The Pennsylvania State University

The Graduate School

Eberly College of Science

PERIODIC GRAVITATIONAL RADIATION FROM NEUTRON STARS WITH EXOTIC MATTER

A Thesis in

Physics

by

Mohit Nayyar

Submitted in Partial Fulfillment
of the Requirements
for the Degree of

Doctor of Philosophy

May 2007

The thesis of Mohit Nayyar was reviewed and approved* by the following:

Benjamin J. Owen
Assistant Professor of Physics
Thesis Adviser
Chair of Committee

Stephane Coutu
Associate Professor of Physics
Associate Professor of Astronomy and Astrophysics

Pablo Laguna
Professor of Physics
Professor of Astronomy and Astrophysics

George G. Pavlov
Senior Scientist, Department of Astronomy and Astrophysics

Jayanth R. Banavar
Professor of Physics
Head of the Department of Physics

*Signatures are on file in the Graduate School.

Abstract

The first generation of interferometric gravitational wave detectors is now in operation and actively searching the skies for gravitational waves. The sources that may be detected include rotating neutron stars, especially if they contain some matter more exotic than neutrons. This thesis investigates issues related to two probable mechanisms for the generation of gravitational radiation from neutron stars containing exotic states of matter. The first is the persistent gravitational radiation from r-mode oscillations in accreting neutron stars containing hyperons, while the second is the gravitational radiation from large elastic deformations in quark-baryon hybrid stars.

Before examining two mechanisms for gravitational radiation generation, we address the neutron star equation of state that forms the basis of any neutron star calculation. To ensure the validity of equations of state used in later sections of the thesis, we constrain a set of relativistic mean field equations of state using the latest neutron star observations. We find that, of these equations of state, only the stiffest previously used in literature satisfy the constraints. We therefore generate new equations of state within the same relativistic mean field framework.

Persistent gravitational radiation caused by r-modes could explain why neutron stars in low mass x-ray binaries (LMXBs) are not being spun up by accretion. A high duty cycle of gravitational radiation is only possible when the cores of these stars contain some exotic state of matter. We examine the scenario for persistent emission for a set of equations of state that allow for the presence of hyperons, and find that persistent emission is robust. Therefore, gravitational radiation from neutron stars in LMXBs is likely to be detectable by advanced gravitational wave detectors if they contain exotic matter.

The spindown for the Crab pulsar suggests that it could be detectable by the first generation of interferometric gravitational wave detectors if much of the spindown is due to gravitational wave emission. Conventional neutron stars cannot support quadrupole moments large enough to generate gravitational radiation commensurate with the Crab pulsar spindown. This warrants the study of other classes of neutron stars containing exotic matter which could display higher quadrupole moments. We, therefore, evaluate the maximum quadrupole moments of a class of baryon-quark hybrid stars. We find that the maximum quadrupole moments are just below the threshold for being detectable by the present generation of detectors, but are good prospects for the next generation.

Table of Contents

List of Figures

List of Tables

Acknowledgments

I thank Ben for being a motivating, friendly and understanding adviser. I am grateful for his enthusiasm for the subject of my research–it would have taken me longer to finish with this PhD if it had been any less contagious. I thank him for all the knowledge and skills I have acquired as a part of learning the scientific process. They are helping me approach the next phase of my life with a sense of confidence and security.

I would like to thank my parents Harish and Rita Nayyar for their invaluable moral support during my years as a graduate student. I thank them for being concerned and interested about my choice of career, and also for the patience they continue to show as I meander my way to my own dream. It is from them that I have learnt to appreciate the values of learning, curiosity and open-mindedness–strong early influences that inexorably led me to graduate school. I am also grateful to my wonderful sister, Shivani Nayyar, for her help in spiritual and emotional matters. I have been able to rely on her whenever my courage, belief and confidence in myself have needed a boost.

I would like to thank all the members of the Institute for Gravitational Physics and Geometry, Center for Gravitational Wave Physics and the Physics department for collaboration, stimulating discussions and friendship. A special thanks to Louis Rubbo for his invaluable help during the process of writing this thesis. I would also like to thank Karen Brewster, Camma Hoffman, Megan Meinecke, Randi Neshteruk and Kathy Smith for their professional help in administrative matters.

Finally, I thank all the wonderful people I had an opportunity to be friends with here in State College. I applaud them for their generosity, warmth and help in keeping my sanity all these years. I reserve a special thanks for Chris Van Den Broeck for helping soothe my doubts related to pursuing a PhD early in my graduate life. An incomplete list of friends I would like to thank: Sanjeevi Atuluguma, Corina Barbu, Shantanu Desai, Yvonne Glanville, Chandrika Gopalakrishna, Russell Hart, Shivprakash Iyer, Joby John, Shivkumar Jolad, Un Jeong Kim, Neeraj Kulkarni, Tim Lezon, Sanghamitra Neogi, Orcan Ogetbil, Sachin Oswal, Mike Peterson, Sanjiv Ramchandran, Priti Shah, Nari Sounderrajan, Birjoo Vaishnav, Kevin Vandersloot, Trevor Wenger and David Whitbeck.

Chapter 1

Introduction

According to Einstein's theory of General Relativity, gravitational waves are ripples in the curvature of spacetime that propagate at the speed of light [1, 2]. Observations have confirmed the prediction of Einstein's theory that matter causes the curvature of spacetime [3]. A standard analogy used to describe gravitational radiation is to relate it to the surface of an orange. Spacetime curvature is like the overall spherical shape of the orange. The skin of the orange is not completely smooth and a magnified view reveals minute variations in height. Gravitational waves are like the fine detail on the skin of the orange. They are curvature perturbations propagating on a large scale background curvature.

The direct detection of gravitational radiation will reveal a new window to the universe and will probe features that cannot be probed by electromagnetic radiation. In contrast with electromagnetic waves, which are incoherent superpositions of emissions from individual atoms and molecules, gravitational waves carry information related to the coherent motions of bulk matter. They are emitted by sources which exhibit time varying multipole moments (quadrupole and higher). They originate in regions of strong gravity, where the bulk motion of matter approaches the speed of light. Since they couple only weakly with matter, they propagate without losing their information content from source to detector. Electromagnetic radiation, however, interacts very strongly with matter. Consequently, the information content of electromagnetic waves emitted from regions of strong gravity is lost due to the scattering and absorption of the radiation by surrounding matter.

The foundations of gravitational radiation theory were laid by Einstein in his 1916 paper [4]. In this first paper he derives results related to the emission of gravitational waves by weak gravity sources, and to their propagation in flat spacetime. Following contributions by Einstein [5], Weyl [6], and Eddington [7] the theory of linearized gravity was completely established by the 1920s. The formalism for the emission of gravitational waves from sources exhibiting strong gravity was given by Landau and Lifshitz in 1941 [8]. The theory for the propagation of short-wavelength gravitational radiation through curved spacetime was presented by Isaacson in a pair of 1968 papers [9, 10].

The detection of gravitational waves requires at least two spatially separated particles. Consider a gravitational wave passing through a plane containing two particles. The wave

will cause the particles to alternately move closer and away from each other. A way of measuring the strength of the gravitational wave is by measuring the observed strain, i.e. the ratio of the displacement of a particle in one of its extreme positions about its mean position to the total separation between the particles. An optimistic strain amplitude caused by a passing gravitational wave is $\sim 10^{-24}$. This low value suggests why gravitational waves have eluded detection. However, their existence has been inferred from orbital period observations of the Hulse Taylor binary pulsar, PSR1913+16, which was discovered in 1974 [11]. The observed rate of orbital decay for this binary system matches the predicted rate from General Relativity due to the emission of gravitational radiation to within a 1% observational error [12].

Motivated by the possibility of directly detecting gravitational radiation from such binary sources, a network of interferometric gravitational wave detectors have been built. At the forefront of this group is the Laser Interferometer Gravitational-Wave Observatory (LIGO) [13] which consists of a set detectors, two of which are located in Hanford, Washington, and one in Livingston, Louisiana. Each detector is a laser interferometer with a 90° opening angle. The strain amplitude is determined by measuring the shift in the interference pattern observed when a gravitational wave passes through the detector. The field of gravitational wave astronomy is becoming exciting as these first generation ground based interferometric gravitational wave detectors have started reaching their target sensitivities [14]. The prospect of detecting gravitational radiation by such detectors is particularly high [15].

Gravitational radiation from rotating neutron stars has frequencies similar to their spin frequencies. Since the spin frequencies lie within the target frequency range of the ground based detectors, 10–100 Hz, neutron stars are bright prospects for detection. Neutron stars are a class of highly compact objects which exhibit extreme properties that are not observed elsewhere in the universe. They are created in the aftermath of supernova explosions with typical masses around $1.4M_{\odot}$, but radii of only $\sim$ 10 km. The high concentration of mass implies that, with the exception of black holes, these objects exhibit the strongest gravitational effects in the present universe. The acceleration due to gravity at the surface of a neutron star is about 10^{11} times greater than its value at the surface of the Earth. The spin periods of neutron stars are short and stable: the fastest observed neutron star has a spin frequency of 716 Hz [16], although a claim of 1122 Hz has been made by Kaaret et al [17]. Neutron stars are also believed to have the highest magnetic fields in nature. The highest are expected to be found in 'magnetars[1]' which could have fields as high as 10^{15} G [18].

Neutron stars were first conceptualized as 'giant nuclei' by Landau [19] in 1932. The

[1] Although gravitational waves from these stars are not expected to be detectable by LIGO as they have large spin periods.

connection between neutron stars and supernovae was first proposed by Baade and Zwicky in their 1934 paper [20]. Five years later, Oppenheimer and Volkoff described a method for calculating the structure of non-rotating neutron stars [21]. The first neutron star was not discovered until 1967. Hewish and Bell [22] discovered a pulsating radio source whose identification as a neutron star was made shortly thereafter by Gold [23].

Neutron stars are most commonly discovered as pulsars (like Hewish and Bell's discovery). During certain phases of their life cycle neutron stars exist as pulsars, i.e. sources of periodic electromagnetic emission. The continuous emission from a neutron star, which is powered by rotation and emitted in a narrow beam from its magnetic poles is observed only periodically on Earth. The periodicity is a result of a misalignment between the beamed emission and Earth's line of sight to the star: the emission is observed only when the beam sweeps over the Earth. Pulsars appear both as isolated stars or with a companion in binary configurations. They emit electromagnetic radiation from radio (10^7 Hz) to gamma frequencies (10^{22} Hz).

A class of gravitational wave sources associated with neutron stars are magnetic mountains [2]. Mountains impart time varying quadrupole moments to rotating neutron stars, and thereby cause gravitational wave emission. Magnetic mountains form on neutron stars with toroidal magnetic fields [24, 25]. A neutron star might develop such a toroidal field through differential rotation as it forms after a supernova event. If it develops the toroidal field due to differential rotation, then in the initial configuration the magnetic axis will be aligned with the rotation axis. In this configuration, the star is unstable as the magnetic field tries to make it prolate in opposition to rotation which tries to make it oblate. As a result, the magnetic field axis is likely to migrate until it is perpendicular to the rotation axis, as that is the minimum energy configuration of the system.

Another way mountains can form on neutron stars is by the mechanism of magnetic funneling [26]. Mountains could form on neutron stars which exhibit large magnetic fields and gravitationally attract matter from their surroundings. The magnetic field funnels the infalling material to the magnetic poles of the star and keeps it bottled there. Formation of these mountains follows from the conducting properties of the accreting material which allows it to go along magnetic lines faster than it crosses them.

The quadrupole moment of a neutron star can sometimes be more conveniently expressed in terms of its ellipticity, ϵ, which is a dimensionless quantity, comparable to the quadrupole moment over the moment of inertia of the star. The spindown limit of the Crab pulsar, which is calculated assuming that the spindown of the pulsar is caused exclusively by the emission of gravitational radiation, is $\epsilon \sim 7 \times 10^{-4}$ [15, 27]. Normal neutron stars, which are stars that contain only neutrons, protons, electrons, and muons, are expected to have

[2] Mountains is a misnomer in the context of neutron stars. The mountains on neutron stars could be only up to ~ 1 cm high, and up to ~ 1 m on quark stars

much lower maximum ellipticities of a few times 10^{-7} [28, 29]. However, there are a few categories of stars composed of exotic states of matter which might have larger values of maximum ϵ [27]. Of these, the highest prediction is by Xu [30] for solid strange stars which could have ellipticities as high as 6×10^{-4} as estimated by Owen [31].

Hybrid stars are another class of exotic matter stars that could exhibit high ellipticities [32]. Hybrid stars are stars which possess both normal neutron star matter and some other exotic state of matter (quarks [33] or meson-condensates [34]). The large elastic deformations in these stars are due to the formation of a crystalline lattice between the normal and exotic phases of matter in the regions where they coexist. Owen [31] made rough estimates of the maximum ellipticities for hybrid stars obtaining a value of 10^{-5}. With the expectation of revising Owen's estimates upwards, closer to initial LIGO's sensitivity threshold, we made a more detailed calculation of, specifically, baryon-quark hybrid stars. We found ellipticities as high as 3×10^{-5} which is within a factor of a few of initial LIGO's threshold for some known pulsars [27].

One of the periodic sources this thesis focuses on are neutron stars in low mass x-ray binaries (LMXBs). These binary systems are characterized by a disk of infalling matter surrounding the neutron star formed by the tidal destruction of the low mass companion star. The infalling matter gradually spirals into the neutron star heating up and radiating in x-rays. Since it carries the companion's angular momentum it should also result in imparting high spin frequencies to the neutron star. It has, however, been observed that the neutron stars in these systems are not rotating as fast as they should be. In fact, the observed rotation is mostly in a relatively narrow band of frequencies, $\sim$ 300–600 Hz [35]. This suggests that there is some mechanism responsible for taking away the angular momentum gained by the neutron star.

A possible mechanism could be the persistent gravitational radiation caused by r-mode oscillations [28, 36]. The emission of gravitational radiation usually causes modes to damp out. R-mode oscillations, however, are a type of normal mode of oscillations of a star which are driven unstable by gravitational radiation. This unexpected behavior is a result of the Chandrasekhar-Friedman-Schutz Instability (CFS) which occurs when a prograde mode in the co-rotating frame of the star appears retrograde in an inertial frame of reference [37, 38]. The angular momentum of the mode is negative, and the loss of angular momentum and rotational energy caused by the emission of gravitational radiation, causes the angular momentum of the mode to become more negative. This implies the growth of the mode, which causes more gravitational radiation, which causes further growth of the mode. This feedback cycle constitutes the CFS instability.

The mechanism for persistent wave emission relies on a specific behavior of viscosity: namely, the viscosity is an increasing function of temperature near 10^8 K [39]. The viscous process that satisfies this requirement is the bulk viscosity caused by the presence of exotic

matter in the core of the neutron star. Bulk viscosity is caused by irreversible processes which convert the mechanical energy of r-modes to heat. The presence of exotic matter is a reasonable expectation as the densities in the cores of neutron stars can easily exceed the nuclear density ($\epsilon_0 = 2.8 \times 10^{14}$ g/cm^3) by a factor of more than 2–3. In the thesis we explore this mechanism for stars whose exotic content is hyperons. In Chapters 4 and 5, we explore the entire range of a class of equations of state to see how robust this mechanism is to estimate how realistically we can expect LIGO to detect such a source.

Any neutron star calculation requires a reliable high-density equation of state, which is the pressure of neutron star matter as a function of its density. There are broadly two types of neutron star equations of state in common use. The first kind are the 'potential-based' equations of state that rely on the detailed modeling of the nuclear potential [40, 41, 42]. The other are the relativistic mean field equations of state [32]. Most of the work in this thesis uses the latter category. These equations of state model the strong nuclear force as a tree-level exchange of mesons. The free parameters are constrained using the latest neutron star observations [43, 44, 45].

In this thesis Chapters 3 and 5 reproduce two papers that have been published in the journal Physical Review D. The material in Chapter 6 is not published yet but will be submitted to a journal at a later time. As some of the chapters in this thesis are exact reproductions of published papers, at times the reader can expect to be referred ahead to material that appears later in the thesis. Chapter 2 presents background material for both Chapters 3, 5, and 6. Chapter 4 presents background material for Chapter 5. All three papers are collaborative efforts with Dr. Benjamin Owen. Chapter 2 was also done in collaboration with Benjamin Lackey, who was at the time an undergraduate student at the Pennsylvania State University. I am the chief contributor to the research presented in all three papers. In many cases the preliminary results were derived from a code written by me and have been confirmed by Dr. Owen who wrote his own parallel code. In Chapter 5 the only aspect I was not involved with was the generation of the Mass-Radius and Mass-Redshift plots which were made by Benjamin Lackey. The responsibility of writing the three papers was shared between Dr. Owen and myself. For the most part, I did the bulk of the writing while Dr. Owen played an editorial role to ensure that the quality of writing was worthy of publication in a reputable journal.

The thesis outline is as follows. Chapters 2 and 3 detail research pertaining to constraining a set of mean field equations of state using the latest astronomical observations. Chapter 2 serves as an introduction to Chapter 3 which is a reproduction of the published paper entitled *Observational constraints on hyperons in neutron stars* [46]. In Chapter 2 we supply details related to the relativistic mean field equation of state not provided in either Chapter 3 or 5.

Chapters 4 and 5 concern the study of the viability of persistent gravitational radiation

caused by r-modes in neutron stars. Chapter 4 serves as an introduction to the reproduction of the published paper *R-modes of accreting hyperon stars as persistent sources of gravitational radiation* [47] presented in Chapter 5. In Chapter 4 we review r-mode oscillations explaining their relevance to gravitational radiation from neutron stars. We explain the Chandrasekhar-Friedman-Schutz instability and the mechanism of hyperon bulk viscosity. We present the important derivation of the coefficient of bulk viscosity appropriate to multi-component relativistic fluids. We also reproduce the derivation of the expression for the relaxation timescale appropriate to non-leptonic weak interactions taking place in a dense Fermi liquid. We also show the calculation of the collision integrals for the non-leptonic weak interactions of interest to us.

In Chapter 6 we calculate the quadrupole moments for a class of baryon-quark hybrid stars and comment on the likelihood of detection of gravitational radiation from them by LIGO. Since this work is not yet published, the chapter contains substantial background material which will be edited before submission to a journal.

Chapter 2

Neutron star equation of state

This chapter in conjunction with the descriptions in Sec. 3.2 and Sec. 5.2.1 provides a brief summary of the neutron star equation of state. It serves as an introduction to Chapters 3 and 5, which have been published as technical articles [46, 47].

2.1 Overview

The equation of state of high-density neutron star matter is highly uncertain [32]. It is predicted by extrapolating from experiments on ordinary atomic nuclei corresponding to the energy density $\epsilon = 2.8 \times 10^{14}$ g/cm^3 to densities in the cores of neutron stars which can exceed 2–3 times this value. More specifically, it relies on the careful distillation of certain numbers, from experiments on thousands of nuclei, into a handful of numbers characterizing bulk matter. Even the composition of neutron star matter is uncertain. While the composition of the nuclear-density mantle of the neutron star is relatively well known, there exist numerous exotic matter possibilities for the core. The high density of the core could cause the transformation of nucleons to hyperons or meson condensates. Beyond densities where the distance between the baryons becomes smaller than the diameter of a baryon (2–3 times nuclear density), it is reasonable to expect that individual baryons lose their identity and baryonic matter is transformed to quark matter. What exotic states of matter exist in the cores is an open question.

New observations are challenging our belief in the established maximal properties of neutron stars [43, 44, 45]. The latest observations are given in the introduction to Chapter 3. Here we give a brief summary of mass and radius observations prior to when this thesis was begun (2002). Most mass measurements are obtained from radio observations of pulsars in binary configurations. Thorsett and Chakrabarty [48] established that the masses of neutron stars in these systems are all clustered in a very small range whose upper limit is $1.45 M_\odot$[1], see Fig. 2.1. The masses of neutron stars in accreting systems are expected to be higher but are harder to measure. A commonly cited example is that of Vela X-1 whose mass has been measured to be $1.85 M_\odot \pm^{0.35}_{0.30}$ at the 95% confidence level [49]. However, there are systematic errors in this measurement which render a statement of statistical confidence

[1] $M_\odot$ represents the mass of the Sun which is 1.99×10^{30} kg.

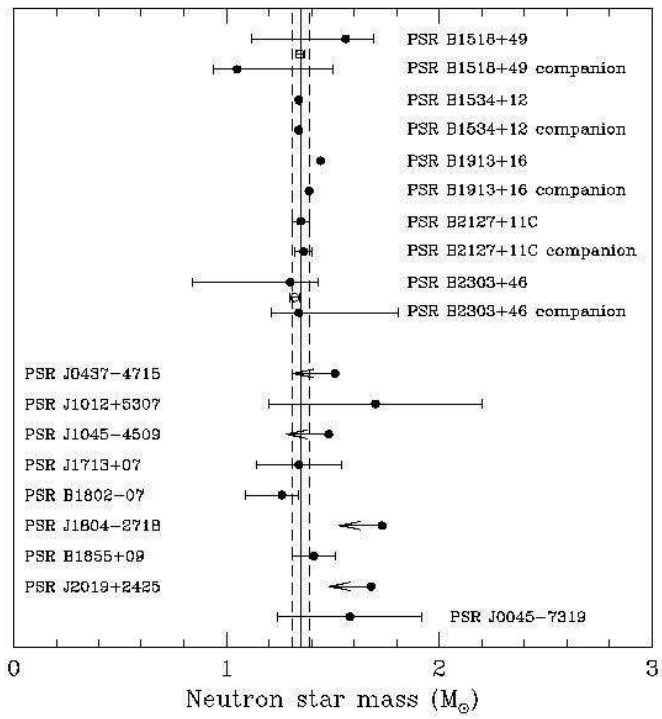

Figure 2.1: Known masses of radio pulsars, with error bars, from the 1998 paper by Thorsett and Chakrabarty [48].

suspect [35]. Precise measurement of the radius of neutron stars is much more difficult [50]. Most measurements are based on observations of thermal emissions from the surface of neutron stars which measure the 'radiation' radius, R_∞, of the star which is related to the coordinate radius, R, of the star by

$$R_\infty = \frac{R}{\sqrt{1-(2GM)/(Rc^2)}}. \tag{2.1}$$

The 'radiation' radius is greater than R due to the deflection of light in a strong gravitational field. Even around 2002, there were a wide range of measured radius values [50]. A lot of these were very small values, which suggests that the emission is caused by localized heating at the poles and is not from the entire star surface. The radius measurement involves either making the assumption that the star is a perfect black body or modeling the atmosphere. The measured radius is therefore dependent on which assumption is made. There were no precise gravitational redshift measurements before the recent $z = 0.35$ observation by Cottam, Paerels, and Mendez [45]. Subsequently, a smaller gravitational redshift measurement of $z = 0.28$ has been made [51], though the result is uncertain as more than one transition could account for each of the observed spectrum lines the result is based on.

Neutron star equations of state can be broadly put in two different categories: equations of state based on relativistic mean field theory and equations of state based on the detailed modeling of the nuclear potential [50]. In this thesis we usually use equations of state belonging to the former category. A brief summary is given in the next section which complements the descriptions in Sec. 3.2 and Sec. 5.2.1. The latter category can be further subdivided into relativistic or non-relativistic potential-based equations of state. One of the most widely used non-relativistic potential-based equations of state is the APR equation of state [40]. The relativistic potential based equations are referred to as Brückner-Hartree-Fock equations of state [52] and their behavior is similar to relativistic mean field models. A brief comparison of the two approaches is given in Chapter 3.

2.2 Relativistic mean field theory

A brief summary of the relativistic equation of state is given in papers I (Sec. 3.2) and II (Sec. 5.2.1). In this section we state the details that are not explained in the papers. I suggest the reader read Sec. 5.2.1 before reading the remainder of this chapter.

We use baryonic equations of state based on the framework of relativistic mean field theory developed by Glendenning [53] from earlier works by others. The basic neutron star contains neutrons, protons, electrons, and muons. We assume for the purposes of paper I that at higher densities the neutron star is also populated by hyperons. Relativistic mean field theory models the strong interaction as a tree-level exchange of mesons between the

baryons. The σ scalar meson simulates the attractive part of the strong interaction while the ω vector meson models its repulsive part. We know from experiments that nuclei with equal numbers of neutrons and protons (isospin symmetry) have lower energies than similar nuclei with dissimilar number of neutrons and protons. This type of behavior is mimicked in neutron star matter by the ρ isovector meson. The Lagrangian in Glendenning's theory consists of free particle terms for the baryons and the mesons, interaction terms between the baryons and mesons, and two σ self-interaction terms which expand effectively in weak σ:

$$\begin{aligned}
\mathcal{L} &= \sum_B \overline{\Psi}_B (i\gamma_\mu \partial^\mu - m_B + g_{\sigma B}\sigma - g_{\omega B}\gamma_\mu \omega^\mu - \frac{1}{2} g_{\rho B}\gamma_\mu \boldsymbol{\tau}\cdot\boldsymbol{\rho}^\mu)\Psi_B \\
&\quad + \sum_\lambda \overline{\Psi}_\lambda (i\gamma_\mu \partial^\mu - m_\lambda)\Psi_\lambda \\
&\quad + \frac{1}{2}(\partial_\mu \sigma \partial^\mu \sigma - m_\sigma^2 \sigma^2) - \frac{1}{3} b m_n (g_\sigma \sigma)^3 - \frac{1}{4} c (g_\sigma \sigma)^4 \\
&\quad - \frac{1}{4}\boldsymbol{\rho}_{\mu\nu}\cdot\boldsymbol{\rho}^{\mu\nu} + \frac{1}{2} m_\rho^2 \boldsymbol{\rho}_\mu \boldsymbol{\rho}^\mu - \frac{1}{4}\omega_{\mu\nu}\omega^{\mu\nu} + \frac{1}{2} m_\omega^2 \omega_\mu \omega^\mu .
\end{aligned} \tag{2.2}$$

Here Ψ_B and Ψ_λ are the spinors for the baryons and leptons, respectively. The parameters $g_{\sigma B}$, $g_{\omega B}$, and $g_{\rho B}$ are the coupling constants between the baryons and the σ, ω, and ρ mesons, respectively. The parameter $m_{subscript}$ is the mass of the respective particle. The parameters b and c are the coupling constants for the scalar self-interaction terms. The vector $\boldsymbol{\tau}$ is the isospin vector. The first line in the above equation contains the free particle baryonic terms and the meson interaction terms. The second line contains the free leptonic terms. The third line contains the free-particle σ terms and also the corresponding perturbative self-interaction terms. The fourth line contains the free-particle terms for the vector and isovector mesons.

The Euler-Lagrange equations for the baryons and the mesons are determined from the Lagrangian. The meson equations are simplified by the *relativistic mean field approximation* which entails replacing the mesonic fields by their mean values under the assumption that the ground state of nuclear matter is static and spatially uniform. The assumption that the ground state is uniform also implies that the space-like components of the ω meson and the ρ isovector meson are identically zero. Since, neutron star matter is in its ground state, of these only the ρ_3^0 component of the ρ meson survives, i.e. is non-zero. The remaining procedure of obtaining the equation of state is given in chapter 5 (Sec. 5.2.1).

The coupling constants of the theory are obtained from five numbers extracted from nuclear experimental data. These numbers quantize specific properties of bulk nuclear matter. A neutron star can be thought of as one very large nucleus. This analogy suggests that we can use information from finite nuclear data to help determine the equation of state of a neutron star, although the properties of bulk matter can be obscured by finite size

effects. Some of these numbers are related to the property of saturation. Saturation refers to the property of the central density of the nucleus of being independent of the number of nucleons in it for large atomic mass number Z. The five numbers are: the number density at saturation n_0, the energy density at saturation ϵ_0, the coefficient of isospin asymmetric energy, a_{sym}, the effective nucleonic mass, m^*, and the nuclear compressibility, K. The number density and energy density are precisely known. The remaining three numbers are not as well known.

The number density at saturation can be determined from the radius of the nucleons. Saturation implies that the radius of each nucleon, r_0, has the same value, $r_0 = 1.16$ fm which is determined from electron-nucleus scattering experiments. The number density is then given by

$$n_0 = \left[(4\pi/3){r_0}^3\right]^{-1}. \tag{2.3}$$

We use a value of $n_0 = 0.153$ fm^{-3}.

Saturation also implies a constant value of the energy density. The energy density is determined from the semiempirical mass formula which is based on the liquid drop model. This formula expresses the mass of the nucleus as a function of A and Z (atomic number) and, in addition to the volume contribution, also includes contributions from the surface energy, Coulomb interaction, and isospin asymmetry energy:

$$M(A,Z) = A\left[\frac{4}{3}\pi {r_o}^3\epsilon_0 + a_{sym}\left(\frac{N-Z}{A}\right)^2\right] + 4\pi {r_0}^2 A^{2/3}\epsilon_{surf} + \frac{3}{5}\frac{e^2Z^2}{r_0A^{1/3}}. \tag{2.4}$$

Here a_{sym} is the coefficient of isospin asymmetry, ϵ_{surf} appears in the surface term and the last term is the Coulombic contribution. To obtain the energy density from this formula we first determine the value of the binding energy per nucleon, B/A. We obtain B/A by subtracting the bare mass contributions of the nucleons from the mass formula and dividing the result by A. However, obtaining more precise values of B/A requires a more detailed version of the semiempirical mass formula, which includes terms from several additional effects. The coefficients of the additional terms are obtained using best fit methods on data from experiments on several different nuclei. Using the more complicated formula results in a series in $1/A$. A precise value of B/A is obtained by taking the limit of the series as A goes to infinity and $Z = A/2$. The energy density can now be obtained using

$$\frac{B}{A} = \left[\frac{\epsilon}{n}\right]_0 - m_N, \tag{2.5}$$

and Eq. (2.3). The mass m_N is the average mass of the neutron and proton, and the subscript "0" from this point on refers to quantities at saturation. We use the value 141 MeV/fm^3 for the energy density at saturation in all our calculations.

The coefficient a_{sym} is also obtained from the semi-empirical mass formula. It is, however, believed that the contribution from isospin asymmetry energy to the mass formula does not stay quadratic away from isospin symmetry. In neutron stars where neutrons heavily outnumber protons, we expect a non-negligible contribution from other non-quadratic isospin energy terms. Following standard practice we keep only the quadratic term and use the value 32.5 MeV for the coefficient a_{symm} in this thesis.

The compression modulus, K, is a measure of how fast the energy density changes when the density of neutron star matter is changed. It is defined at saturation as

$$K = \left[k^2 \frac{d^2}{dk^2} \frac{\epsilon}{n} \right]_0 . \tag{2.6}$$

Here, k is the Fermi momentum, and the 0 subscript denotes saturation. It is obtained from experiments that involve perturbing the nucleus and obtaining the resulting 'giant monopole resonance'. It characterizes the radial or 'breathing' mode of vibrations of the nucleus. There is a great deal of uncertainty about the value of K. This is because these experiments do not directly measure K. Instead, K is determined using modeling techniques, which can be, broadly speaking, categorized as either relativistic or non-relativistic techniques. The range of values of K obtained from relativistic models is higher than non-relativistic models. Following Glendenning [32], we consider the range 240–300 MeV for the relativistic equations of state we use. For some non-relativistic equations of state used in Chapter 3 we allow the compressibility to go as low as 120 MeV for a "straw man" equation of state sometimes used in literature

The effective mass m^* of a nucleon in a dense medium is lower than its bare mass value. The Euler Lagrange equations in Glendenning's framework allow the identification $m^* = m - g_\sigma \sigma$. These equations also contain terms which involve summing $[k_f^2 + m^{*2}(k_f)]^{1/2}$ over the momentum states below the Fermi momentum k_f. Since k_f depends on the density this indicates the importance of m^* to extrapolation to the high density regime. Following Glendenning [32], we use the range of values 0.70–0.78 m_N for m^*.

Four of the coupling constants, $(g_\sigma/m_\sigma)^2$, $(g_\omega/m_\omega)^2$, b, and c, are determined from a less complicated model of mean field theory which does not contain the ρ meson and treats the neutrons and protons as identical particles. They are determined using the experimentally determined values of the saturation number density, n_0, the binding energy at saturation, B/A, the compression modulus, K, and the effective mass, m^*. The energy density, and

the σ and ω Euler-Lagrange equations for this model are written, respectively, as

$$\begin{aligned}
\epsilon &= \frac{1}{3}bm_N\left(g_\sigma\sigma\right)^3+\frac{1}{4}c\left(g_\sigma\sigma\right)^4+\frac{1}{2}m_\sigma^2\sigma^2+\frac{1}{2}m_\omega^2\omega_0^2 \\
&\quad +\frac{2}{\pi^2}\int_0^{k_N}\sqrt{k^2+m_N^{*2}}k^2dk, \qquad (2.7)\\
m_\sigma^2\sigma &= g_\sigma\left[\frac{2}{\pi^2}\int_0^{k_N}k^2dk\frac{m_N-g_\sigma\sigma}{\sqrt{k^2+(m_N-g_\sigma\sigma)^2}}\right] \\
&\quad -bm_Ng_\sigma(g_\sigma\sigma)^2-cg_\sigma(g_\sigma\sigma)^3, \qquad (2.8)\\
g_\omega\omega_0 &= \left[\frac{g_\omega}{m_\omega}\right]^2 n_N, \qquad (2.9)
\end{aligned}$$

where k_N is the Fermi momentum of nucleons and m_N^* is the effective mass, $m_N^*=m_N-g_\sigma\sigma$.

We now take the derivative of Eq. (2.7) with respect to the nucleonic number density to obtain

$$\begin{aligned}
\frac{d\epsilon}{dn_N} &= \frac{d\sigma}{dn_N}\left[m_\sigma^2\sigma+\frac{dU}{d\sigma}\right. \\
&\quad \left.-g_\sigma\frac{2}{\pi^2}\int_0^{k_N}k^2dk\frac{m_N-g_\sigma\sigma}{\sqrt{k^2+(m_N-g_\sigma\sigma)^2}}\right] \\
&\quad +g_\omega\omega_0+\sqrt{k_N^2+(m_N-g_\sigma\sigma)^2}. \qquad (2.10)
\end{aligned}$$

The quantity in the square parenthesis is zero by Eq. (2.8), while U is the σ perturbative terms

$$U=\frac{1}{3}bm_N(g_\sigma\sigma)^3+\frac{1}{4}c(g_\sigma\sigma)^4. \qquad (2.11)$$

We thereby obtain the result that $d\epsilon/dn_N$ is equal to the chemical potential of the nucleons at the Fermi surface, i.e.

$$\begin{aligned}
\frac{d\epsilon}{dn_N} &= g_\omega\omega_0+\sqrt{k_N^2+m_N^*} \qquad (2.12)\\
&\equiv \mu_F. \qquad (2.13)
\end{aligned}$$

The function ϵ/n_N has its minimum value at saturation which implies that

$$\left[\frac{d}{dn_N}\frac{\epsilon}{n_N}\right]_0=\left[\frac{1}{n_N}\left(\frac{d\epsilon}{dn_N}-\frac{\epsilon}{n_N}\right)\right]_0=0, \qquad (2.14)$$

which results in, using Eq. (2.12),

$$\left[\frac{\epsilon}{n_N}\right]_0=\mu_F. \qquad (2.15)$$

If we use Eq. (2.12), (2.9), and (2.5) in the above equation we obtain

$$m_N + \frac{B}{A} = \left[\left[\frac{g_\omega}{m_\omega} \right]^2 n_N + \sqrt{k_N^2 + m_N^*} \right]_0 . \tag{2.16}$$

This equation can be solved to determine $(g_\omega/m_\omega)^2$.

To determine $(g_\sigma/m_\sigma)^2$, b, and c we rewrite the expression for the compressibility Eq. (2.6) using $n_N = k_N^3/(3\pi^2)$:

$$K = 9 \left[n_N^2 \frac{d^2}{dn_N^2} \frac{\epsilon}{n_N} \right]_0 . \tag{2.17}$$

At saturation the double derivative $(d^2\epsilon/dn_N^2)$ can be written as $(1/n_N)d\mu_F/dn_N$ which when substituted in the expression for K gives

$$K = 9 \left[\frac{d\mu_F}{dn_N} \right]_0 . \tag{2.18}$$

From the definition $\mu \equiv g_\omega \omega_0 + \sqrt{k^2 + {m_N^*}^2}$ we obtain

$$\frac{d\mu}{dn_N} = \left(\frac{g_\omega}{m_\omega} \right)^2 + \frac{1}{\sqrt{k^2 + m_N^*}} \left(k \frac{dk}{dn_N} - m_N^* g_\sigma \frac{d\sigma}{dn_N} \right) . \tag{2.19}$$

The derivative $d\sigma/dn_N$ is obtained by taking the derivative of the σ Euler-Lagrange equation Eq. (2.8). Once the derivative $d\sigma/dn_N$ is known it can be substituted into Eq. (2.19) which in turn can be substituted into Eq. (2.18). The equation we thereby obtain is

$$\begin{aligned} K \;=\; & \left[\left[\frac{g_\omega}{m_\omega} \right]^2 \frac{6k_N^3}{\pi^2} + \frac{3k_N^2}{E(k_N)} \right. \\ & \left. - \frac{6k_N^3}{\pi^2} \left(\frac{m_N^*}{E(k_N)} \right)^2 \left(\frac{g_\sigma}{m_\sigma} \right)^2 \left\{ 1 + \left(\frac{g_\sigma}{m_\sigma} \right)^2 \left(\frac{d^2U}{d(g_\sigma\sigma)^2} + \frac{2}{\pi^2} \int_0^{k_N} \frac{k^4 dk}{E^3(k)} \right) \right\} \right]_0 \end{aligned} \tag{2.20}$$

where

$$E(k_N) = \sqrt{k_N^2 + {m_N^*}^2}. \tag{2.21}$$

The value of $g_\sigma\sigma = m - m^*$ is known at saturation since the value of m^* is known. The above equations are therefore a system of linear equations in the vector of three unknowns $(g_\sigma/m_\sigma)^2$, b, and c. The system is solved by standard matrix-inversion. The other two equations required to determine the value of these variables are the equation for the energy density, Eq. (2.7), and the σ Euler-Lagrange equation, Eq. (2.8), both of which are also linear in these variables, and can be solved individually.

The coupling constant $(g_\rho/m_\rho)^2$ is determined by first determining an expression for a_{sym}. For this we need the complete mean field theory which includes the ρ meson and does not treat the neutron and proton as identical particles. It is easy to see from the semiempirical mass formula, Eq. (2.4), that a_{sym} can be written as

$$a_{sym} = \frac{1}{2}\left[\frac{\partial^2(\epsilon/n_N)}{\partial t^2}\right]_{t=0}, \tag{2.22}$$

where, $t = (n_n - n_p)/n_N$, $n_N = n_n + n_p$, and n_n and n_p are the number densities of the neutrons and protons, respectively. We now determine that part of the energy, per unit nucleon, that depends on the asymmetry between the neutrons and protons from Eq. (5.10):

$$\begin{aligned}\frac{\epsilon_s}{n_N} &= \frac{1}{8}\left(\frac{g_\rho}{m_\rho}\right)^2 n_N t^2 + \frac{1}{n_N}\frac{1}{\pi^2}\left[\int_0^{k_p} k^2 dk\sqrt{k^2+(m_p - g_\sigma\sigma)^2}\right. \\ &+ \left.\int_0^{k_n} k^2 dk\sqrt{k^2+(m_n - g_\sigma\sigma)^2}\right]\end{aligned} \tag{2.23}$$

Here, ϵ_s is the asymmetry energy per unit volume. Now, on evaluating Eq. (2.22) using Eq. (2.23), and rearranging the result, we obtain

$$\left[\frac{g_\rho}{m_\rho}\right]^2 = \frac{8}{n_N}\left[a_{sym} - \frac{k_N^2}{6E(k_N)}\right]_0. \tag{2.24}$$

Since, all quantities on the right hand side of Eq. (2.24) are known we can now calculate $(g_\rho/m_\rho)^2$ also.

Hyperon couplings to the mesons are expected to be different from the couplings of baryons due to the presence of the isospin-neutral strange quark in hyperons. The hyperon coupling constants are determined from Λ-hypernuclei data [54]. A relativistic mean field model for finite hypernuclei is fitted to the energy levels of various Λ hypernuclei to obtain the constraint that $x_\sigma = 0.46 \pm 0.26$ and $x_\omega = 0.48 \pm 0.32$. Another constraint on the coupling constants is obtained from the binding energy of Λ hyperons in saturated nuclear matter. This has been determined to be -28 MeV. The expression that relates the binding energy to the coupling constants is given by

$$(B/A)_\Lambda = (x_\omega V - x_\sigma S)_0, \tag{2.25}$$

where $S = g_\sigma\sigma$ is the value of the scalar field and $V = g_\omega\omega$ is the value of the vector field at saturation. At saturation $V = (g_\omega/m_\omega)^2(n_N)_0$ from Eq. (2.9), while $S = m_N - m^*{}_0$. The ratio x_ρ is unconstrained from Λ-hypernuclei experiments as the Λ has no isospin. It is usual practice to set $x_\rho = x_\omega$. Most results are not sensitive to this somewhat arbitrary choice.

This completes the introduction to relativistic mean field equations of state. We are now ready to address the address the issue of constraining the equation of state using the latest neutron star observations.

Chapter 3

Observational constraints on hyperons in neutron stars

The possibility that neutron stars may contain substantial hyperon populations has important implications for neutron-star cooling and, through bulk viscosity, the viability of the r-modes of accreting neutron stars as sources of persistent gravitational waves. In conjunction with laboratory measurements of hypernuclei, astronomical observations were used by Glendenning and Moszkowski [Phys. Rev. Lett. **67**, 2414 (1991)] to constrain the properties of hyperonic equations of state within the framework of relativistic mean-field theory. We revisit the problem, incorporating recent measurements of high neutron-star masses and a gravitational redshift. We find that only the stiffest of the relativistic hyperonic equations of state commonly used in the literature is compatible with the redshift. However, it is possible to construct stiffer equations of state within the same framework which produce the observed redshift while satisfying the experimental constraints on hypernuclei, and we do this. The stiffness parameter that most affects the redshift is not the incompressibility but rather the hyperon coupling. Nonrelativistic potential-based equations of state with hyperons are not constrained by the redshift, primarily due to a smaller stellar radius.

3.1 Introduction

The observed masses of neutron stars have been used for years to constrain theoretical predictions of the equation of state of degenerate matter at high density [32]. If an equation of state is "soft" (low pressure) at high density, the maximum mass of a stable star in general relativity is lower than for a "stiff" (high pressure) equation of state. The most massive observed neutron star then sets a limit on the softness of the equation of state. An accumulation of neutron star-cooling observations favors (though not decisively) the presence of exotic particles such as hyperons in the cores of some neutron stars [55], which tends to soften the equation of state. Hyperonic couplings in a relativistic mean-field theory of dense matter can be constrained to a range of values based on the measured properties of Λ hypernuclei and the maximum neutron-star mass [54]. This information is in turn useful for predictions of the bulk viscosity of hyperonic matter [56, 57], which has important

implications for the viability of r-modes in accreting neutron stars as persistent sources of gravitational radiation [58]. Spurred by these implications and by new observations, we revisit the constraints on hyperonic equations of state.

First we consider the maximum mass. The most precise observations of neutron-star masses come from radio pulsars in binaries, which are all measured with 95% confidence to be less than 1.5 $M_\odot$ [48]. Accreting neutron stars are naturally expected to be more massive, and x-ray measurements have long suggested that this is so. The best case for decades has been Vela X-1 (4U 0900-40), with a most likely mass of about 1.8 $M_\odot$ but with 1.5 $M_\odot$ included in the 95% confidence interval [49]. However, this measurement is now known to be contaminated by oscillations of the high-mass main sequence companion [35]; and while more recent measurements [59, 60] can claim smaller statistical confidence intervals, they are still subject to large and poorly quantified systematic errors. Thus 1.5 $M_\odot$ has remained the constraint for many years.

However, this is changing. Recent radio observations of PSR J0751+1807 by Nice *et al.* [44, 61, 62] yield a neutron-star mass greater than 1.6 $M_\odot$ at the 95% confidence level. PSR J0751+1807 orbits a white dwarf which, unlike the main sequence star in Vela X-1, shows no evidence of oscillations. The orbital period is 6 hours, short enough that its decay due to gravitational radiation is observable. This provides a post-Keplerian parameter to disambiguate the two masses. Marginal detection of the Shapiro delay implies intermediate orbital inclination angles, and disambiguates the inclination angle (somewhat) from the mass of the neutron stars (see the figure in Ref. [62]). Also, Ransom *et al.* [43] find through measurements of the periastron advance of the highly eccentric orbit that Ter 5 I has 1.68 $M_\odot$ or higher, formally at the 95% confidence level. Overall this bound is tighter than that for PSR J0751+1807, but the companion is probably a white dwarf and there may be some contamination of the relativistic periastron advance by its rotationally induced quadrupole. Thus the mass constraint on equations of state is now at least 1.6 $M_\odot$ and may be 1.7 $M_\odot$.

Another constraint is the measurement of a gravitational redshift by Cottam, Paerels, and Mendez [45]. The low-mass x-ray binary EXO0748-676 displayed several absorption lines (inferred from multiple x-ray burst spectra) consistent with a redshift $z = 0.35$. Estimates of numerous possible sources of error in the redshift amount to a total of no more than 5% [63], implying that equations of state should be ruled out if their maximum redshift is below about 0.33.

Qualitatively, it has been stated [45] that softer equations of state are disfavored by the redshift; here we make that quantitative. Like Glendenning and Moszkowski [54], we constrain the parameters of relativistic mean field theory between astronomical observation and hypernuclear experiment. Since there is a fairly large parameter space involved, most papers using the results of relativistic mean-field theory use two canonical parameter sets

corresponding to a soft equation of state and a stiff equation of state. We find that the so-called stiff equation of state is actually the softest allowed (marginally) by the redshift observation if hyperons are present. However, we can and do construct stiffer equations of state that are compatible with hypernuclear measurements and consistent with the redshift observation. The most important stiffness parameter as far as the redshift is concerned is the hyperon coupling (and thus hyperon population) rather than the incompressibility. We also note that nonrelativistic potential-based equations of state are not greatly constrained by the redshift observation (they can all reproduce it due to their smaller stellar radii). The new neutron-star masses do not constrain the relativistic mean-field equations of state much compared to the redshift, but potential-based models are constrained more effectively by the masses than by the redshift. In the Appendix we provide tabulations of several relativistic mean-field theory equations of state with hyperons that satisfy the new observational constraints for a variety of nuclear-matter parameters.

3.2 Equations of state

We consider two types of high-density equation of state in this chapter. The first is the main focus of the chapter, and the second is used for comparison to demonstrate model dependence.

The first is based on relativistic mean-field theory and is discussed in detail in Ref. [32]. (We note that other relativistic models, such as the relativistic Brückner-Hartree-Fock of Ref. [52], produce equations of state with qualitatively similar behavior.) Here the low-energy strong nuclear interaction is modeled as the tree-level exchange of mesons between baryons (neutrons, protons, and possibly hyperons). The starting point is the construction of a relativistic Lagrangian, which is a sum of free-particle Dirac terms for the baryons and leptons, plus free-particle terms for the mesons (scalar σ, vector ω, and isovector ρ), plus interaction terms including tree-level meson-baryon interactions and perturbative self-interactions for the σ meson. This makes the theory a phenomenological low-energy effective field theory, although it has the advantage of being many-particle and relativistic by construction so that the sound speed never exceeds the speed of light. It also has a small number of parameters which can be fit simply to experiment, although this is a mixed blessing since the many numbers known from nuclear experiments must be distilled to a few. Mean-field theory also has the disadvantage that it neglects correlations by construction.

Under the assumption that the bulk matter is (on a macroscopic scale) static and homogeneous, the fields are replaced by their mean values, time and spatial derivatives vanish, and the Euler-Lagrange equations take a form that is relatively simple to solve but is still somewhat lengthy and thus we do not reproduce it here. It is enough to state that the Euler-Lagrange equations in this approximation reduce to a set of coupled algebraic equa-

tions for the lepton and baryon Fermi momenta and the meson fields. These are combined with equations for generalized β-equilibrium, electric charge conservation, and conservation of baryon number to obtain the Fermi momenta and meson fields as functions of, for example, the total baryon number density. These are then used to construct the pressure and energy density, i.e. the equation of state.

The Euler-Lagrange equations feature five free parameters, which under certain assumptions are fit algebraically to numbers distilled from laboratory measurements of many finite nuclei: the saturation density, binding energy per nucleon and isospin asymmetry coefficient at saturation density, and the overall incompressibility K and effective mass m^* of nucleons in the nuclear medium. The latter two are difficult to estimate from available data and are subject to systematic uncertainties, and thus papers using this relativistic set of equations of state typically treat a range of values for K (240–300 MeV) and m^* (0.70–0.80 times the nucleon mass m). (The compressibilities are typically lower for nonrelativistic models.)

At roughly twice nuclear density in these equations of state, the neutron Fermi momentum is high enough to make hyperon production favorable in spite of the roughly 200 MeV/c^2 mass difference. The hyperons of most interest are the Λ and Σ^- hyperons, which have the lowest masses and therefore are created at the lowest densities and occupy the largest fraction of the volume of a star. However, the other hyperons Σ^0, Σ^+, Ξ^-, and Ξ^0 also appear in small numbers at the very highest densities. Hyperons introduce more free parameters. The hyperon-meson couplings are assumed to be the same for all hyperons but are weaker than the nucleon-meson couplings by the ratios x_σ, x_ω, and x_ρ for the three mesons. The former two ratios are obtained algebraically from the measured binding of Λ hyperons in nuclear matter (double-Λ hypernuclei) and (more roughly) from hypernuclear energy levels, resulting in $x_\sigma \leq 0.72$ (usually taken to be $x_\sigma = 0.6$) and x_ω being determined as a function of x_σ and m^*. [Note that the first Table in Ref. [54] contains a typo which is repeated in Ref. [32]: The value of x_ω reading 0.568 should read 0.658, as can be seen by solving Eq. (5.59) of the latter reference.] The remaining ratio x_ρ is unconstrained by hypernuclear data, since the Λ is isospin neutral and the relevant Σ^- hypernuclear measurements are highly uncertain. As is standard practice, we set $x_\rho = x_\sigma$, although the final equation of state is rather insensitive to the precise value [32].

Numerically, we construct these equations of state using the methods of Ref. [32] as functions of the most uncertain parameters m^*, K, and x_σ. (The low density equation of state is the standard BPS model [64], but this has little effect on the mass-radius curve which is the subject of our work.) For all cases we also use the values 0.153 fm^{-3} for the saturation density, -16.3 MeV for the binding energy per baryon at that density, and 32.5 MeV for the isospin symmetry energy coefficient at that density, all as in Ref. [32]. We use seven fiducial equations of state of this type: Three sets of values from Ref. [32] are already in common use in the literature: $K = 240$ MeV and $m^*/m = 0.78$, the softest

choice which we denote H1; $K = 300$ MeV and $m^*/m = 0.78$, an intermediate choice denoted H2; and $K = 300$ MeV and $m^*/m = 0.70$, the stiffest of these equations of state denoted H3. All use $x_\sigma = 0.6$. We construct the stiffest such equation of state compatible with experimental data (H4) using $K = 300$ MeV, $m^*/m = 0.70$, and $x_\sigma = 0.72$. We construct three others (H5–H7) for extreme values of K and m^* with x_σ just satisfying the astronomical constraints (see below and Fig. 3.3). These parameter values are summarized in Table 3.1. We also construct relativistic mean field equations of state without hyperons by artificially setting the hyperon masses to arbitrarily high values. These are denoted G1–G7 correspondingly, but note that G3 is identical to G4.

The second type of equation of state is based on detailed modeling of the potentials observed in laboratory nuclei, such as done in Ref. [40]. That paper, denoted APR, gives the canonical Schrödinger (non-relativistic) model including detailed potentials, two- and three-body interactions, and with some relativistic effects in the form of perturbations. It has the advantage of using more of the known experimental numbers than relativistic mean-field theory, including correlations and scattering data. However, the fitting to experimental numbers is more involved, while there are in the end only a few numbers that characterize bulk matter and neutron-star structure. These equations of state are few-body by construction and are fundamentally nonrelativistic, resulting in causality violation at high densities (the sound speed exceeds the speed of light). Since we expect the recent observations to rule out softer equations of state, we also consider a very soft version of this type denoted BPAL12 in Ref. [41]. The incompressibility of BPAL12 is 120 MeV, which was known at the time to be much too low. It was created explicitly to produce "artificially" the softest equation of state compatible with then-known neutron star masses (1.45 $M_\odot$). Since neither of these equations of state includes hyperons, we also consider the results of Balberg, Lichtenstadt, and Cook [65], who include hyperons in a similar model, and denote their equations of state as BLC1 (the softer) and BLC2 (the stiffer).

Table 3.1: Parameters for seven fiducial hyperonic equations of state in relativistic mean field theory. Corresponding equations of state without hyperons are denoted G1–G7, but G3 and G4 are identical.

Name	K (MeV)	m^*/m	x_σ
H1	240	0.78	0.60
H2	300	0.78	0.60
H3	300	0.70	0.60
H4	300	0.70	0.72
H5	300	0.80	0.66
H6	240	0.70	0.67
H7	240	0.80	0.69

3.3 Maximum mass

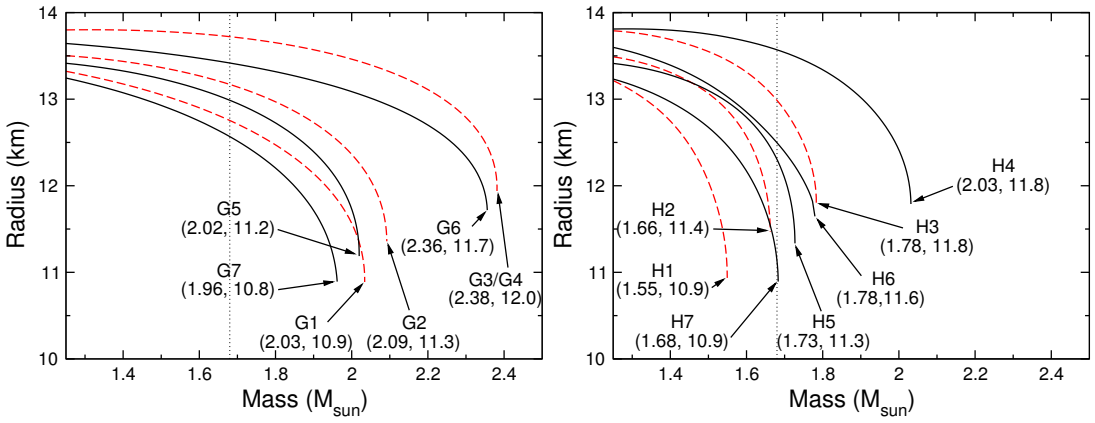

Figure 3.1: Oppenheimer-Volkoff mass-radius curves for the fiducial relativistic mean field equations of state with hyperons (right) and without hyperons (left). The vertical line is the observational 95% confidence limit 1.68 $M_\odot$ from Ter 5 I. H1 is ruled out by the observation. H2 is marginally consistent, allowing for a small increase in maximum mass due to rotation and the imprecision of the constraint.

General relativity predicts a maximum mass for a star stable to radial perturbations for a given equation of state. This is seen by solving the well-known Oppenheimer-Volkoff (OV) equations, which map a curve $p(\rho)$ (pressure as a function of energy density) onto a curve $M(R)$ (mass of the star as a function of radius). The gravitational mass M generically has a maximum, which rules out equations of state that are too soft to produce the observed masses. The tightest observational constraint at 95% confidence is now 1.68 $M_\odot$ for Ter 5 I [43], though the corresponding 1.6 $M_\odot$ for PSR J0751+1807 [44] may be cleaner. While PSR J0751+1807 has a 287 Hz rotation frequency [66], this is well below the mass-shedding limit for all equations of state and can be shown to increase the OV maximum mass (which assumes no rotation) by no more than about 2–3 percent [67]. Ter 5 I rotates at 104 Hz [43], and thus its maximum mass is increased by less than 1% over the OV value.

We use a version of the OV equations due to Lindblom [68]:

$$\frac{dm}{dh} = -\frac{4\pi\rho(h)r(h)^3[r(h)-2m(h)]}{m(h)+4\pi r(h)^3 p(h)}, \tag{3.1}$$

$$\frac{dr}{dh} = -\frac{r(h)[r(h)-2m(h)]}{m(h)+4\pi r(h)^3 p(h)}, \tag{3.2}$$

using as independent variable the specific enthalpy

$$h(p) = \int_0^p dp'/[p'+\rho(p')]. \tag{3.3}$$

(Here $G = c = 1$.) Unlike the standard OV equations for $m(r)$ (the mass contained within a sphere of radius r) and $p(r)$, Lindblom's form does not suffer numerical difficulties near the surface of the star, which is simply and robustly defined by $h = 0$. We start by picking a central enthalpy and evaluating an analytical expansion of the equations at a point very close to the center of the star (where the equations are singular). We then integrate down to $h = 0$ and read off the total mass and radius of the star as $M = m(0)$ and $R = r(0)$.

In Fig. 3.1 we plot $R(M)$ for our fiducial relativistic mean-field equations of state, with hyperons (right) and without hyperons (left). All equations of state without hyperons are consistent with 1.68 $M_\odot$. The softest one with hyperons (H1) has a maximum mass of 1.55 $M_\odot$ and is ruled out by the new pulsar observations [43, 44]. H2 is nominally inconsistent with the 95% confidence limit of 1.68 $M_\odot$ for Ter 5 I. However, in practice H2 cannot be ruled out by this observation and must be considered marginally consistent because rotation (not included in the OV model) can account for most of the 0.02 $M_\odot$ difference and changing the confidence level very slightly from 95% would bring it within the limit. At the 68% confidence level for PSR J0751+1807 [44] (1.8 $M_\odot$), only the stiffest equation of state with hyperons (H3) is marginally allowed, while again all equations of state without hyperons are allowed.

Of the potential-based equations of state (plotted in [40, 65]), BPAL12 is firmly ruled out with a maximum mass of 1.45 $M_\odot$ (at a radius of 9.0 km). This is not too surprising, since BPAL12 was deliberately constructed with an artificially low incompressibility $K = 120$ MeV as an extreme example. The extremely soft example for this type of equation of state should now be BPAL21, which has a maximum mass of 1.67 $M_\odot$ for a nonrotating star (the 95% confidence limit from Ter 5 I) at a radius of 9.2 km. The hyperonic BLC1 equation of state has a maximum mass of 1.55 $M_\odot$, which is also firmly ruled out. The stiffer BLC2 has a maximum mass of 1.75 $M_\odot$, which is compatible with the 95% confidence limit of Ter 5 I. APR stars have a maximum mass of 2.2 $M_\odot$, compatible with all constraints.

3.4 Gravitational redshift

General relativity also predicts a redshift for photons leaving the surface of a star with a strong gravitational field. For a nonrotating star the redshift z obeys the relation

$$1 + z = \left(1 - \frac{2GM}{c^2 R}\right)^{-1/2}. \tag{3.4}$$

Since R decreases with M as M approaches its maximum for a stable star, z generically has a maximum for the maximum-mass star and an observation can rule out equations of state which cannot produce a strong enough redshift. Cottam, Paerels, and Mendez [45] have such an observation, a gravitational redshift $z = 0.35$ obtained by identifying several absorption

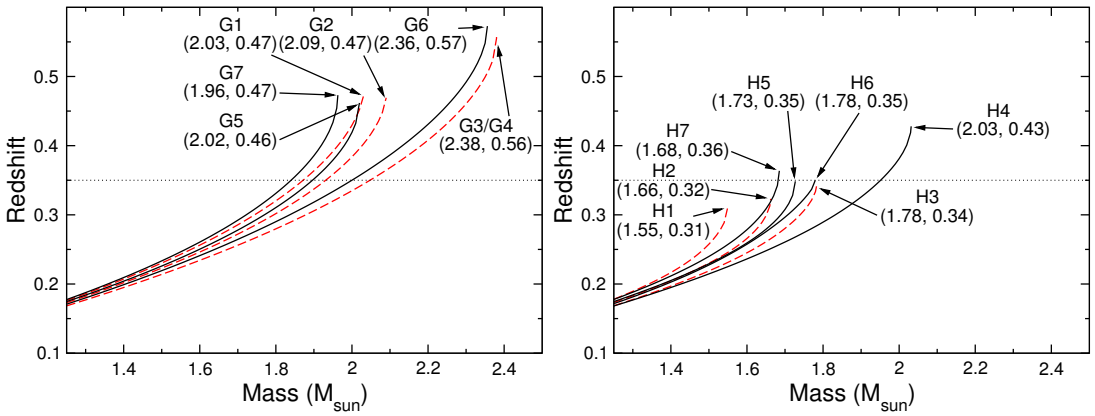

Figure 3.2: Gravitational redshift vs. mass for relativistic mean field theory equations of state with hyperons (right) and without hyperons (left). The horizontal line is $z = 0.35$ measured for EXO0748-676. H1 and H2 are ruled out, even allowing for the estimated measurement errors. H3, formerly considered the "stiff" equation of state, is actually the softest compatible with the redshift. H5 through H7 barely satisfy the redshift constraint by construction (see the next Figure).

lines in spectra constructed from multiple bursts from the low-mass x-ray binary EXO0748-676. Due to the number of consistent lines the result is robust, although there may be errors at the few percent level [63]. Pulsations from a more recent x-ray burst have inferred a rotation frequency of 45 Hz for the neutron star [69]. At this frequency rotational corrections to the redshift should be a fraction of a percent [63] and the nonrotating approximation suffices.

The redshift as a function of mass is plotted for the fiducial relativistic mean-field equations of state in Fig. 3.2 and compared to the observational constraint from EXO0748-676. Without hyperons, all equations of state are consistent with $z = 0.35$ for masses greater than the 1.4 $M_\odot$ typical of previous measurements, consistent with the suspected higher masses of accreting stars in x-ray binaries. With hyperons, only the stiffest of the usual equations of state (H3) is marginally consistent with $z = 0.35$. Therefore we favor using H3 as the new "soft" equation of state of this type and H4 as the stiffest. In fact, varying values of the nuclear incompressibility K and nucleon effective mass m^* allow for several "soft" equations of state marginally consistent with the redshift, as shown in Fig. 3.3. Although H3 nominally has $z \leq 0.34$, it should be considered marginally consistent because there may be measurement errors of order 5% [63] and, more importantly, the maximum redshift is extremely sensitive to the equation of state at several times nuclear density. For example, artificially excluding all hyperons but the Λ and Σ^- raises the maximum redshift by 0.03 (a 10% correction), even though the populations of those hyperons are very small.

Of the potential-based equations of state, BPAL12 is marginal with $z \leq 0.36$ while all the others (including those with hyperons) easily meet the observational constraint, even

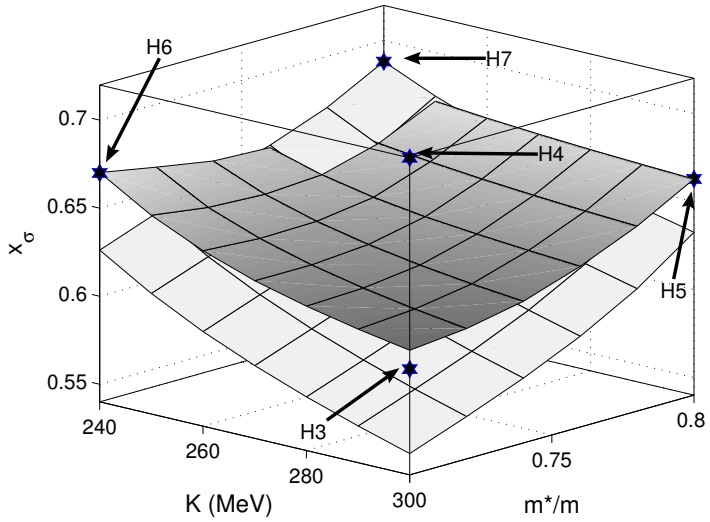

Figure 3.3: Relativistic mean field theory equations of state can be described by incompressibility K (in MeV), effective nucleon mass m^*/m, and scalar meson-hyperon coupling x_σ (see text). The dark surface marks those equations of state with a maximum redshift of 0.35. Equations of state below the surface are incompatible with the observed redshift of EXO0748-676. While H3 is below the surface, it is within the estimated 5% error bar and should be considered marginally allowed. Equations of state above the lighter surface are compatible with the 95% confidence limit on the mass of Ter 5 I. The points corresponding to our fiducial equations of state are indicated.

when the maximum masses are similar to the relativistic mean-field theory models. This is because the maximum-mass stars have 11 km radii in the relativistic models and 9 km radii in the nonrelativistic ones. Radii in general are approximately determined by the pressure near nuclear density [50], which in relativistic mean-field theory is about twice what it is for potential-based models. Physically this has the simple explanation that most of the matter in the neutron star is within a factor of two of nuclear density, and so the pressure at higher densities matters less for the typical radius (though it is important for the maximum mass). The fact that the redshift does not constrain the potential-model equations of state suggests that their low pressure near nuclear density may be favored (in the sense that there is more unconstrained parameter space). However, at high densities these models violate causality, which then favors the relativistic mean field models at high density.

Rather than using a set of fiducial equations of state, one can invert the problem to ask "Given an observation of $z = 0.35$, what parameters in relativistic mean-field theory with hyperons are compatible with it?" As stated in Sec. II, the three main parameters are x_σ, K, and m^*/m. If we put them all at the stiff end of their allowed ranges consistent with nuclear and hypernuclear experiment, we obtain equation of state H4 with a maximum

redshift $z = 0.43$. If we soften the equation of state by lowering x_σ (and thus x_ω and x_ρ) while keeping the other parameters fixed at the H4 values, we get $z = 0.35$ at $x_\sigma = 0.61$. Similarly, softening the equation of state by lowering K or raising m^*/m results in bounds of $K \geq 210$ MeV or $m^*/m \leq 0.84$ respectively, both of which are less stringent than the experimental bounds [32]. A plot showing the redshift constraint surface (and Ter 5 I mass constraint surface) in the three-parameter space is shown in Fig 3.3. The boundaries of the cube correspond to the parameter ranges inferred from experiment, except for x_σ where the experimental lower bound is far below the redshift constraint surface. The redshift seems to be most sensitive to the hyperonic coupling parameter x_σ, and fairly insensitive to the incompressibility K which is traditionally considered the measure of stiffness. This can be seen from the fact that the redshift constraint surface in Fig. 3.3 is fairly flat and that x_σ is the only difference between H3 and H4. (The mass constraint surface is tilted, *i.e.* more correlated with K and m^*.) The physical explanation is that the main hyperon interaction at high densities is the repulsion (represented in this framework by the vector meson ω), and thus increasing the coupling constants decreases the hyperon population of a given star. Hyperons, and any other new degrees of freedom, soften the equation of state at high densities and thus reduce the maximum mass and redshift.

There is also a very recent discussion of a measured $z = 0.4$ in the x-ray binary 4U 1700+24 by Tiengo *et al.* [70], but it is very tentative. This redshift comes from one spectral line, which is probably better explained by $z = 0.012$ (implying emission well away from the surface of the star), and there are no other spectral features consistent with $z = 0.4$. H4 would still be compatible with such a redshift, but would be fairly marginal.

3.5 Conclusion

We have compared equations of state for hyperon stars with new astronomical observations of mass and gravitational redshift. Nonrelativistic potential-based models are not greatly constrained by the new observations. Relativistic mean-field theory models, however, are tightly constrained by the observed gravitational redshift. In fact, the stiffest of these models commonly used in the literature (which we denote H3) is so soft as to be only marginally compatible with the observation. When the full range of parameters consistent with experiments on hypernuclei is considered, there are still many such equations of state allowed and the hyperon coupling parameter is found to be the main one determining the redshift. As a consequence we advocate that future studies involving these models use H3 and a new set of canonical parameter values which we denote as equations of state H4–H7 (see the Appendix). If through further observations the 95% confidence limit on the mass of the neutron star in PSR J0751+1807 is narrowed to the present 68% confidence limit, it would rule out all but H4.

Moving away from the details of a specific model, the general physical result is this: The presence of hyperons in neutron stars is constrained but not ruled out by the gravitational redshift observation (and to a lesser extent by high mass observations). In general the equations of state that survive are stiffer than the range previously considered in the literature. This means that the hyperons are less numerous, reducing for example the effect of enhanced cooling and bulk viscosity, which is a subject for future work [47]. It may also be useful to consider phenomenological equations of state that behave like potential-based models near nuclear density but like relativistic mean-field models at higher densities.

3.6 Appendix

For many purposes the detailed microscopic properties of a matter model are unnecessary, and all that is desired is a tabulation of pressure, energy density, and baryon number density. In Tables II, III, IV, V, and VI we provide these for equations of state H3–H7. The low density ($n < 0.3$) parts of some of these (before hyperons or other strange matter appear) are the same as in Ref. [32]. We duplicated the procedure of Glendenning [32] from the beginning using constants from Ref. [71], which leads to some discrepancies in the third or fourth significant figure.

All equations of state but H6 are given up to a baryon density $n = 1.2$ fm^{-3}, which is more than sufficient for stable nonrotating stars. We stop H6 at $n = 0.81$ because at high densities the effective mass of the proton becomes negative. This indicates a limitation of the Lagrangian, which was posited as a low-energy effective theory. In practice this is not an issue since $n = 0.81$ is almost the central density of the maximum-mass nonrotating H6 star. We find that extrapolating H6 beyond $n = 0.81$ under a wide range of assumptions only changes the maximum mass of a stable star by 1%.

Table 3.2: Baryon number density n (fm^{-3}), energy density ρ ($\mathrm{erg/cm}^3$), and pressure p ($\mathrm{dyn/cm}^2$) for H3.

n	ρ	p	n	ρ	p
0.03	5.041e+13	3.581e+31	0.63	1.221e+15	1.842e+35
0.06	1.009e+14	3.148e+32	0.66	1.290e+15	2.024e+35
0.09	1.518e+14	1.237e+33	0.69	1.359e+15	2.217e+35
0.12	2.031e+14	3.124e+33	0.72	1.430e+15	2.407e+35
0.15	2.549e+14	6.126e+33	0.75	1.501e+15	2.597e+35
0.18	3.073e+14	1.040e+34	0.78	1.573e+15	2.791e+35
0.21	3.604e+14	1.624e+34	0.81	1.646e+15	2.991e+35
0.24	4.144e+14	2.389e+34	0.84	1.720e+15	3.197e+35
0.27	4.694e+14	3.360e+34	0.87	1.794e+15	3.408e+35
0.30	5.263e+14	4.261e+34	0.90	1.870e+15	3.596e+35
0.33	5.846e+14	5.122e+34	0.93	1.946e+15	3.773e+35
0.36	6.440e+14	6.107e+34	0.96	2.023e+15	3.950e+35
0.39	7.044e+14	7.236e+34	0.99	2.100e+15	4.125e+35
0.42	7.658e+14	8.417e+34	1.02	2.178e+15	4.301e+35
0.45	8.282e+14	9.588e+34	1.05	2.256e+15	4.478e+35
0.48	8.914e+14	1.083e+35	1.08	2.336e+15	4.657e+35
0.51	9.556e+14	1.215e+35	1.11	2.416e+15	4.837e+35
0.54	1.021e+15	1.357e+35	1.14	2.496e+15	5.019e+35
0.57	1.087e+15	1.508e+35	1.17	2.577e+15	5.202e+35
0.60	1.153e+15	1.670e+35	1.20	2.659e+15	5.386e+35

Table 3.3: Same as the previous Table, but for H4.

n	ρ	p	n	ρ	p
0.03	5.041e+13	3.581e+31	0.63	1.242e+15	2.416e+35
0.06	1.009e+14	3.148e+32	0.66	1.315e+15	2.685e+35
0.09	1.518e+14	1.237e+33	0.69	1.390e+15	2.972e+35
0.12	2.031e+14	3.124e+33	0.72	1.466e+15	3.260e+35
0.15	2.549e+14	6.126e+33	0.75	1.543e+15	3.556e+35
0.18	3.073e+14	1.040e+34	0.78	1.621e+15	3.863e+35
0.21	3.604e+14	1.624e+34	0.81	1.701e+15	4.182e+35
0.24	4.144e+14	2.389e+34	0.84	1.782e+15	4.512e+35
0.27	4.694e+14	3.360e+34	0.87	1.865e+15	4.856e+35
0.30	5.256e+14	4.561e+34	0.90	1.949e+15	5.191e+35
0.33	5.839e+14	5.711e+34	0.93	2.034e+15	5.517e+35
0.36	6.438e+14	6.924e+34	0.96	2.120e+15	5.847e+35
0.39	7.050e+14	8.313e+34	0.99	2.208e+15	6.183e+35
0.42	7.676e+14	9.883e+34	1.02	2.296e+15	6.525e+35
0.45	8.315e+14	1.149e+35	1.05	2.386e+15	6.875e+35
0.48	8.967e+14	1.321e+35	1.08	2.476e+15	7.232e+35
0.51	9.631e+14	1.508e+35	1.11	2.569e+15	7.597e+35
0.54	1.031e+15	1.710e+35	1.14	2.662e+15	7.969e+35
0.57	1.100e+15	1.928e+35	1.17	2.756e+15	8.346e+35
0.60	1.170e+15	2.164e+35	1.20	2.852e+15	8.727e+35

Table 3.4: Same as the previous Table, but for H5.

n	ρ	p	n	ρ	p
0.03	5.045e+13	4.568e+31	0.63	1.207e+15	1.720e+35
0.06	1.010e+14	2.739e+32	0.66	1.274e+15	1.879e+35
0.09	1.518e+14	1.123e+33	0.69	1.343e+15	2.045e+35
0.12	2.032e+14	2.929e+33	0.72	1.412e+15	2.219e+35
0.15	2.549e+14	5.788e+33	0.75	1.482e+15	2.401e+35
0.18	3.073e+14	9.754e+33	0.78	1.552e+15	2.591e+35
0.21	3.602e+14	1.494e+34	0.81	1.624e+15	2.789e+35
0.24	4.140e+14	2.139e+34	0.84	1.697e+15	2.995e+35
0.27	4.686e+14	2.916e+34	0.87	1.770e+15	3.209e+35
0.30	5.241e+14	3.827e+34	0.90	1.844e+15	3.431e+35
0.33	5.806e+14	4.874e+34	0.93	1.919e+15	3.660e+35
0.36	6.388e+14	5.840e+34	0.96	1.995e+15	3.898e+35
0.39	6.982e+14	6.819e+34	0.99	2.071e+15	4.136e+35
0.42	7.586e+14	7.883e+34	1.02	2.149e+15	4.377e+35
0.45	8.199e+14	9.040e+34	1.05	2.227e+15	4.623e+35
0.48	8.822e+14	1.029e+35	1.08	2.306e+15	4.875e+35
0.51	9.454e+14	1.156e+35	1.11	2.386e+15	5.132e+35
0.54	1.010e+15	1.287e+35	1.14	2.466e+15	5.396e+35
0.57	1.074e+15	1.424e+35	1.17	2.548e+15	5.666e+35
0.60	1.140e+15	1.558e+35	1.20	2.630e+15	5.942e+35

Table 3.5: Same as the previous Table, but for H6.

n	ρ	p	n	ρ	p
0.03	5.038e+13	2.458e+31	0.45	8.220e+14	8.987e+34
0.06	1.009e+14	3.597e+32	0.48	8.846e+14	1.026e+35
0.09	1.517e+14	1.380e+33	0.51	9.481e+14	1.166e+35
0.12	2.031e+14	3.308e+33	0.54	1.013e+15	1.320e+35
0.15	2.549e+14	6.183e+33	0.57	1.078e+15	1.489e+35
0.18	3.073e+14	1.001e+34	0.60	1.145e+15	1.674e+35
0.21	3.603e+14	1.513e+34	0.63	1.212e+15	1.875e+35
0.24	4.139e+14	2.160e+34	0.66	1.281e+15	2.090e+35
0.27	4.685e+14	2.974e+34	0.69	1.350e+15	2.299e+35
0.30	5.241e+14	3.933e+34	0.72	1.421e+15	2.512e+35
0.33	5.816e+14	4.709e+34	0.75	1.493e+15	2.732e+35
0.36	6.402e+14	5.588e+34	0.78	1.565e+15	2.959e+35
0.39	6.998e+14	6.621e+34	0.81	1.639e+15	3.188e+35
0.42	7.604e+14	7.807e+34			

Table 3.6: Same as the previous Table, but for H7.

n	ρ	p	n	ρ	p
0.03	5.039e+13	3.353e+31	0.63	1.195e+15	1.621e+35
0.06	1.009e+14	3.585e+32	0.66	1.261e+15	1.777e+35
0.09	1.518e+14	1.329e+33	0.69	1.328e+15	1.942e+35
0.12	2.031e+14	3.151e+33	0.72	1.396e+15	2.116e+35
0.15	2.549e+14	5.842e+33	0.75	1.465e+15	2.298e+35
0.18	3.072e+14	9.426e+33	0.78	1.535e+15	2.488e+35
0.21	3.601e+14	1.401e+34	0.81	1.605e+15	2.715e+35
0.24	4.136e+14	1.966e+34	0.84	1.677e+15	2.897e+35
0.27	4.678e+14	2.645e+34	0.87	1.749e+15	3.114e+35
0.30	5.228e+14	3.442e+34	0.90	1.822e+15	3.339e+35
0.33	5.787e+14	4.362e+34	0.93	1.896e+15	3.572e+35
0.36	6.356e+14	5.349e+34	0.96	1.971e+15	3.812e+35
0.39	6.942e+14	6.252e+34	0.99	2.047e+15	4.059e+35
0.42	7.537e+14	7.227e+34	1.02	2.124e+15	4.309e+35
0.45	8.140e+14	8.292e+34	1.05	2.201e+15	4.564e+35
0.48	8.752e+14	9.454e+34	1.08	2.279e+15	4.825e+35
0.51	9.374e+14	1.071e+35	1.11	2.358e+15	5.093e+35
0.54	1.000e+15	1.199e+35	1.14	2.438e+15	5.369e+35
0.57	1.064e+15	1.332e+35	1.17	2.519e+15	5.651e+35
0.60	1.129e+15	1.473e+35	1.20	2.601e+15	5.941e+35

Chapter 4

R-modes and bulk viscosity of hyperonic matter

In this chapter we provide background for Chapter 5, which was written as a technical article [47]. For a review of issues related to r-modes see Stergioulas [72].

4.1 R-modes and their instability

Disturbances caused during the birth of a neutron star, or resulting from infalling material in accreting neutron stars can cause the excitation of normal oscillation modes of neutron stars. These oscillations result in time varying multipole moments which cause the emission of gravitational radiation.

In certain instances gravitational radiation tends to drive oscillation modes rather than damp them. This instability, known as the Chandrasekhar-Friedman-Schutz (CFS) instability [37, 38], stems from a disagreement between two frames of reference. The instability occurs when a neutron star oscillation mode that is prograde in an inertial frame appears retrograde in the corotating frame of the star. This follows from the angular momentum associated with a retrograde mode in the corotating frame being negative, and the assumption that the mode perturbation is small. The 'canonical' energy associated with the mode is also negative. Therefore, when the neutron star loses positive angular momentum (and energy) through gravitational radiation, the loss appears as a larger value of the negative angular momentum (and energy) associated with the mode, i.e. as growth of the mode. The increased perturbation causes an increase in gravitational radiation which in turn causes further growth of the mode. In this fashion the CFS instability can cause the mode to grow until non-linear effects take over.

Mathematically, the requirement of disagreement between the frames is the condition

$$\omega(\omega + m\Omega) < 0, \tag{4.1}$$

which follows from the expression for the rate at which the gravitational radiation causes

the energy of a mode to grow [73]:

$$\frac{d\tilde{E}}{dt} = -\omega(\omega + m\Omega) \sum_{l \geq 2} N_l \omega^{2l} \left(|\delta D_{lm}|^2 + |\delta J_{lm}|^2 \right). \tag{4.2}$$

Here ω is the angular frequency of the mode in the inertial frame, Ω is the spin angular frequency of the star, m is the azimuthal quantum number, l is the angular quantum number, D_{lm} and J_{lm} are mass and current multipoles respectively, and N_l is given by

$$N_l = \frac{4\pi G}{c^{2l+1}} \frac{(l+1)(l+2)}{l(l-1)[(2l+1)!!]^2}. \tag{4.3}$$

If we identify the term within the parenthesis in Eq. (4.1) as the angular frequency of the mode in the co-rotating frame, we can see that Eq. (4.1) would be satisfied if the frequencies in the inertial and corotating frames have opposing signs. This identification is made by explaining the relationship between the frequency of the mode and its pattern speed. The pattern speed of a mode is the angular velocity at which surfaces of constant phase of the mode move. For a perturbation of the form $\exp[i(m\phi + \omega t)]$ the pattern speed is given by $-\omega/m$. The *relative* pattern speed in the co-rotating frame is given by:

$$-\frac{\omega_r}{m} = -\frac{\omega_i}{m} - \Omega, \tag{4.4}$$

where, ω_m is the frequency in the co-rotating frame. This equation can be rearranged to obtain

$$\omega_r = \omega_i + m\Omega, \tag{4.5}$$

and hence the identification.

R-modes are a class of axial modes whose dynamics is governed by the Coriolis force[1]. *R*-modes are similar to Rossby waves that are found in the oceans of the Earth. Although they have been studied by astrophysicists since the 1970s [74], they became an active topic of research in the late 1990s with the discovery that they are unstable to gravitational radiation in perfect fluid stars for *all* values of m and Ω [75]. This result was explicitly proved by Friedman and Morsink [76] soon afterwards. Soon followed two independent calculations [73, 77] which showed that they would be unstable even in real stars, where viscous processes tend to damp any type of oscillations. The first detailed study related to the detectability of gravitational radiation from these modes was made by Owen et al [78]. It was also proposed that gravitational radiation from these modes could be responsible for limiting the spin frequencies in LMXBs [28, 36].

[1] To get better acquainted with the structure of these modes see the animation here. (*http* : *//phys.psu.edu/people/display/index.html?person_id* = 484; *mode* = *research*; *research_description_id* = 333).

R-modes are characterized by their velocity perturbation

$$\delta\vec{v} = \alpha R\Omega \left(\frac{r}{R}\right)^l \vec{Y}^B_{ll} e^{i\omega t} + \mathcal{O}(\Omega^3), \tag{4.6}$$

where R is the radius of the unperturbed star (which is spherical in the limit of small Ω), α is an arbitrary dimensionless constant, and $\vec{Y}^B_{lm}$ is the magnetic-type vector spherical harmonic defined by

$$\vec{Y}^B_{lm} = [l(l+1)]^{-1/2} r\vec{\nabla} \times (r\vec{\nabla} Y_{lm}), \tag{4.7}$$

where Y_{lm} is the scalar spherical harmonic. The frequency of the r-modes in the inertial frame is given by [74]

$$\omega_i = -\frac{(l-1)(l+2)}{l+1}\Omega + \mathcal{O}(\Omega^3). \tag{4.8}$$

The negative sign of the frequency implies a positive pattern speed and hence the mode is prograde in the inertial frame. The frequency in the co-rotating frame is obtained using Eq. (4.5) and the fact that only modes that have $l = m$ are present in neutron stars with barotropic equations of state [79]:

$$\omega_r = \frac{2}{l+1}\Omega + \mathcal{O}(\Omega^3). \tag{4.9}$$

The positive sign of the frequency implies that the pattern speed in the co-rotating frame is negative and the mode is retrograde in this frame. The two Eqs. (4.8) and (4.9) satisfy the condition for CFS instability Eq. (4.1).

Real neutron stars are not perfect fluids, and thus viscous (and other) damping mechanisms compete with gravitational wave driving of the oscillation modes. The strength of the driving and damping mechanisms, expressed as timescales, determines if a mode is unstable or not. The mode is unstable if the driving timescale is shorter than the viscous damping timescale. This can be expressed in terms of an overall mode timescale τ_n such that

$$\frac{1}{\tau_n(\Omega, T)} = \frac{1}{\tau_{GR}(\Omega)} + \frac{1}{\tau_V(\Omega, T)} \tag{4.10}$$

where $\tau_{GR} < 0$ is the damping timescale of the mode due to gravitational radiation and $\tau_V > 0$ is the damping timescale resulting from the sum of all viscous processes in the star. The star's spin angular frequency and temperature are represented by Ω and T, respectively. A mode unstable to gravitational radiation corresponds to $\tau_n < 0$ in Eq. (4.10), and the angular frequency corresponding to the point where the two timescales are equal, $1/\tau_n(\Omega_c, T) = 0$, is called the critical frequency Ω_c.

The gravitational radiation timescale is given by

$$\frac{1}{\tau_{GR}} = -\frac{1}{2\tilde{E}}\left(\frac{d\tilde{E}}{dt}\right)_{GR}, \tag{4.11}$$

where $\tilde{E}$ is the mode energy in a frame rotating with the star and $(d\tilde{E}/dt)_{GR}$ is the rate at which energy is emitted in gravitational waves in the same frame. The energy of an $l = 2$ r-mode is given by

$$\tilde{E} = \frac{1}{2}\alpha^2\Omega^2 R^{-2}\int_0^R \epsilon(r) r^6 dr, \tag{4.12}$$

where ϵ is the energy density.

Gravitational radiation at the lowest order couples to r-modes through the current quadrupole moment and not the mass quadrupole moment as is usually the case. This follows from the fact that the lowest order density perturbation is of order Ω^2 and not Ω [73]. The expressions for the mass and current multipole moments that appear in Eq. (4.2) are

$$\delta D_{lm} = \int \delta\epsilon\, r^l Y^*_{lm} d^3x, \tag{4.13}$$

$$\delta J_{lm} = 2\sqrt{\frac{l}{l+1}}\int r^l(\epsilon\,\delta\vec{v} + \delta\epsilon\,\vec{v})\cdot\vec{Y}^{B*}_{l\,m} d^3x, \tag{4.14}$$

where $\vec{v}$ is the velocity of the mode. It is clear from Eq. (4.13)that the $\mathcal{O}(\Omega)$ mass multipoles are all identically zero since the lowest order density perturbation is of order Ω^2. The $\mathcal{O}(\Omega)$ current multipole moments are non-zero as can be seen by substituting Eq. (4.6) into Eq. (4.14):

$$\delta J_{ll} = \frac{2\alpha\Omega}{R^{l-1}}\sqrt{\frac{l}{l+1}}\int_0^R \epsilon\, r^{2l+2} dr. \tag{4.15}$$

We can now determine the net gravitational radiation growth time. We first substitute Eq. (4.15) into Eq. (4.2) to obtain the rate at which the gravitational wave instability is pumping energy into the mode. We then substitute the resultant expression into Eq. (4.11) to obtain

$$\frac{1}{\tau_{GR}} = -\frac{243\pi G\,\Omega^6}{600\,c^7}\int_0^R \epsilon(r) r^6\, dr. \tag{4.16}$$

To obtain the above expression we have used Eq. (4.9) and the fact that the most dominant r-mode is the $l = m = 2$ mode. In Eq. (4.15) α is a dimensionless amplitude coefficient which cancels out of the linear driving and damping timescales.

R-modes are more likely to survive in stars than other types of modes for a variety of reasons. Other types of modes are unstable to the CFS instability only above some minimum values of m and Ω. They become unstable only at high values of Ω close to the

Kepler limit [2] and are therefore likely to be stable in most stars. The requirement of high m for modes other than r-modes makes it likely that they are dominated by some form of viscosity for two reasons: firstly, the gravitational radiation growth timescale increases with m, and secondly, viscous damping time decreases with m. Another factor that makes it more likely for r-modes to survive viscosity in real stars is that the rate at which bulk viscosity damps r-modes is at a higher order in Ω than other modes. The expression for the rate at which viscous processes drain energy from a mode is given by

$$\frac{d\tilde{E}}{dt} = -\int \left(2\eta\delta\sigma^{ab}\delta\sigma^{*}_{ab} + \zeta\delta\sigma\delta\sigma^{*}\right) d^3x. \tag{4.17}$$

Here η and ζ are the coefficients of shear and bulk viscosity respectively i.e. the first term is the contribution from shear viscosity while the second is from bulk viscosity. The shear $\delta\sigma_{ab}$ and expansion $\delta\sigma$ are given, respectively, by

$$\delta\sigma_{ab} = \tfrac{1}{2}(\nabla_a\delta v_b + \nabla_b\delta v_a - \tfrac{2}{3}\delta_{ab}\nabla_c\delta v^c), \tag{4.18}$$

$$\delta\sigma = \nabla_a\delta v^a. \tag{4.19}$$

The expansion $\delta\sigma$ to the lowest order in Ω ($\mathcal{O}(\Omega)$) is zero as can be seen by using the r-mode velocity perturbation Eq. (4.6) in the expression for the expansion Eq. (4.19) and using the identity

$$\vec{\nabla}\cdot(\vec{\nabla}\times\vec{A}) = 0, \tag{4.20}$$

which holds for any vector $\vec{A}$. Therefore, the lowest order contribution to the bulk viscosity for r-mode damping results from a shear of the order Ω^2. For other modes the expansion at the lowest order in Ω (of order Ω) is non-zero, which makes for a stronger effect of bulk viscous processes on the damping of these modes. For accreting neutron stars (see Chapter 5), bulk viscosity is more important than shear viscosity in determining persistent gravitational wave emission. The expression for the timescale associated with the damping of r-modes due to bulk viscosity is calculated in Sec. 5.3.2.

4.2 Viscous processes of neutron stars

The interiors of neutron stars are rich dense environments where various strong, weak, and electromagnetic interactions take place. These interactions tend to damp the gravitational radiation driven oscillations of neutron stars. These processes can be roughly divided up into two categories: processes that cause shear viscosity and those that cause bulk viscosity.

[2] The highest allowed frequency of a neutron star before it starts to disintegrate. Physically, it represents the frequency at which the centrifugal force on a point particle at the equator balances the gravitational force experienced by it.

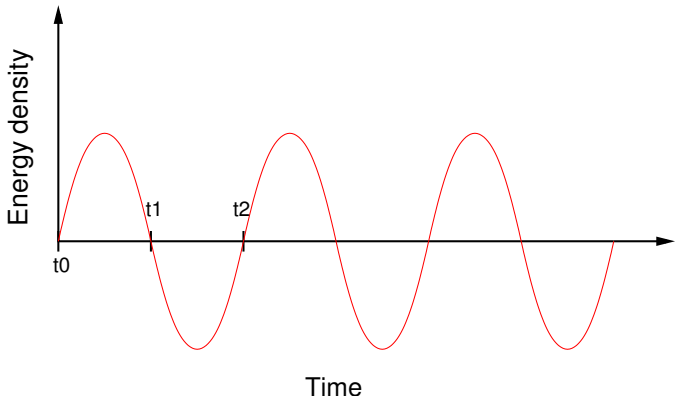

Figure 4.1: A sinusoidal perturbation of the energy density of a neutron star fluid element as a function of time.

The chief contributor to shear viscosity in stars which do not exhibit superfluidity is the neutron-neutron scattering process [80]. The T^{-2} dependence on temperature implies that the viscosity from this process dominates at low neutron star temperatures. Real neutron stars are likely to be superfluid as suggested by temperature-age measurements and cooling curve calculations [81]. In these stars the dominant shear viscosity process is a superfluid effect called mutual friction that results from the scattering of electrons off the magnetic fields in the cores of vortices [82]. Other shear viscous processes that might be present share a similar inversely proportional dependence on temperature which causes an increase in damping at lower temperatures. The shear viscous processes determine the low temperature part of the critical frequency curve (see Fig. 5.1).

Bulk viscous processes convert the mechanical energy of the oscillation modes of the star to heat. They occur in any multi-component system which is perturbed away from mechanical equilibrium. This, in turn, causes the system to also move away from chemical equilibrium. Chemical reactions then try to bring the system back to chemical equilibrium which causes the mechanical energy associated with the oscillation to be converted to heat. For a more detailed explanation, consider a fluid element that undergoes a sinusoidal perturbation as depicted in Fig. 4.1. When the fluid element is compressed, as in the time interval $t_0 - t_1$, interaction processes work to decrease its pressure towards chemical equilibrium. Similarly, in the interval $t_1 - t_2$, they work to increase its pressure. In real stars, this process is not instantaneous, chemical reactions take a finite time to bring about chemical equilibrium. Since the mechanical perturbation varies with time, the finite timescale of this equilibrium restoring process implies that the pressure of the fluid element always lags the chemical equilibrium pressure value. It also implies that irreversible processes continually try reaching chemical equilibrium that is never reached. The irreversible processes cause the mechanical energy of the oscillation to be converted to heat. A representative fluid

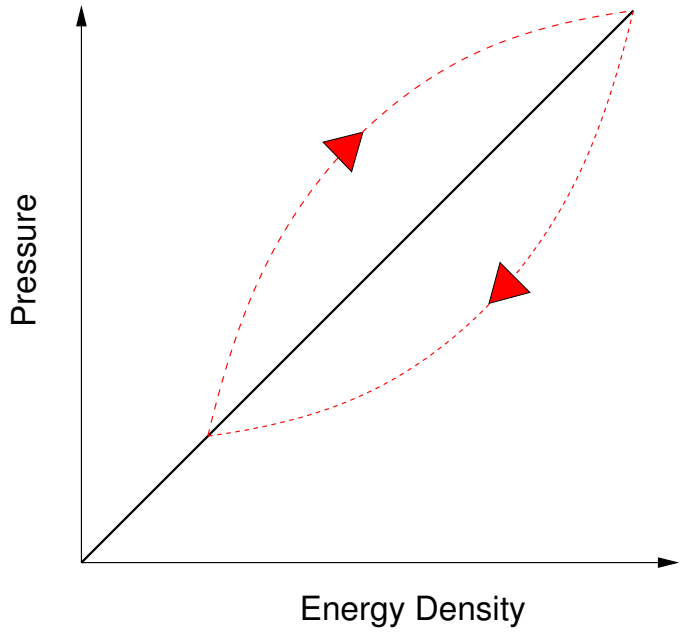

Figure 4.2: Companion figure to Fig. 4.1: The dashed line denotes the deviation of the fluid element from chemical equilibrium, represented by the solid equation of state line, in the course of one oscillation (t_0–t_2).

element executes a loop in the density–pressure plane as depicted in Fig. 4.2 over the time period of an oscillation (t_0 to t_2 of Fig. 4.1). The part of the loop above the solid line (the equation of state representing chemical equilibrium) corresponds to the interval $t_0 - t_1$ of Fig. 4.1 where the fluid element is compressed. In this region the finite rates of the bulk viscous processes imply a value of pressure which is higher than the equation of state value (which assumes infinite time to relax to chemical equilibrium). For a hyperon star, since the presence of hyperons usually reduces pressure on account of their higher masses as compared to nucleons, the limited rate implies a surplus of nucleons that have not been converted to hyperons by the reactions yet. The region below the solid line corresponds to the interval $t_1 - t_2$ of Fig. 4.1. Here the fluid element is rarefied. The finite reaction rate in this region results in a surplus of hyperons which implies a value of pressure which is too low. Fig. 4.2 can be mapped to a figure that plots pressure versus the volume. The loop of Fig. 4.2 will map to a corresponding loop in the pressure-volume plane. The area inside the pressure-volume plane loop represents the amount of work done on the fluid element in the course of one mechanical oscillation, i.e. the amount of mechanical energy pumped out of the oscillation mode. Bulk viscous processes are most effective when the timescales of the relevant reactions are comparable to the oscillation period of the mode. For r-mode oscillations, our interest is in the weak interactions as they have relaxation timescales which

are within a few orders of magnitude of the millisecond periods of the oscillations.

In non-superfluid neutron stars, with no exotic matter content, the main bulk viscous processes are the direct Urca[3] and modified Urca reactions of the nucleons. The direct Urca reactions are essentially the β-decay and reverse-β-decay of the neutron:

$$\begin{aligned} n &\leftrightarrow p^+ + l + \bar{\nu}_l, \\ p^+ + l &\leftrightarrow n + \nu_l. \end{aligned} \tag{4.21}$$

Here, l denotes a lepton which could be either an electron or a muon, and ν_l, and $\bar{\nu}_l$, are, respectively, the corresponding neutrino and the antineutrino. Since the neutrinos and antineutrinos escape from the neutron star carrying away energy, these processes are also major contributors to neutron star cooling. The presence of direct Urca reactions, however, requires that the proton fraction of the star be greater than $\sim 1/9$, a stringent condition that is either never achieved for many equations of state, or achieved only for very heavy neutron stars. The physical origin of the requirement is that, in a neutron star, the Fermi energy, and hence the Fermi momenta, of the neutrons is much larger than the Fermi energy of the protons, which makes it difficult for the energy and momentum to be conserved for these processes. The modified Urca reactions do not suffer from this drawback. The nucleon on either side of Eq. (4.21) is accompanied by another nucleon which makes energy and momentum conservation possible irrespective of the equation of state and mass of the star. Superfluidity has the effect of decreasing the rates of these reactions, which in low-temperature stars results in decreased viscosity, but can increase viscosity in high-temperature stars (limit of Eq. (4.23) when $\omega\tau << 1$)

In stars with exotic matter content there are additional processes that contribute to bulk viscosity. In the interiors of neutron stars, where the densities can be higher than 2–3 times the nuclear density, it is reasonable to expect that the baryonic content is more varied than merely neutrons and protons. The many possibilities for these exotic states of matter include hyperons, quarks, and the K and π meson condensates. We conduct our investigations in Chapter 5 for hyperons, a choice dictated by the fact that we have much more experimental data for them than for the other exotic particle choices (although bulk viscosity calculations have been made recently for the other exotic matter choices [83, 84, 85]). Hyperons come with their own versions of the direct and modified Urca reactions. In the context of studying the persistent gravitational wave emission scenario in accreting hyperonic stars, the effect of both direct and modified Urca reactions is negligible. Modified Urca reactions are irrelevant as they dominate at temperatures higher than the LMXB temperature range. The contribution of direct Urca reactions is not significant compared

[3]Allegedly, named by George Gamow after a casino in Rio de Janeiro. Analogous to how the casino was a famous money sink, these processes, if occuring in a neutron star, would cause it to rapidly lose heat!

to another set of reactions involving hyperons: non-leptonic weak interactions. It is the latter reactions that determine the positive-sloped part of the instability curve where the movement of the neutron star could be arrested (see the Fig. 5.1 and the introduction to Chapter 5). See Sec. 5.2.2 for more details about the non-leptonic weak interactions we consider.

Subsequent to the publishing of our paper a few papers [86, 87] have calculated the instability curves for non-superfluid quark hybrid stars. The results indicate much higher damping from bulk viscosity than our results for hyperonic neutron stars. The implication is that the gravitational radiation explanation (see Introduction to Chapter 5) for the observed spin frequencies of neutron stars in LMXBs would not work for hybrid stars. Glampedakis and Andersson [88] have made a more sophisticated calculation of the crust-core low temperature vsicosity in neutron stars (the low-temperature negatively sloped part of the instability curve of Fig. 5.1). They have determined that for certain cases the associated damping rate shows about a two-fold decrease. Chatterjee and Bandyopadhyay [89] have calculated the bulk viscosity for kaon condensate matter and found that it is many orders of magnitude smaller than the results for hyperonic stars.

4.2.1 Bulk viscosity expression derivation

To calculate the timescale associated with the damping of the r-modes (see Eq. (5.55) in Sec. 5.3.2) by bulk viscosity we need to determine the macroscopic coefficient of bulk viscosity, ζ. We use for ζ the special relativistic expression derived by Lindblom and Owen [56]:

$$\zeta = \frac{p(\gamma_\infty - \gamma_0)\tau}{1 + (\hat{\omega}\tau)^2}, \tag{4.22}$$

where p is the pressure, $\hat{\omega}$ is the angular frequency of the r-mode in a frame corotating with the star, and τ is the net microscopic relaxation time associated with, in our case, the non-leptonic weak interactions.

Older derivations of the coefficient of bulk viscosity cannot be used for the calculation in neutron star matter. For relativistic systems where multiple inter-dependent interactions are jointly responsible for the bulk viscosity, Eq. (4.22) is more accurate than other derivations found in older literature [90, 91]. The older derivations, for instance the one by Landau and Lifshitz [90], are valid only when the associated particles have non-relativistic energies. In neutron stars this is clearly not the case—some particles have Fermi energies comparable to their masses. Another problem with Landau's result is that it cannot be used for the case where a set of non-independent microscopic processes are collectively responsible for the bulk viscosity. He does generalize his result so that it is applicable to the case where there are multiple processes responsible for bulk viscosity, but only if they are all independent of each other. For the case we are interested in, the two reactions (see Sec. 5.3.2) we consider

are related to each other through constraints like baryon number conservation and charge neutrality, so that Landau and Lifshitz's generalized result for independent processes is not applicable.

We now proceed to write the derivation of ζ by Lindblom and Owen [56], which does not suffer from the limitations of other derivations. The coefficient of bulk viscosity is the constant of proportionality relating the microscopic expansion $\vec{\nabla} \cdot \vec{v}$, to the quantity $p - \tilde{p}$, which is the difference between the pressure of the system, p, at a give time and the pressure at which the system would be in chemical equilibrium. The relationship is given by

$$p - \tilde{p} = -\zeta \vec{\nabla} \cdot \vec{v}, \tag{4.23}$$

where $\vec{v}$ is the velocity of the fluid element. The difference in the pressures reflects how bulk viscosity takes place when a system is out of equilibrium and is trying to attain it, while the non-zero microscopic expansion shows that bulk viscosity occurs only for compressible fluids. The thermodynamic pressure is derived from the equation of state and depends only on the baryon number density and entropy density. For cold neutron stars the temperature of the star is much smaller than the typical Fermi energy of the particles, so that the entropy of the system is small and the dependence of the equation of state on it can be ignored. We should think of the state of the displaced fluid element as a perturbation about a time independent equilibrium state. Quantities associated with this equilibrium state have the subscript "$_0$" while those associated with thermodynamic equilibrium have a "$\sim$" superscript. To obtain ζ in terms of the microscopic reaction rate we start off by expressing both sides of Eq. (4.23) in terms of $\Delta n \equiv n - n_0$, the Lagrangian baryon number density perturbation which is more convenient for relativistic calculations than the energy density. We assume that the perturbation has the time dependence $e^{-i\hat{\omega}t}$ in the comoving frame. We perturb the particle conservation equation about equilibrium and retain only the linear terms to re-express the right side of eq. (4.23) as

$$-\zeta \vec{\nabla} \cdot \delta\vec{v} = -i\hat{\omega}\zeta \Delta n/n, \tag{4.24}$$

where $\delta\vec{v}$ is the Eulerian velocity perturbation.

Now, consider x to be the independent variable that characterizes the microscopic reactions that cause bulk viscosity. We choose $x = x_n$, the number fraction of neutrons, for our calculation of hyperon bulk viscosity, since neutrons are involved in both the non-leptonic weak interactions we consider (see Sec. 5.3.2). In the comoving frame for small departures from equilibrium x moves toward its thermodynamic equilibrium value:

$$\partial_t x + \vec{v} \cdot \vec{\nabla} x = -(x - \tilde{x})/\tau, \tag{4.25}$$

where τ is the relaxation timescale for this process. Additionally, we should expect x and $\tilde{x}$ to oscillate about the background equilibrium, so that

$$(\partial_t + \vec{v}\cdot\vec{\nabla})(x - x_0) = -i\hat{\omega}(x - x_0), \tag{4.26}$$

$$(\partial_t + \vec{v}\cdot\vec{\nabla})(\tilde{x} - x_0) = -i\hat{\omega}(\tilde{x} - x_0). \tag{4.27}$$

It is easy to see from Eq. (4.25), Eq. (4.26), and the continuity equation,

$$\frac{\partial n}{\partial t} + \vec{\nabla}\cdot(n\vec{v}) = 0, \tag{4.28}$$

that holds for x_0, that the following is true:

$$x - x_0 = \frac{x - \tilde{x}}{i\hat{\omega}\tau} = \frac{\tilde{x} - x_0}{1 - i\hat{\omega}\tau}. \tag{4.29}$$

As the fluid element moves from the mechanical equilibrium state to the thermodynamic equilibrium state the corresponding change in the variable $\tilde{x}$ is given by

$$\tilde{x} - x_0 = \frac{d\tilde{x}}{dn}(\tilde{n} - n_0) = \frac{d\tilde{x}}{dn}\Delta n, \tag{4.30}$$

where we have used that, by definition, $n = \tilde{n}$, since baryon number is conserved. The pressure out of equilibrium can be expressed as a function of the number density n and x. We therefore obtain

$$\tilde{p} - p_0 = \left[\left(\frac{\partial p}{\partial n}\right)_x + \left(\frac{\partial p}{\partial x}\right)_n \frac{d\tilde{x}}{dn}\right]\Delta n. \tag{4.31}$$

Similarly, we obtain an expression for $p - p_0$,

$$p - p_0 = \left[\left(\frac{\partial p}{\partial n}\right)_x + \frac{1}{1 - i\hat{\omega}\tau}\left(\frac{\partial p}{\partial x}\right)_n \frac{d\tilde{x}}{dn}\right]\Delta n, \tag{4.32}$$

where we have used Eq. (4.29) to relate $x - x_0$ and $\tilde{x} - x_0$.

Combining Eqs. (4.31) and (4.32) gives us an expression for the difference in the pressure $p - \tilde{p}$ that appears on the left side of Eq. (4.23):

$$p - \tilde{p} = \frac{i\hat{\omega}\tau}{1 - i\hat{\omega}\tau}\left(\frac{\partial p}{\partial x}\right)_n \frac{d\tilde{x}}{dn}\Delta n. \tag{4.33}$$

Then equating this expression for the left side of Eq. (4.23) with the expression for the right side from Eq. (4.24), we find the desired formula for the bulk viscosity:

$$\zeta = \frac{-n\tau}{1 - i\hat{\omega}\tau}\left(\frac{\partial p}{\partial x}\right)_n \frac{d\tilde{x}}{dn}. \tag{4.34}$$

Finally, it is convenient to re-express the thermodynamic derivatives that appear in Eq. (4.22) in terms of

$$\gamma_\infty = \frac{n}{p}\left(\frac{\partial p}{\partial n}\right)_x , \tag{4.35}$$

the "infinite" frequency adiabatic index, and

$$\gamma_0 = \frac{n}{p}\left[\left(\frac{\partial p}{\partial n}\right)_x + \left(\frac{\partial p}{\partial x}\right)_n \frac{d\tilde{x}}{dn}\right], \tag{4.36}$$

the "zero" frequency adiabatic index. Using Eq. (4.35) and Eq. (4.36) we obtain the desired expression, Eq. (4.22), for the coefficient of bulk viscosity. This expression agrees with the non-relativistic result when we write the γ's in terms of corresponding u's, the speeds of sound, using the relationship $p\gamma = \rho u^2$:

$$\zeta = \frac{\rho(c_\infty^2 - c_0^2)\tau}{1 - i\tilde{\omega}\tau}. \tag{4.37}$$

In a neutron star one would expect the energies of the constituting particles to be relativistic even though the bulk motion associated with the fluid itself is non-relativistic, so that we should use the relativistic expression for ζ.

Now we illustrate how the net timescale is determined when the underlying bulk viscous processes are not independent. When the processes are independent the the net timescale can be found using

$$\frac{1}{\tau} = \sum_i^n \frac{1}{\tau_i}, \tag{4.38}$$

where τ_i are the timescales associated with each independent process. To calculate the relaxation timescale when the processes are not independent we first need to calculate the reaction rates for the non-leptonic weak interactions. To relate the two we notice that any change in x_n depends on internal reactions and not on any changes in the volume, so that we may write

$$(\delta_t + \vec{v}\cdot\vec{\nabla})x_n = -\frac{(x_n - \tilde{x_n})}{\tau} = -\frac{\Gamma_n}{n_B}. \tag{4.39}$$

Here n_B is the baryon number density and Γ_n is the net reaction rate at which neutrons are produced. We can rearrange the terms in the above equation to obtain

$$\frac{1}{\tau} = \frac{\Gamma_n}{\delta x_n n_B}. \tag{4.40}$$

4.3 Relaxation timescales

4.3.1 Collision integrals

In this section we calculate the reaction rates (Γ_n in Eq. (4.40)) and the net relaxation timescales (Eq. (5.15) and Eq. (5.16)) associated with the weak interactions responsible for bulk viscosity. We reproduce in more detail the calculation from Lindblom and Owen [56] who use the standard techniques of time-dependent perturbation theory in relativistic quantum mechanics. The result is valid for the case when superfluidity is completely absent.

For a single reaction involving two incoming and two outgoing particles the differential reaction rate is

$$d\Gamma = |\mathcal{M}|^2 (2\pi)^4 \delta^{(4)}(p_1 + p_2 - p_3 - p_4) S \prod_{i=1}^{4} \frac{d^3\boldsymbol{p}_i}{(2\pi)^3 2\epsilon_i}, \tag{4.41}$$

where p_i is the momentum of the ith particle, $|\mathcal{M}|^2$ is the spinor matrix element (squared and summed over spin states), $\boldsymbol{p}_i$ are 3-momenta, ϵ_i are particle energies, and we have set $\hbar = 1$. The statistical factor S, which compensates for overcounting momentum states of indistinguishable particles, is 1/2 for reaction involving the Σ^- hyperon, Eq. (5.12), and 1 for the Λ hyperon reaction, Eq. (5.13).

To obtain the total reaction rate we integrate the differential reaction rate, Eq. (4.41), over the momenta of the particles:

$$\begin{aligned} \Gamma \;\; = \;\; & \frac{S}{4096\pi^8} \int \prod_{i=1}^{4} \frac{d^3\boldsymbol{p}_i}{\epsilon_i} |\mathcal{M}|^2 \delta^{(3)}(\boldsymbol{p}_1 + \boldsymbol{p}_2 - \boldsymbol{p}_3 - \boldsymbol{p}_4) \\ & \times F(\epsilon_i) \delta(\epsilon_1 + \epsilon_2 - \epsilon_3 - \epsilon_4). \end{aligned} \tag{4.42}$$

Here, $p_i = \sqrt{\boldsymbol{p}_i \cdot \boldsymbol{p}_i}$ denotes the absolute value of the 3–momenta. The Pauli blocking factor $F(\epsilon_i)$ in Eq. (4.42) is

$$F(\epsilon_i) = f_1 f_2 (1 - f_3)(1 - f_4) - (1 - f_1)(1 - f_2) f_3 f_4, \tag{4.43}$$

where,

$$f_i = 1/\{1 + \exp[(\epsilon_i - \mu_i)/kT]\}, \tag{4.44}$$

reflects the degeneracy of the particles participating in the reactions.

In the case where the particles are degenerate the integral can be split up into a part that depends only on the energies of the particles and another that contains all the angular dependence. The separation requires simplification of the part of the integrand that contains the delta function, the energies of the particles in the denominator, and the differential

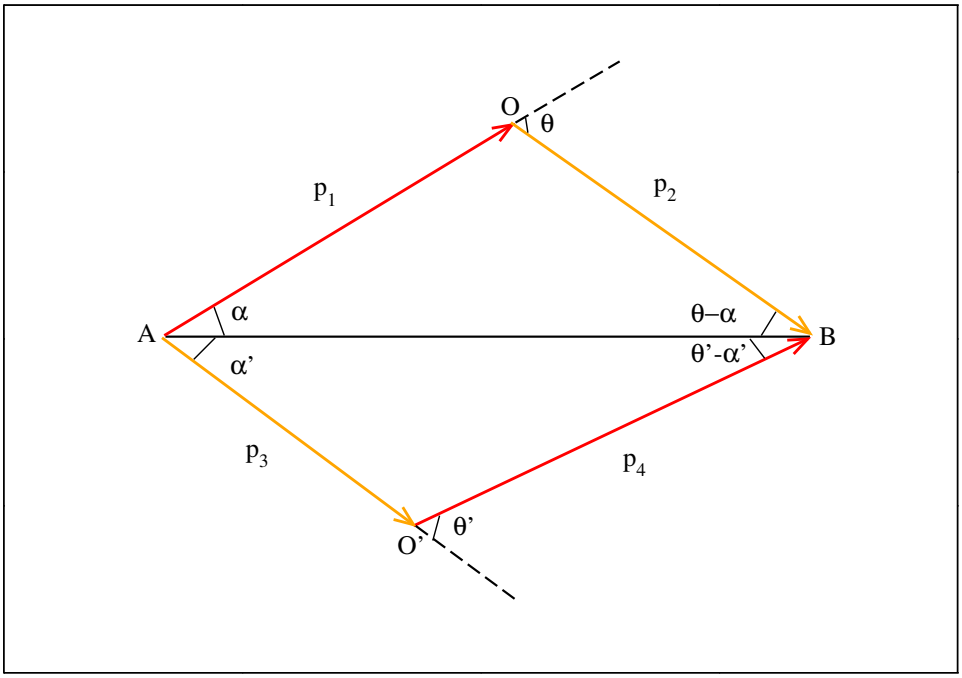

Figure 4.3: Diagram expressing the relationships between the momenta of the particles involved in a reaction. The triangle AOB and AO'B are not in the same plane.

elements of the momenta, the variables over which the integral is to be integrated:

$$\delta^{(3)}(\boldsymbol{p}_1 + \boldsymbol{p}_2 - \boldsymbol{p}_3 - \boldsymbol{p}_4) \prod_{i=1}^{4} \frac{d^3\boldsymbol{p}_i}{\epsilon_i}. \tag{4.45}$$

We use Fig. 4.3 to explain how this is done. The $\boldsymbol{p}_1$ volume element can be written as $4\pi {p_1}^2 dp_1$ as there is no preferred direction, while the $\boldsymbol{p}_2$ volume element is written as $p_2^2 dp_2 \sin\theta d\theta d\phi$, where θ and ϕ are the polar and azimuthal angles with respect to $\vec{p}_1$. Conservation of momentum, represented by the delta function in Eq. (4.45) demands that $\boldsymbol{p}_1 + \boldsymbol{p}_2 = \boldsymbol{p}_3 + \boldsymbol{p}_4$, determining a common axis which is indicated as the segment AB in the figure. Let α and α' be the angles $\boldsymbol{p}_1$ and $\boldsymbol{p}_3$ make with that axis, respectively. The volume element of $\boldsymbol{p}_3$ is given by $p_3 \sin\alpha' d\phi'$ times the area element in the plane that contains $\boldsymbol{p}_3$ and $\boldsymbol{p}_4$. The angle ϕ' is the angle between $\boldsymbol{p}_1 \times \boldsymbol{p}_2$ and $\boldsymbol{p}_3 \times \boldsymbol{p}_4$. To separate the energetic and angular integrals, it is convenient to write this area element as $dp_3 dp_4 / \sin\theta'$, where θ' is the angle between $\boldsymbol{p}_3$ and $\boldsymbol{p}_4$. We can now write Eq. (4.45) as

$$\frac{4\pi p_1^2 p_2^2 p_3 \sin\alpha'}{\sin\theta'} d\theta d\phi d\phi' \prod_{1=1}^{4} dp_i \tag{4.46}$$

This expression can be further simplified by differentiating the following equation keeping the p_i constant:

$$p_1^2 + p_2^2 + 2p_1p_2\cos\theta = p_3^2 + p_4^2 + 2p_3p_4\cos\theta', \tag{4.47}$$

and using the relationship between ϵ_i and p_i for relativistic particles

$$p_i dp_i = \epsilon_i d\epsilon_i, \tag{4.48}$$

to obtain

$$\delta^{(3)}(\boldsymbol{p}_1 + \boldsymbol{p}_2 - \boldsymbol{p}_3 - \boldsymbol{p}_4)\prod_{i=1}^{4}\frac{d^3\boldsymbol{p}_i}{\epsilon_i} = 4\pi p_3 \sin\alpha' d\theta' d\phi' d\phi \prod_{i=1}^{4} d\epsilon_i. \tag{4.49}$$

Although the limits of ϕ and ϕ' cover the entire angular range from 0 to 2π, the limits of integration for θ' depend on the relations between the momenta p_i, which are constrained to be close to the Fermi momenta (henceforth, p_i refers to the Fermi momenta). The angle θ' can be integrated over the full range, 0 to π, allowed by momentum conservation, when the following conditions are satisfied:

$$\begin{aligned} p_1 + p_2 &\geq p_3 + p_4 \\ p_1 - p_2 &\leq p_3 + p_4 \\ p_1 - p_2 &\leq p_3 - p_4 \\ p_1 + p_2 &\geq p_3 - p_4 \end{aligned} \tag{4.50}$$

where p_4 refers either to the Σ^- or the Λ hyperon depending on the reaction. These conditions can be written down in a more compact form as:

$$p_n \geq p_p \geq (p_\Lambda, p_\Sigma). \tag{4.51}$$

In realistic neutron stars one would expect that for densities upto $\rho \sim 1.0 \times 10^{15}\mathrm{g/cm}^3$, the hyperons would have lower momenta than the nucleons, and therefore the identity in Eq. (4.51) would be satisfied. At higher densities this identity might be violated, but there the very description of baryons as discernibly independent entities is likely to be invalid, thereby making the entire approach of calculating collision integrals of baryons meaningless.

To obtain the final expression for the part of the integral that depends only on the angles we make use of the angle-averaged value of $|\mathcal{M}|^2$ which we calculate later in this section. We can now integrate over the remaining angle θ' by using the fact that $p_3 > p_4$ and that

in Fig. 4.3

$$p_3 \sin\alpha' = p_4 \sin(\theta' - \alpha') \tag{4.52}$$

to obtain

$$\int_0^\pi p_3 \sin\alpha' d\theta' = 2p_4. \tag{4.53}$$

Having solved its angle-dependent part we obtain the following simplified form for the collision integral:

$$\Gamma = \frac{S}{128\pi^5} \int \prod_{i=1}^{4} d\epsilon_i p_4 \langle|\mathcal{M}|^2\rangle F(\epsilon_i) \delta(\epsilon_1 + \epsilon_2 - \epsilon_3 - \epsilon_4) \tag{4.54}$$

To evaluate the part of the integral that depends on the energy,

$$\mathcal{I} = \int \prod_i d\epsilon_i F(\epsilon_i) \delta(\epsilon_1 + \epsilon_2 - \epsilon_3 - \epsilon_4), \tag{4.55}$$

we replace the energies of the particles with the variables x_i which are defined as

$$x_i = \frac{\epsilon_i - \mu_i}{kT}, \tag{4.56}$$

where μ_i are the Fermi energies of the particles, and set

$$\frac{\delta\mu}{kT} \equiv \frac{\mu_1 + \mu_2 - \mu_3 - \mu_4}{kT} = \Delta. \tag{4.57}$$

We now obtain obtain for $\mathcal{I}$

$$\mathcal{I} = (kT)^3 \int_{-\infty}^{\infty} \prod_i \frac{dx_i}{(1 + e^{x_i})} e^{x_3 + x_4} (1 - e^{x_1 + x_2 - x_3 - x_4}) \delta(x_1 + x_2 - x_3 - x_4 + \Delta), \tag{4.58}$$

where we have used Eq. (4.56) and Eq. (4.57) along with the property of $\delta(x)$ that

$$\int_{-\infty}^{\infty} \delta(x) dx = \frac{1}{a} \int_{-\infty}^{\infty} \delta\left(\frac{y}{a}\right) dy, \tag{4.59}$$

which is valid for any finite value of an arbitrary constant a, and the condition

$$\frac{|\epsilon(0) - \mu_i|}{kT} \gg 1, \tag{4.60}$$

which is true for degenerate systems. Condition Eq. (4.60) allows us to set the lower limit for the integral in Eq. (4.58) to $-\infty$, which makes its evaluation possible. This approximation is however not valid for a small region of density that lies immediately above the threshold density for the appearance of hyperons. This is due to the fact that in this regime the

hyperons, since they have very low momenta, are very close to the Fermi surface. We expect the values of ζ at the hyperon thresholds and at slightly higher densities to be off by a few percent.

Now we use the following substitutions to further simplify the integrand

$$\begin{aligned} y_1 &= x_1 + x_2 \\ y_2 &= x_1 - x_2 \\ y_3 &= x_3 + x_4 \\ y_4 &= x_3 - x_4, \end{aligned} \tag{4.61}$$

which can be written as

$$\mathcal{I} = \frac{1}{4}(kT)^3 \int_{-\infty}^{\infty} \prod_i dy_i \frac{e^{y_3}(1-e^{y_1-y_3})\delta(y_1-y_3+\Delta)}{(1+e^{(y_1+y_2)/2})(1-e^{(y_1-y_2)/2})(1+e^{(y_3+y_4)/2})(1-e^{(y_3-y_4)/2})} \tag{4.62}$$

$$= \frac{1}{4}(kT)^3 \int_{-\infty}^{\infty} \mathcal{I}_2 \mathcal{I}_4 e^{y_3}(1-e^{y_1-y_3})\delta(y_1-y_3+\Delta)dy_1 dy_3, \tag{4.63}$$

where,

$$\mathcal{I}_2 = \int_{-\infty}^{\infty} \frac{dy_2 e^{y_2/2}}{(1+e^{(y_1+y_2)/2})(e^{y_1/2}+e^{y_2/2})}, \tag{4.64}$$

$$\mathcal{I}_4 = \int_{-\infty}^{\infty} \frac{dy_4 e^{y_4/2}}{(1+e^{(y_3+y_4)/2})(e^{y_3/2}+e^{y_4/2})}. \tag{4.65}$$

The integrals $\mathcal{I}_2$ and $\mathcal{I}_4$ are of identical form,

$$\mathcal{I}_2 = \frac{2y_1}{e^{y_1}-1}, \tag{4.66}$$

$$\mathcal{I}_4 = \frac{2y_3}{e^{y_3}-1}, \tag{4.67}$$

and can be solved analytically. The expression for $\mathcal{I}$ in Eq. (4.63) can now be written as

$$\mathcal{I} = (kT)^3 \int_{-\infty}^{\infty} \frac{y_1 y_3 e^{y_3}(1-e^{y_1-y_3})\delta(y_1-y_3+\Delta)dy_1 dy_3}{(e^{y_1}-1)(e^{y_3}-1)} \tag{4.68}$$

which in the limit of small perturbations, $\Delta \equiv \delta\mu/kT \ll 1$, reduces to

$$\mathcal{I} = (kT)^2 \delta\mu \int_{-\infty}^{\infty} \frac{y^2 dy}{(1-e^{-y})(e^y-1)} \tag{4.69}$$

The integral in Eq. (4.69) is solved as follows: we first notice that the integrand is an even integrand so that we may transform the integrand to twice its value and change the

lower limit of the integral to zero. We then proceed to integrate it by parts:

$$\int_{-\infty}^{\infty} \frac{y^2 dy}{(1-e^{-y})(e^y-1)} = 2\left[\frac{-y^2}{e^y-1}\right]_0^{\infty} + 4\int_0^{\infty} \frac{y dy}{e^y-1}. \tag{4.70}$$

The first term in the integral is zero: when $y \to \infty$ the denominator goes to infinity faster than the numerator, whereas to find the limit $y \to 0$ one can expand out e^y as $1 + y + \frac{y^2}{2!} + \frac{y^3}{3!}\ldots$, and then obtain a finite limit of zero obtained by setting $y = 0$. The remaining integral can be evaluated as in appendix A-11 of Reif [92]. We start by expressing the integrand as a series:

$$\frac{y}{e^y-1} = \frac{ye^{-y}}{1-e^{-y}} = ye^{-y}[1 + e^{-y} + e^{-2y} + e^{-3y}\ldots] = \sum_{n=1}^{\infty} ye^{-ny}. \tag{4.71}$$

The integral in Eq. (4.70) can first be rewritten as

$$\sum_{n=1}^{\infty} \int_0^{\infty} 4ye^{-ny} dy, \tag{4.72}$$

and then, using the fact that the sum of the infinite series is $\pi^2/6$, as

$$4\sum_{0}^{\infty} \frac{1}{n^2} = \frac{2\pi^2}{3}. \tag{4.73}$$

We, finally, obtain for $\mathcal{I}$

$$\mathcal{I} = \frac{2\pi^2 (kT)^2 \delta\mu}{3}, \tag{4.74}$$

and for Γ by substituting Eq. (4.74) into Eq. (4.58) the expression

$$\Gamma = \frac{S}{192\pi^3} \langle |\mathcal{M}|^2 \rangle p_4 (kT)^2 \delta\mu. \tag{4.75}$$

4.3.2 Matrix elements of non-leptonic weak interactions

Now we calculate the angle-averaged values of the matrix elements (Eq. (5.17) and Eq.(5.18)). We use the convention of Griffiths [93]: spinors are normalized as $\bar{u}u = 2m$ and $\gamma^5 = i\gamma^0\gamma^1\gamma^2\gamma^3$; in addition, we set $\hbar = c = 1$. We first calculate $|\mathcal{M}|^2$ for the two hyperonic weak interactions we consider (Eq. (5.12) and Eq. (5.13)).

We begin by writing some of the important rules associated with solving Feynman diagrams for weak interaction processes. The propagator associated with the exchange of a W boson is given by

$$\frac{i g_{\mu\nu}}{M_W^2}, \tag{4.76}$$

where, M_W is the mass of the charged W boson, and $g_{\mu\nu}$ is the Minkowski metric with time component $+1$. The vertex factor for weak interactions for leptons is given by

$$\frac{-ig_w}{2\sqrt{2}}\gamma^\mu(1-\gamma^5), \tag{4.77}$$

where, g_w is the weak coupling constant. Our interest is in baryonic weak interactions, where the actual interaction occurs through the quarks that constitute the participating baryons. To accommodate quarks one has to make two modifications to the vertex factor: the first, associated with the transformation of one quark to another at the vertex, introduces a trigonometric factor, indicated by $f(\theta_C)$ in the equation below, of either $\cos\theta_C$ or $\sin\theta_C$ (in certain cases accompanied with a negative sign) depending on how probable that particular transformation is—since θ_C, which is the Cabbibo angle is small, the more favorable transformations are associated with $\cos\theta_C$, while the less favorable ones with $\sin\theta_C$; the second correction—a pre-factor before γ^5 (g_{AB} in the equation below) in the term within the parenthesis of Eq. (4.77)—arises from the intra-baryonic strong interaction of the participant quark with the two other quarks that form the baryon. Current techniques of QCD are not developed enough to calculate this correction, g_{AB}. Instead, it is inferred from low-density β-decay experimental data. The modified vertex factor is thus given by

$$\frac{-ig_w}{2\sqrt{2}}\gamma^\mu(1+g_{AB}\gamma^5)\times f(\theta_C). \tag{4.78}$$

We now use the Feynman rules to obtain the matrix element for a single set of spin states of the tree-level diagram, the top figure of Fig. 4.4, for the Λ reaction Eq. (5.13):

$$\begin{aligned}\mathcal{M}_\Lambda &= \frac{G_F}{2\sqrt{2}}\sin 2\theta_C\left[\bar{u}(p_3)\gamma^\mu\left(1+g_{np}\gamma^5\right)u(p_1)\bar{u}(p_4)\right.\\ &\left.\times\,\gamma_\mu\left(1+g_{p\Lambda}\gamma^5\right)u(p_2)\right].\end{aligned} \tag{4.79}$$

Here, the particles are labeled as follows: incoming neutron by 1, incoming proton by 2, outgoing proton by 3, and outgoing Λ by 4. The Fermi coupling constant G_F is defined as

$$G_F \equiv \frac{\sqrt{2}}{8}\left(\frac{g_W}{M_W}\right)^2. \tag{4.80}$$

The factor g_{np} arises from the left vertex in the top figure, where the subscript refers to the two particles associated with that vertex, the incoming neutron and the outgoing proton. Similarly, the factor $g_{p\Lambda}$ is associated with the incoming proton and the outgoing Λ at the right vertex. The bottom figure helps to explain the trigonometric factors. The left vertex contributes $\cos\theta_C$ corresponding to the transformation of a down quark to an up quark. This is a more favorable transformation than the up to strange quark transformation that

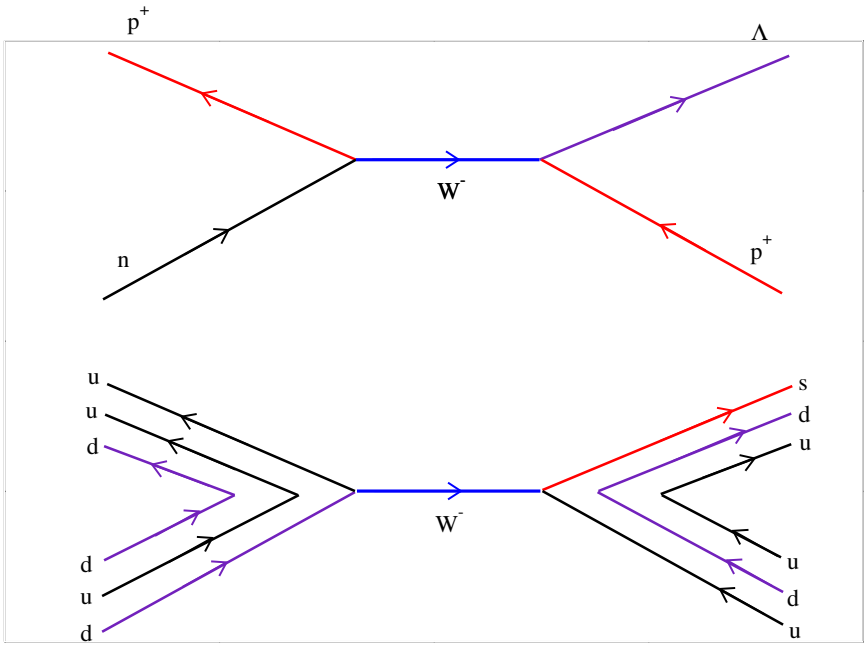

Figure 4.4: The top figure depicts the Λ reaction as a interaction between baryons. The bottom figure depicts the more fundamental underlying interaction—that of quarks which constitute the baryons. Notice how only one of the three quarks that make up a baryon participates in the reaction.

takes place at the right vertex, and which, therefore, contributes the smaller trigonometric factor $\sin\theta_C$.

We obtain $|\mathcal{M}|^2$ by using 'Casimir's trick', summing over all the final spin states, and averaging over the initial spin states:

$$\begin{aligned}
|\mathcal{M}_\Lambda|^2 &= 4G_F^2 \sin^2 2\theta_C \left\{ 2m_n m_p^2 m_\Lambda \left(1-g_{np}^2\right)\left(1-g_{p\Lambda}^2\right) \right. \\
&\quad -m_n m_p p_2\cdot p_4 \left(1-g_{np}^2\right)\left(1+g_{p\Lambda}^2\right) \\
&\quad -m_p m_\Lambda p_1\cdot p_3 \left(1+g_{np}^2\right)\left(1-g_{p\Lambda}^2\right) \\
&\quad +p_1\cdot p_2\, p_3\cdot p_4 \left[\left(1+g_{np}^2\right)\left(1+g_{p\Lambda}^2\right)+4g_{np}g_{p\Lambda}\right] \\
&\quad \left. +p_1\cdot p_4\, p_2\cdot p_3 \left[\left(1+g_{np}^2\right)\left(1+g_{p\Lambda}^2\right)-4g_{np}g_{p\Lambda}\right]\right\}.
\end{aligned} \tag{4.81}$$

Casimir's trick makes use of the fact that the spinor fields satisfy the Dirac equation. The Dirac equation is obtained from a Lagrangian that assumes no interactions between the particles. However, the Lagrangian we use for our equation of state has interaction terms (see Eq. (2.2) of Sec. 2.2), so that the Euler-Lagrange equation for the baryons in this case is a modified version of the Dirac equation. This modified version of the Dirac equation can be put in its more conventional form by defining:

$$K_B^\mu = p^\mu - g_{\omega B}\omega^\mu - g_{\rho B}\rho_3^\mu I_{3B}, \tag{4.82}$$

$$m_B^* = m_B - g_{\sigma B}\sigma, \tag{4.83}$$

to obtain the momentum space Dirac equation

$$(\gamma^\mu K_\mu - m^*)u(K) = 0, \tag{4.84}$$

where $K^0 = \sqrt{\boldsymbol{K}^2 + m*^2}$. Here p^μ is the four-momentum of the particle. Casimir's trick uses this form of the Dirac equation so that p^i and ϵ in this section, from this point on, refer to K^i and K^0, respectively ($K^i = p^i$, as the spatial components of ω^μ and ρ_3^μ are zero) [4].

Reaction Eq. (5.12) (shown in Fig. 4.5) is treated similarly, with particle labels 1 and 2 (neutrons), 3 (proton), and 4 (Σ^-). In this case another tree level diagram, corresponding to switching the neutrons, is possible. Antisymmetrizing, to take into account both diagrams,

[4] In the published paper we use the chemical potential for ϵ in the final expressions for $|\mathcal{M}|^2$ (see Eqs. (5.17) and (5.18)) instead of using $\sqrt{p^2+m*^2}$. Due to this the results for the coefficient of bulk viscosity quoted in the paper are ~ 10 times too small. This affects the instability curves only by a few percent which does not affect our conclusions.

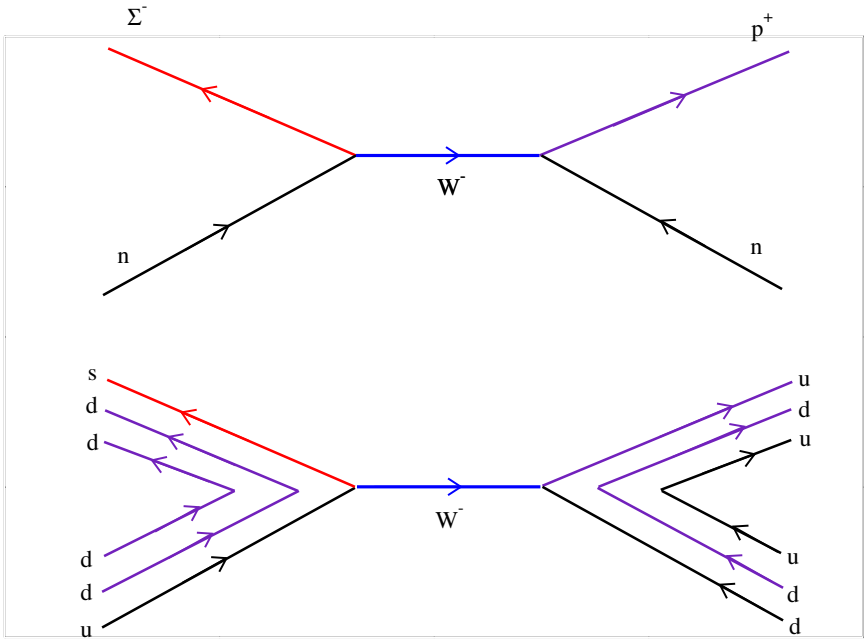

Figure 4.5: The top figure depicts the Σ^- reaction as a interaction between baryons. The bottom figure depicts the more fundamental underlying interaction—that of quarks that constitute the baryons. Notice how only one of the three quarks that make up a baryon participates in the reaction.

gives us the matrix element:

$$\begin{aligned}\mathcal{M}_\Sigma &= \frac{G_F}{2\sqrt{2}}\sin 2\theta_C \bar{u}(p_3)\gamma^\mu\left(1+g_{np}\gamma^5\right)[u(p_1)\bar{u}(p_4)\\ &\quad\times\gamma_\mu\left(1+g_{n\Sigma}\gamma^5\right)u(p_2) - u(p_2)\bar{u}(p_4)\gamma_\mu\left(1+g_{n\Sigma}\gamma^5\right)\\ &\quad u(p_1)]\,. \end{aligned} \tag{4.85}$$

Here too, the factor $\sin\theta_C$ is obtained from the vertex in the bottom figure of Fig. 4.5 where the up quark is transforming to a strange quark. The other vertex contributes the $\sin\theta_C$ factor. The factor $g_{n\Sigma}$ is obtained from the vertex of the top figure where the neutron is being transformed to a Σ^-. When the matrix element is squared, averaged over the initial states, and summed over the final states we obtain

$$\begin{aligned}|\mathcal{M}_\Sigma|^2 &= 4G_F^2\sin^2 2\theta_C\left\{6m_n^2 m_p m_\Sigma\left(1-g_{np}^2\right)\left(1-g_{n\Sigma}^2\right)\right.\\ &\quad -m_p m_\Sigma p_1\cdot p_2\left(1-g_{np}^2\right)\left(1-g_{n\Sigma}^2\right)\\ &\quad -2m_n m_\Sigma p_1\cdot p_3\left(1+g_{np}^2\right)\left(1-g_{n\Sigma}^2\right)\\ &\quad -2m_n m_p p_1\cdot p_4\left(1-g_{np}^2\right)\left(1+g_{n\Sigma}^2\right)\\ &\quad -2m_n m_\Sigma p_2\cdot p_3\left(1+g_{np}^2\right)\left(1-g_{n\Sigma}^2\right)\\ &\quad -2m_n m_p p_2\cdot p_4\left(1-g_{np}^2\right)\left(1+g_{n\Sigma}^2\right)\\ &\quad -m_n^2 p_3\cdot p_4\left[\left(1+g_{np}^2\right)\left(1+g_{n\Sigma}^2\right)-4g_{np}g_{n\Sigma}\right]\\ &\quad +4p_1\cdot p_2\, p_3\cdot p_4\left[\left(1+g_{np}^2\right)\left(1+g_{n\Sigma}^2\right)+4g_{np}g_{n\Sigma}\right]\\ &\quad +p_1\cdot p_3\, p_2\cdot p_4\left[\left(1+g_{np}^2\right)\left(1+g_{n\Sigma}^2\right)-4g_{np}g_{n\Sigma}\right]\\ &\quad \left.+p_1\cdot p_4\, p_2\cdot p_3\left[\left(1+g_{np}^2\right)\left(1+g_{n\Sigma}^2\right)-4g_{np}g_{n\Sigma}\right]\right\}. \end{aligned} \tag{4.86}$$

The angle averaged values of Eq. (4.81) and Eq. (4.86), which are needed to calculate the reaction rate Γ in Eq. (4.75) are obtained by using the following results:

$$\langle \boldsymbol{p}_1\cdot\boldsymbol{p}_2\rangle = \tfrac{1}{6}\left(-3p_1^2-3p_2^2+3p_3^2+p_4^2\right), \tag{4.87}$$

$$\langle \boldsymbol{p}_1\cdot\boldsymbol{p}_3\rangle = \tfrac{1}{6}\left(-3p_1^2+3p_2^2-3p_3^2+p_4^2\right), \tag{4.88}$$

$$\langle \boldsymbol{p}_1\cdot\boldsymbol{p}_4\rangle = \langle \boldsymbol{p}_2\cdot\boldsymbol{p}_4\rangle = \langle \boldsymbol{p}_3\cdot\boldsymbol{p}_4\rangle = -\tfrac{1}{3}p_4^2, \tag{4.89}$$

$$\langle \boldsymbol{p}_2\cdot\boldsymbol{p}_3\rangle = \tfrac{1}{6}\left(3p_1^2-3p_2^2-3p_3^2+p_4^2\right), \tag{4.90}$$

$$\langle \boldsymbol{p}_1\cdot\boldsymbol{p}_2\,\boldsymbol{p}_3\cdot\boldsymbol{p}_4\rangle = \tfrac{1}{30}p_4^2\left(5p_1^2+5p_2^2+5p_3^2-p_4^2\right), \tag{4.91}$$

$$\begin{aligned}\langle \boldsymbol{p}_1\cdot\boldsymbol{p}_3\,\boldsymbol{p}_2\cdot\boldsymbol{p}_4\rangle &= \langle \boldsymbol{p}_1\cdot\boldsymbol{p}_4\,\boldsymbol{p}_2\cdot\boldsymbol{p}_3\rangle \\ &= \frac{p_4^2}{60\left(p_3^2-p_4^2\right)}\left[5p_1^4-10p_1^2p_2^2+5p_2^2\right. \\ &\quad \left.+3\left(5p_3^4-6p_3^2p_4^2+p_4^4\right)\right]. \end{aligned} \tag{4.92}$$

Plugging the above angle averages into Eq. (4.81) and Eq. (4.86) we obtain our results, Eq. (5.17) and Eq. (5.18), respectively.

Once the reaction rates have been calculated we can now calculate the relaxation timescales that go in the expression for the ζ, the coefficient of bulk viscosity. The net timescale using the logic leading upto Eq. (4.40) is given by

$$\frac{1}{\tau} = \frac{\Gamma_\Lambda + 2\Gamma_\Sigma}{\delta\mu}\frac{\delta\mu}{n_B\delta x_n}. \tag{4.93}$$

Here Γ_Λ and Γ_Σ refer, respectively to the reactions in Eq. (5.13) and Eq. (5.12); the factor of 2 accompanying the latter arises due to the presence of *two* neutrons on the left hand side of reaction Eq. (5.12. In this equation we have introduced $\delta\mu$ in the numerator and the denominator. The one in the denominator cancels out the dependence of the reaction rates on $\delta\mu$, while the second factor in the above expression containing the $\delta\mu$ in the numerator is a thermodynamic derivative that we can evaluate. Substituting the result Eq. (4.75), and using the values 1, and 2, respectively, for S for the Λ and Σ^- reactions we obtain for the timescale when only Σ^- hyperons are present the result

$$\frac{1}{\tau} = \frac{(kT)^2}{192\pi^3}k_\Sigma\langle|\mathcal{M}_\Sigma^2|\rangle\frac{\delta\mu}{n\,x_n}, \tag{4.94}$$

and

$$\frac{1}{\tau} = \frac{(kT)^2}{192\pi^3}\left(k_\Sigma\langle|\mathcal{M}_\Sigma^2|\rangle + k_\Lambda\langle|\mathcal{M}_\Lambda^2|\rangle\right)\frac{\delta\mu}{n\,x_n} \tag{4.95}$$

when both Λ and Σ^- are present. Here kT is Boltzmann's constant times the temperature. The factor on the far right of Eqs. (4.94) and (4.95) is calculated like in Lindblom and Owen [56] as explained in Sec. 5.2.3.

Chapter 5

R-modes of accreting hyperon stars as persistent sources of gravitational waves

The r-modes of accreting neutron stars could be a detectable source of persistent gravitational waves if the bulk viscosity of the stellar matter can prevent a thermal runaway. This is possible if exotic particles such as hyperons are present in the core of the star. We compute bulk viscous damping rates and critical frequencies for r-modes of neutron stars containing hyperons in the framework of relativistic mean field theory. We combine the results of several previous calculations of the microphysics, include for the first time the effect of rotation, and explore the effects of various parameters on the viability of persistent gravitational wave emission. We find that persistent emission is quite robust, although it is disfavored in stars below 1.3–1.5 $M_\odot$ depending on the equation of state. In some cases persistent emission is compatible with temperatures as low as 10^7 K, observed in some accreting neutron stars in quiescence.

5.1 Introduction

The r-modes (fluid oscillations governed by the Coriolis force) of rapidly rotating neutron stars have attracted much interest as possible sources of gravitational waves and mechanisms for regulating the spins of neutron stars. See Ref. [72] for a recent review of the many physical and astrophysical issues related to the r-modes; here we focus on gravitational wave emission. Gravitational radiation drives the r-modes unstable and could lead to detectable gravitational wave emission in two scenarios. In one scenario, a newborn neutron star could radiate a substantial fraction of its rotational energy and angular momentum as gravitational waves changing in frequency on a timescale of a year or more [78]. In the other scenario, r-modes in rapidly accreting neutron stars in low-mass x-ray binaries (LMXBs) could be persistent sources of periodic gravitational waves [28, 36]. (Here the r-modes provide a specific mechanism for a more general torque balance argument [39, 94]).

Currently the latter scenario for gravitational wave emission (from LMXBs) looks like a brighter prospect for detection. There is now evidence from several approaches that the amplitude of an r-mode growing due to the instability is limited by nonlinear fluid dynamics

to a relatively small value [95, 96, 97, 98, 99, 100, 101]. While low-amplitude long-lived r-modes in newborn neutron stars still can lead to astrophysically interesting effects such as the regulation of spins, a low mode amplitude renders the gravitational wave signal undetectable unless there is a very nearby supernova [78]. Also, if neutron stars contain particles more exotic than neutrons and protons—such as hyperons, where an up or down quark in a nucleon is replaced by a strange quark—there are additional viscous damping mechanisms which may eliminate the instability altogether in very young, hot neutron stars [56, 57, 102, 103, 104, 105, 106, 107] or strange quark stars [108]. However, for the LMXB scenario, low amplitude is not a problem [28, 36] and the additional viscosity actually renders stars with exotic particles better candidates for gravitational wave detection. The reason for the latter is subtle, and bears explanation.

Real neutron stars are not perfect fluids, and thus viscous (and other) damping mechanisms compete with gravitational wave driving of the r-modes. The strengths of the driving and damping mechanisms can be expressed as timescales which depend on the rotation frequency and temperature of the star (usually assumed to be nearly isothermal). Therefore it is useful to consider the location of a star in the temperature-frequency plane, as shown in Fig. 5.1. The strength of viscosity can be graphically represented by a curve in that plane that is the locus of all points where the driving and damping timescales are equal—this defines a critical frequency as a function of temperature. Since the driving timescale decreases with frequency, stars above the critical frequency curve have one or more unstable r-modes, while stars below it are stable and stars on it are marginally stable.

Figure 5.1 plots examples of critical frequency curves in the temperature range 10^8 K$\ll T \ll 10^{10}$ K appropriate for the LMXB emission scenario. (The needed range is higher than most observed temperatures of LMXBs in quiescence because of a thermal runaway; see below.) At low temperatures the damping in Fig. 5.1 is taken to be dominated by shear viscosity in a boundary layer between the solid crust and fluid core (from Ref. [109], augmented by a constant relative crust-core velocity in the range discussed in Ref. [110]). There are many other possible curves for the low temperature part of the plot, corresponding to more complicated damping mechanisms such as turbulence [111] or superfluid magneto-viscous effects [112], but they generally share the qualitative property of decreasing with temperature. (Some low-temperature curves lie above the observed range of spins entirely, but the observed spins of low-mass x-ray binaries are easier to explain if the curve lies in the region indicated [28, 36, 113].) At high temperatures the damping is probably dominated by bulk viscosity, either from the Urca process (perturbation of β-equilibrium) or from non-leptonic processes involving strange particles such as hyperons. The Urca process, which requires no exotic particles, does not affect the critical frequency curve for $T < 10^{10}$ K and thus does not show up in Fig. 5.1. Thus the top plot in Fig. 5.1 shows a critical frequency curve for a neutron star, and the bottom plot shows such a curve for a star with hyperons

(with the high-temperature part of the curve derived from Ref. [56]). This type of plot looks encouraging for gravitational wave detection because there is plenty of room above the curve for stars to be unstable and thus emitting gravitational waves.

However, the gravitational wave emission duty cycle could be much smaller than 100% due to a thermal runaway [114, 115]. This happens generically when the critical frequency decreases with temperature. In that case, plotted at the top of Fig. 5.1, a star will execute a loop as shown and radiate only during the time it spends above the curve. A stable star which begins at the bottom left of the loop is spun up by accretion until it moves above the critical frequency and the instability is triggered. The shear from the growing r-modes then causes the star to heat up, moving it rightwards on the loop. As the temperature rises, so does the rate of neutrino cooling, causing the star to drop down toward the critical frequency again at a temperature of a few times 10^9 K. After falling below the critical frequency, the r-mode heating is removed and the star drifts leftward along the bottom of the loop until returning to its initial position. Although the time it takes for a star to complete the loop is dominated by the accretion rate, the timescale for gravitational wave emission depends mainly on the saturation amplitude of r-mode oscillations. For a saturation amplitude (α in the notation of Ref. [73]) of order unity, the duty cycle for gravitational wave emission is of the order 10^{-6} [114]. Whereas the duty cycle can be as high as about 30% for the lowest predicted values of the saturation amplitude ($\alpha \simeq 10^{-5}$), for typical estimates of the saturation amplitude ($\alpha \simeq 10^{-4}$) the duty cycle is only of order 10^{-1} [116]. Advanced LIGO will be able to detect at most one LMXB (Sco X-1) without narrowbanding (and hurting its ability to see other sources), or 6–7 LMXBs with narrowbanding around a series of different frequencies [15]. The small number of detectable systems and the fact that the timescale for a star to complete a loop is much longer than a human lifetime mean that a duty cycle of order 10^{-1} or less is pessimistic for gravitational wave searches for the r-modes.

If the critical frequency increases with temperature as in the bottom plot of Fig. 5.1, the thermal runaway can be blocked. A rapidly accreting star in an LMXB can have a duty cycle of order unity for emission of gravitational radiation as it sits on the curve or makes small peregrinations about it [117]. (It could also keep emitting, although less detectably, for some time after the rapid accretion shuts off [118].) This could happen for stars which exhibit a rise in the critical frequency curve at a low enough temperature. The rise is typical for stars where high bulk viscosity processes involving hyperons [58, 119] or strange quarks [120] are at work. Thus the case for the gravitational wave emission scenario is in fact strengthened by high bulk viscosity from processes which are fundamentally quark-quark interactions. One might expect similar critical frequency curves to arise for stars containing other forms of strange matter such as a kaon condensate or mixed quark-baryon phase, but this has yet to be investigated. The thermal runaway is blocked if the increase in temperature (width of the loop in Fig. 5.1) is enough to take the star from the negatively

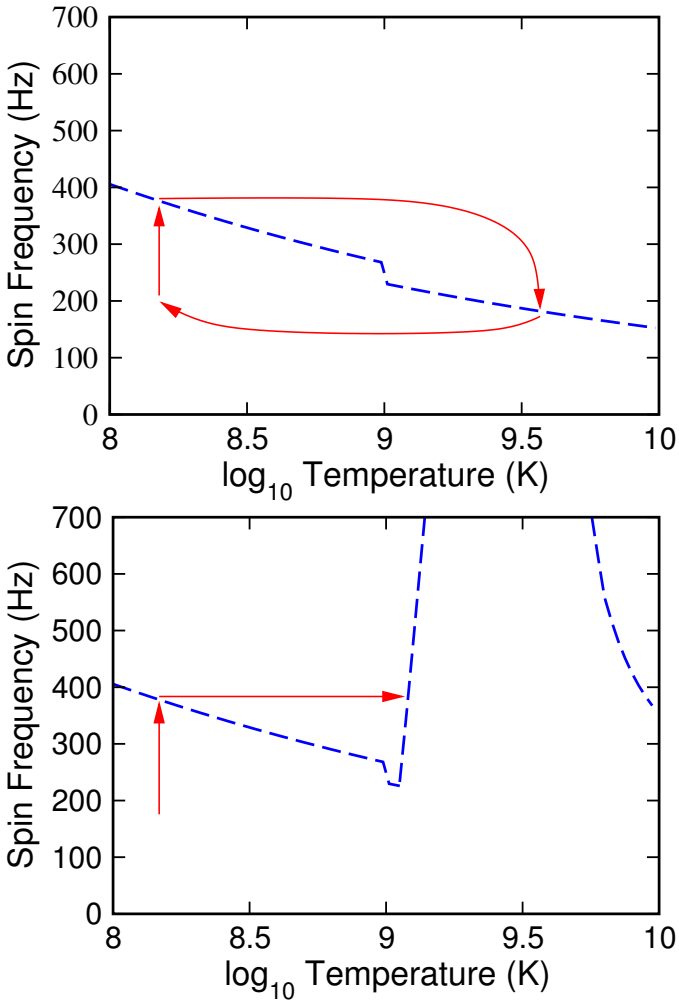

Figure 5.1: A typical critical frequency curve (critical frequency as a function of temperature of a neutron star) is given (qualitatively) by the dashed lines. The top plot includes no bulk viscosity due to hyperons or other strange particles. In this case an accreting neutron star traversing the loop indicated undergoes a thermal runaway and has a low gravitational radiation duty cycle. The bottom plot includes hyperon bulk viscosity. The critical frequency as a function of the temperature In this case the thermal runaway is blocked, and an accreting star is a source of persistent gravitational waves as it remains in equilibrium at the last arrowhead.

sloped part of the instability curve to the positively sloped part. The larger the saturation amplitude of r-modes the greater is the increase in the temperature. Whether the star makes the jump to the positively sloped curve also depends on which cooling mechanisms are operative, and on the shape of the low-temperature instability curve, which in turn depends on which damping mechanism dominates at low temperatures. Notwithstanding the wide range of estimates for α, the shape of the negatively sloped curve, and the cooling mechanisms, the question of the r-modes in LMXBs as a persistent source of gravitational radiation comes down to asking whether there is a rise in the instability curve around 10^9 K or lower.

Our purpose in this chapter is to revisit the question of whether there is a rise in the critical frequency curve around 10^9 K or lower, as in the bottom of Fig. 5.1, leading to persistent gravitational wave emission. We focus (for now) on neutron stars containing hyperons (hyperon stars), because hyperons are in some sense the most conservative and robust of the many proposals for exotic matter in the cores of neutron stars: Some properties of hyperons can be measured in the laboratory, both in vacuum and in the environment of a light nucleus, which combined with astronomical observations allows one to constrain some of the many uncertainties in building an equation of state [32, 46]. Equations of state which allow for hyperons generally produce them at densities relevant for neutron stars, about twice nuclear density and up.

We synthesize and extend results of previous work on this topic. In arguing the case for persistent gravitational wave emission, Wagoner [58, 119] and Reisenegger and Bonacic [118] base their critical frequency curves on bulk viscosity coefficients obtained by combining the results of Lindblom and Owen [56] (hereafter LO) and Haensel, Levenfish, and Yakovlev [57] (hereafter HLY). The LO and HLY viscosities were obtained by different calculations and produced somewhat different results. LO used a detailed self-consistent model of a multi-component fluid described by relativistic mean field theory [32], but since they were primarily concerned with the high-temperature regime appropriate to newborn neutron stars they treated the effect of superfluidity with a rough approximation. LO also made some errors which resulted in a bulk viscosity coefficient a factor of 20 or more too high. HLY were more careful with superfluidity, using consistent damping factors in the collision integrals, but instead of evaluating reaction rates and thermodynamic derivatives within relativistic mean field theory they used "order of magnitude estimates" of some quantities which resulted in more than an order of magnitude disagreement with the microscopic results of LO (and with Jones [106]). We correct some mistakes in LO and combine their self-consistent microphysical model with a more careful treatment of superfluidity similar to that of HLY. We also treat the macroscopic physics more carefully than LO, including the effect of rotation on stellar structure which in some cases can significantly affect damping timescales and critical frequency curves. (HLY made only order of magnitude estimates of mode damping

timescales and did not plot critical frequency curves.)

We also address the question "Does the viability of persistent gravitational wave emission require fine tuning of parameters?" Many of the parameters that go into building the equation of state have significant uncertainties, and those that go into computing reaction rates and bulk viscosities are even more uncertain. We investigate the viability of persistent gravitational wave emission with respect to variation of several microphysical numbers such as hyperon coupling constants and the superfluid bandgap, and even which nonleptonic reaction is most important (taking into account the results of van Dalen and Dieperink [107]). We also investigate the dependence on the mass of the star, since cooling observations [55] and timing of radio pulsars in binaries [43, 44] indicate a wider mass range than the traditionally assumed clustering around 1.4 $M_\odot$. (Cooling observations also might be interpreted to favor the existence of strange particles such as hyperons, although the data still can be fit by exotic cooling from purely nucleonic matter.)

The organization of the rest of the chapter is as follows. In Sec. 5.2 we describe the microphysical model which leads to the equation of state and ultimately the macroscopic coefficient of bulk viscosity. In Sec. 5.3 we plot the critical frequency curves for a range of neutron star masses and microphysical parameters. In Sec. 5.4 we summarize our findings and discuss possible improvements.

5.2 Microphysics

We model the composition of a neutron star within the framework of relativistic mean field theory industrialized by Glendenning and described in Ref. [32]. Here we do not consider meson condensates or exotica such as a mixed quark-baryon phase, but do allow for the presence of hyperons which are somewhat constrained by laboratory and astronomical data.

5.2.1 Equation of state

There are several free parameters in this framework, some of which are better known than others. We use a range of parameters set by combining the old laboratory constraints with recent astronomical observations [46]. At nuclear density (2–3$\times10^{15}$ g/cm^3) the matter is, as in all models, composed of neutrons, protons, electrons, and muons. As the density rises hyperons generically appear, their order of appearance (and density thresholds) changing somewhat with the precise set of parameter values but roughly corresponding to Σ^-, Λ, Σ^0, Σ^+, Ξ^-, starting at roughly twice nuclear density. Other baryons typically appear in this framework only at densities higher than those found in the cores of the most massive neutron stars, nearly 10 times nuclear density. At such high densities the asymptotic freedom of the strong nuclear force is likely to lead to quark matter anyway, and any baryonic model must be considered somewhat suspect. As we shall see, most of the astrophysically important

dissipation comes from lower densities (2–3 times nuclear density) where this deficiency of the model is not important, i.e. low-energy effective field theory is good enough. The framework of relativistic mean field theory has some advantages over others, such as an inherently causal equation of state even at high densities, but has some disadvantages including the neglect of correlations between particles which should become more important at high densities.

In this framework, the strong interaction between baryons is modeled as a tree-level exchange of isoscalar mesons σ, vector mesons ω, and isovector mesons ρ. The effective Lagrangian includes kinetic and tree-level interaction terms for the baryons, leptons, and mesons, as well as an effective potential for the σ expanded up to $O(\sigma^4)$. The variables of the theory are the Fermi momenta k_i of the baryons and leptons, supplemented by the field strengths of the σ, ω, and ρ mesons. Expansion coefficients and coupling constants can be fit to numbers extracted from measurements of nuclei and hypernuclei at saturation density. The fitting process (and Lagrangian) is described in detail in Ref. [32]. We use an updated set of fit parameters from Ref. [46].

For N species of baryons, two of leptons, and three of mesons, the composition of the matter consists of $N+5$ unknowns (the baryon, lepton and meson fields) which must be determined by $N+5$ equations. The first three equations are the Euler-Lagrange equations for the mesons determined by varying the effective Lagrangian of Ref. [32]. The equations are rendered tractable by assuming that the fields are given by their mean values in a uniform static ground state, and take the form

$$\omega_0 = \sum_B \frac{g_{\omega B}}{m_\omega^2} n_B, \tag{5.1}$$

$$\rho_{03} = \sum_B \frac{g_{\rho B}}{m_\rho^2} I_{3B} n_B, \tag{5.2}$$

$$m_\sigma^2 \sigma = \sum_B g_{\sigma B} \rho_{s,B} - b m_N g_\sigma (g_\sigma \sigma)^2 - c g_\sigma (g_\sigma \sigma)^3. \tag{5.3}$$

Here the index B labels baryon species, ω_0 is the timelike component of the vector meson field (the spatial components vanish), n_B is the number density of baryon B, and ρ_{03} is the isospin 3-component of the timelike component of the isovector meson field. Throughout this Section we use units such that $\hbar = c = 1$. The scalar density is given by

$$\rho_{s,B} = \sum_B \frac{2J_B+1}{2\pi^2} \int_0^{k_B} \frac{m_B^{\star 2}(\sigma)}{\sqrt{k^2 + m_B^{\star 2}(\sigma)}} k^2 dk. \tag{5.4}$$

The coupling constants between the baryon B and the mesons are given by $g_{\sigma B}$, $g_{\omega B}$, and $g_{\rho B}$. We assume, as in Ref. [32], that they are given by one set of values $(g_\sigma, g_\omega, g_\rho)$ for the nucleons and another $(x_\sigma g_\sigma, x_\omega g_\omega, x_\rho g_\rho)$ for the hyperons, so that the x's measure relative

coupling strengths for hyperons. The coupling constants for the self-interaction terms of the scalar field are b and c. The masses of the mesons are given by m_σ, m_ω, and m_ρ. The quantities for the Bth baryon I_{3B} and J_B are, respectively, its 3-component of isospin, and its spin. The Fermi momentum of the baryon species is given by k_B while its effective mass is given by $m_B^* = m_B - g_{\sigma B}\sigma$. The quantity m_N represents the average mass of a nucleon and is used to make b and c dimensionless. The constraints of charge neutrality and conservation of baryon number (if a particular baryon number density n is assumed) provide two more equations which can be written, respectively, as

$$\sum_i n_i q_i = 0, \tag{5.5}$$

$$\sum_B n_B = n. \tag{5.6}$$

Here n_i denotes the number density of fermion species i and q_i is its electric charge in units of e. Now we are down to N unknowns, which can be eliminated with the N equations of generalized β-equilibrium

$$\mu_i = b_i\mu_n - q_i\mu_e. \tag{5.7}$$

(The neutrinos are assumed to have zero chemical potential.) Here μ_i is the chemical potential of fermion species i and b_i is its baryon charge. (Actually there are $N+2$ equations of β-equilibrium including the leptons, but the equations for the electron and neutron are identities and thus do not count toward the elimination of unknowns.) The chemical potential of each baryon species is given by

$$\mu_B = g_{\omega B}\omega_0 + g_{\rho B}\rho_{03}I_{3B} + \sqrt{k_B^2 + m_B^{*2}}, \tag{5.8}$$

while that of each lepton species is given by

$$\mu_L = \sqrt{k_L^2 + m_L^2}. \tag{5.9}$$

Here k_L and m_L are, respectively, the Fermi momentum and mass of the Lth leptonic species.

For a given baryon number density n, the baryon, meson, and lepton fields are found by simultaneously solving Eqs. (5.1)–(5.7). The numerical technique is based on a multi-dimensional root finder and thus requires an initial guess to ensure finding the correct root. We first solve for a low value n below saturation density where the system can be approximated as a weakly interacting Fermi gas and analytic approximations can be found as in Ref. [32]. The code then steps up in baryon density n, at each step using the previous step's values for the unknowns as the initial guess for the root finder. Once the fields are

found for a given n, the mass-energy density ϵ and pressure p can be determined:

$$\begin{aligned}
\epsilon &= \frac{1}{3}bm_N\left(g_\sigma\sigma\right)^3+\frac{1}{4}c\left(g_\sigma\sigma\right)^4+\frac{1}{2}m_\sigma^2\sigma^2 \\
&+\frac{1}{2}m_\omega^2\omega_0^2+\frac{1}{2}m_\rho^2\rho_{03}^2 \\
&+\sum_B\frac{1}{\pi^2}\int_0^{k_B}\sqrt{k^2+m_B^{*2}}k^2dk \\
&+\sum_L\frac{1}{\pi^2}\int_0^{k_L}\sqrt{k^2+m_L^2}k^2dk, \qquad (5.10) \\
p &= -\frac{1}{3}bm_N\left(g_\sigma\sigma\right)^3-\frac{1}{4}c\left(g_\sigma\sigma\right)^4-\frac{1}{2}m_\sigma^2\sigma^2 \\
&+\frac{1}{2}m_\omega^2\omega_0^2+\frac{1}{2}m_\rho^2\rho_{03}^2 \\
&+\sum_B\frac{1}{\pi^2}\int_0^{k_B}\frac{k^4dk}{\sqrt{k^2+m_B^{*2}}} \\
&+\sum_L\frac{1}{\pi^2}\int_0^{k_L}\frac{k^4dk}{\sqrt{k^2+m_L^2}}. \qquad (5.11)
\end{aligned}$$

Here the summations are over the baryon species (B) and the lepton species (L). These expressions can be combined to produce tabulations of $p(\epsilon)$, the equation of state.

There remains the problem of choosing the values of the constants $(g_\sigma/m_\sigma)^2$, $(g_\omega/m_\omega)^2$, $(g_\rho/m_\rho)^2$, b, c, x_σ, x_ω, and x_ρ. Each choice of constants produces a different equation of state with different hyperon threshold densities, neutron star maximum mass, etc. We use five equations of state from [46] chosen to be compatible with recent measurements of neutron star masses [43, 44] and a gravitational redshift [45] as well as hypernuclear data [32]. The constants in Eqs. (5.1)–(5.7) are fit in the manner of Glendenning [32] to a Λ binding of -28 MeV, saturation density 0.153 fm^{-3}, binding energy per nucleon -16.3 MeV at saturation, and isospin asymmetry coefficient 32.5 MeV, as well as a range of incompressibilities K, nucleon effective masses m^*, and hyperon couplings x_σ. Since it is easiest to qualitatively understand the equations of state in terms of the latter three parameters, we give them in Table 5.1. Low K and high m^* lead to a soft equation of state, while high K and low m^* lead to a stiff equation of state. Since most of the matter in the star is at high density, the hard core repulsion dominates the strong interaction. Thus high x_σ postpones hyperon formation to higher densities, reducing hyperon populations (and thus viscosity) and stiffening the equation of state.

All of these equations of state are somewhat different from that used by LO and HLY. Though both HLY and LO use the "case 2" equation of state from an older paper by Glendenning [53], there were misprints in that paper which were corrected by HLY but not

Table 5.1: Parameters for five relativistic mean field equations of state used in this paper.

Name	K (MeV)	m^*/m_N	x_σ
H3	300	0.70	0.60
H4	300	0.70	0.72
H5	300	0.80	0.66
H6	240	0.70	0.67
H7	240	0.80	0.68

by LO. The scalar self interaction coupling constants b and c in Ref. [53] should be 3 and 4 times larger, respectively, than the values that are quoted for them. Also, case 2 of Ref. [53] used $K = 285$ MeV and $x_\sigma = x_\omega = x_\rho = \sqrt{2/3}$, and had several minor differences in other constants (we use values from the 2002 Particle Data Group review [121]). As a result, the newer equations of state we use have higher hyperon populations and thus higher viscosities.

5.2.2 Relaxation timescale

The reactions that contribute most to bulk viscosity are the weak interaction processes, as their relaxation timescales are within a few orders of magnitude of the r-mode period (milliseconds).

Among these, the most significant that can be calculated from first principles are the non-leptonic weak interactions involving the lightest hyperons, Σ^- and Λ, as they occur at lower densities than the more massive particles and thus have higher populations in a given star. Following LO, we calculate matrix elements for the reactions

$$n + n \leftrightarrow p + \Sigma^- \tag{5.12}$$

$$n + p \leftrightarrow p + \Lambda \tag{5.13}$$

as tree-level Feynman diagrams involving the exchange of a W boson. The latter reaction was also considered (with a phenomenological free parameters) by HLY. These reactions are combined to calculate an overall microscopic relaxation timescale. (This is the timescale on which a small perturbation of the neutron fraction returns to its equilibrium value.)

In addition to these reactions, Jones [106] includes

$$n + n \leftrightarrow n + \Lambda \tag{5.14}$$

which is the dominant nonleptonic process observed in Λ hypernuclei in the laboratory. We do not consider this reaction as it has no contribution based on a W-boson exchange, even though the bare-mass interaction rate for this process is known. Using Eq. (15) from Jones [106] we estimate that reaction (5.14) has a relaxation timescale that is longer than the timescale of the Λ reaction (5.13) by a factor of about 2 and thus does not change the final

viscosity much. (When accounting for the macroscopic structure of the star, the Σ^- process dominates the overall bulk viscosity since the Σ^- population extends to lower densities and therefore a greater volume fraction of the star than the Λ population.) There are various other concurrently occuring processes which contribute to the net reaction rate but their rates are not easy to predict. Even these rates are subject to substantial uncertainties: Van Dalen and Dieperink [107] use a meson-exchange model for all three hyperon reactions and find reaction rates of order 10–100 times greater than LO and thus bulk viscosity coefficients 10–100 times lower than LO. (As we shall see in the next section, such a change has less of an effect on the r-mode critical frequency than one might think.) Our result for the net rate is then a lower limit, and consequently an upper limit on the bulk viscosity, in the typical range of temperatures for LMXBs.

To summarize the results of LO, the relaxation timescale can be computed as a function of the equilibrium matter fields. Neglecting superfluidity, the result is

$$\frac{1}{\tau} = \frac{(kT)^2}{192\pi^3} k_\Sigma \langle|\mathcal{M}_\Sigma^2|\rangle \frac{\delta\mu}{n\, x_n} \tag{5.15}$$

when the Λ hyperons have not yet appeared and

$$\frac{1}{\tau} = \frac{(kT)^2}{192\pi^3} \left(k_\Sigma \langle|\mathcal{M}_\Sigma^2|\rangle + k_\Lambda \langle|\mathcal{M}_\Lambda^2|\rangle\right) \frac{\delta\mu}{n\, x_n} \tag{5.16}$$

when both Λ and Σ^- are present. Here kT is Boltzmann's constant times the temperature. The matrix elements $\mathcal{M}$ are computed as tree-level Feynman diagrams, squared, summed over initial spinors, and averaged over the angular part of the collision integral (indicated by $\langle\rangle$). (Note that van Dalen and Dieperink [107] do not angle average.) They are functions of the Fermi momenta and meson fields given by Eqs. (4.28) and (4.29) of LO,

$$\begin{aligned}
\langle|\mathcal{M}_\Lambda|^2\rangle &= \frac{G_F^2\sin^2 2\theta_C}{15}\left\{120\left(1-g_{np}^2\right)\left(1-g_{p\Lambda}^2\right)m_n^* m_p^{*2} m_\Lambda^* - 20\left(1-g_{np}^2\right)\left(1+g_{p\Lambda}^2\right)\right.\\
&\times m_n^* m_p^*\left(3\mu_p\mu_\Lambda - k_\Lambda^2\right) - 10\left(1+g_{np}^2\right)\left(1-g_{p\Lambda}^2\right)m_p^* m_\Lambda^*\left(6\mu_n\mu_p - 3k_n^2 + k_\Lambda^2\right)\\
&+2\left[\left(1+g_{np}^2\right)\left(1+g_{p\Lambda}^2\right)+4g_{np}g_{p\Lambda}\right]\left[5\mu_p\mu_\Lambda\left(6\mu_n\mu_p + 3k_n^2 - k_\Lambda^2\right)\right.\\
&\left.+k_\Lambda^2\left(10\mu_n\mu_p + 5k_n^2 + 10k_p^2 - k_\Lambda^2\right)\right] + \left[\left(1+g_{np}^2\right)\left(1+g_{p\Lambda}^2\right) - 4g_{np}g_{p\Lambda}\right]\\
&\times\left[10\mu_n\mu_\Lambda\left(6m_p^{*2} + 3k_n^2 + k_\Lambda^2\right)\right.\\
&\left.\left.+k_\Lambda^2\left(-20\mu_p^2 + 15k_p^2 - 3k_\Lambda^2 + 5(k_n^2-k_p^2)^2/(k_p^2-k_\Lambda^2)\right)\right]\right\}, \qquad (5.17)\\
\langle|\mathcal{M}_\Sigma|^2\rangle &= \frac{2}{15}G_F^2\sin^2 2\theta_C\left\{180\left(1-g_{np}^2\right)\left(1-g_{n\Sigma}^2\right)m_n^{*2}m_p^* m_\Sigma^* - 40\left(1-g_{np}^2\right)\left(1+g_{n\Sigma}^2\right)\right.\\
&m_n^* m_p^*\left(3\mu_n\mu_\Sigma - k_\Sigma^2\right) - 20\left(1+g_{np}^2\right)\left(1-g_{n\Sigma}^2\right)m_n^* m_\Sigma^*\left(6\mu_n\mu_p - 3k_p^2 + k_\Sigma^2\right)\\
&-5\left(1-g_{np}^2\right)\left(1-g_{n\Sigma}^2\right)m_p^* m_\Sigma^*\left(6\mu_n^2 + 6k_n^2 - 3k_p^2 - k_\Sigma^2\right) + 4\left[\left(1+g_{np}^2\right)\right.\\
&\times\left(1+g_{n\Sigma}^2\right)+4g_{np}g_{n\Sigma}\left]\left[10\mu_n^2\left(3\mu_p\mu_\Sigma + k_\Sigma^2\right) + 5\mu_p\mu_\Sigma\left(6k_n^2 - 3k_p^2 - k_\Sigma^2\right)\right.\right.\\
&\left.+k_\Sigma^2\left(10k_n^2 + 5k_p^2 - k_\Sigma^2\right)\right] + \left[\left(1+g_{np}^2\right)\left(1+g_{n\Sigma}^2\right) - 4g_{np}g_{n\Sigma}\right]\\
&\left[-10m_n^{*2}\left(3\mu_p\mu_\Sigma + k_\Sigma^2\right) + 10\mu_n\left(6\mu_n\mu_p\mu_\Sigma - 2\mu_p k_\Sigma^2 - 3\mu_\Sigma k_p^2\right.\right.\\
&\left.\left.\left.+\mu_\Sigma k_\Sigma^2\right) + 15k_p^2 k_\Sigma^2 - 3k_\Sigma^4\right]\right\}. \qquad (5.18)
\end{aligned}$$

We reproduce them here since the latter equation in LO is missing some terms (although the code used to generate the LO results is not missing them). Also, LO actually used kinetic energies instead of chemical potentials which should be used to be consistent with the quasiparticle picture of Fermi liquid theory. Correcting this reduces the relaxation time by a factor of 10 or more, making up much of the difference with the results of van Dalen and Dieperink [107] who use a drastically different model of the interaction. In the matrix elements, G_F is the Fermi constant and θ_C is the Cabibbo angle. The g's are axial-vector coupling constants, which we take to have their values measured from vacuum β-decay of particles at rest [121]. The remaining factor on the far right of Eqs. (5.15) and (5.16) is explained in the next subsection.

HLY, in contrast, used the nonrelativistic limit

$$\langle|\mathcal{M}_\Sigma|^2\rangle = 4G_F^2\sin^2 2\theta_C\left(1+3g_{np}g_{n\Sigma}\right)^2 \qquad (5.19)$$

of Eq. (5.18) and left the term in parentheses as a phenomenological parameter, which they simply set to 0.1. This is somewhat justified because the Particle Data group values for the couplings g_{np} and $g_{n\Sigma}$ result in a near-perfect cancellation of the term. Any in-medium change of these values would have a disproportionately large effect as a result. We (and LO) find that including the full Eq. (5.18) erases the effect of the near-cancellation of the leading-order terms and produces a running value of the term which can increase by more

than an order of magnitude above 0.1.

5.2.3 Bulk viscosity

We use for ζ, the macroscopic coefficient of bulk viscosity, the special relativistic expression derived by Lindblom and Owen [56]:

$$\zeta = \frac{p(\gamma_\infty - \gamma_0)\tau}{1 + (\hat{\omega}\tau)^2}. \tag{5.20}$$

where p is the pressure, $\hat{\omega}$ is the angular frequency of the r-mode in a frame corotating with the star, and τ is the net microscopic relaxation time we just computed. The fast adiabatic index γ_∞ (for infinite-frequency perturbations) can be written as

$$\gamma_\infty = \sum_i \frac{n_i}{n} \left(\frac{\partial p}{\partial n_i} \right), \tag{5.21}$$

where $n_i = k_i^3/(3\pi^2)$ is the number density of species i and the partial derivatives can be evaluated explicitly from Eq. (5.11). The slow adiabatic index γ_0 (for zero-frequency perturbations) can be written as

$$\gamma_0 = \left(\frac{n}{p} \right) \left(\frac{dp}{dn} \right), \tag{5.22}$$

and is straightforward to evaluate for example by differentiating the equation of state. However, while LO derived the correct relativistic expression and noted that it reduces the factor $\gamma_\infty - \gamma_0$ by a factor of 2–2.5 from the nonrelativistic expression, their Fig. 2 and code for the rest of the paper incorrectly used a data file with the nonrelativistic expression and thus are a factor 2–2.5 too high.

Now we address the factor $\delta\mu/\delta x_n$ in Eqs. (5.15) and (5.16) in the same manner as LO. This factor is determined by the constraints of charge and baryon conservation (5.5) and (5.6), plus the constraint that the reaction

$$n + \Lambda \leftrightarrow p^+ + \Sigma^- \tag{5.23}$$

is in equilibrium since its reaction rate is many orders of magnitude greater than the weak interaction rates. This implies that both the non-leptonic reactions have the same chemical potential imbalance:

$$\delta\mu \equiv \delta\mu_n - \delta\mu_\Lambda = 2\delta\mu_n - \delta\mu_p - \delta\mu_\Sigma. \tag{5.24}$$

Assuming small perturbations and using the neutron fraction x_n, this yields the relation

$$\begin{aligned}\frac{\delta\mu}{n_B\delta x_n} &= \alpha_{nn} + \frac{(\beta_n-\beta_\Lambda)(\alpha_{np}-\alpha_{\Lambda p}+\alpha_{n\Sigma}-\alpha_{\Lambda\Sigma})}{2\beta_\Lambda-\beta_p-\beta_\Sigma} \\ &\quad -\alpha_{\Lambda n} - \frac{(2\beta_n-\beta_p-\beta_\Sigma)(\alpha_{n\Lambda}-\alpha_{\Lambda\Lambda})}{2\beta_\Lambda-\beta_p-\beta_\Sigma},\end{aligned} \tag{5.25}$$

where β_i is given by

$$\beta_i = \alpha_{ni} + \alpha_{\Lambda i} - \alpha_{pi} - \alpha_{\Sigma i}. \tag{5.26}$$

and α_i is given by

$$\alpha_{ij} = \left(\frac{\partial\mu_i}{\partial n_j}\right)_{n_{k,k\neq j}}. \tag{5.27}$$

These expressions apply for densities where the Λ and Σ^- hyperons are both present. In the regime where only the Σ^- hyperon is present the strong interaction constraint is no longer a factor and one obtains a simpler form

$$\begin{aligned}\frac{2\delta\mu}{n_B\delta x_n} &= 4\alpha_{nn} - 2(\alpha_{pn}+\alpha_{\Sigma n}+\alpha_{np}+\alpha_{n\Sigma}) \\ &\quad +\alpha_{pp}+\alpha_{\Sigma p}+\alpha_{p\Sigma}+\alpha_{\Sigma\Sigma}.\end{aligned} \tag{5.28}$$

LO used numerical differencing to calculate the derivatives α_{ij}, but due to a coding error the σ meson field was not differenced properly. The maximum error this induces in the value of $\delta\mu/n_B\delta x_n$ is less than 0.3%, well below the uncertainties of the problem.

5.2.4 Superfluidity

In the temperature range of interest (below 10^{10} K), nucleons and hyperons are expected to form Cooper pairs near their Fermi surfaces and act as superfluids. This greatly slows reaction rates and has an important effect on transport coefficients such as bulk viscosity.

The energy associated with the Cooper pairing is given by the bandgap. Assuming $^1S_0$ pairing, the zero-temperature bandgap Δ_0 is related to the superfluid critical temperature T_C by [122]

$$kT_C = 0.57\Delta_0. \tag{5.29}$$

We use the LO fit to the finite-temperature bandgap

$$\Delta(T) = \Delta_0\left[1-\left(\frac{T}{T_C}\right)^{3.4}\right]^{0.53}. \tag{5.30}$$

For the Λ hyperons we use the empirical fit made by LO to the zero-temperature gap function $\Delta_{0\Lambda}$ of the Λ hyperon as computed by Balberg and Barnea [42]. The calculation

by Balberg and Barnea [42] is constrained by experiments on double Λ hypernuclei, though like other calculations of Δ_Λ it is likely only good to within a factor of 2 or 3. The zero-temperature gap depends on the total baryon number density n and on the Fermi momentum k_Λ in a way that LO found was well fit by

$$\begin{aligned}\Delta_{0\Lambda}\left(k_\Lambda, n\right) &= 5.1{k_\Lambda}^3\left(1.52 - k_\Lambda\right)^3 \\ &\times \left[0.77 + 0.043\left(6.2n - 0.88\right)^2\right]. \end{aligned} \tag{5.31}$$

Here $\Delta_{0\Lambda}$ is in MeV, k_Λ in fm^{-1}, and n in fm^{-3}. Thus the critical temperature for Λ superfluidity peaks somewhat below 10^{10} K.

The Σ^- superfluid bandgaps are not as well known as Δ_Λ due to the absence of similar experiments on hypernuclei containing the Σ^- hyperon. Determination of the hypernuclei energy levels for the Σ^- hyperon are constrained by the very short decay time of the hyperon. Takatsuka et al [123] have however calculated, using several models of the nuclear interaction, that the bandgap lies in the range $\Delta_\Lambda \leq \Delta_{\Sigma^-} \leq 10\Delta_\Lambda$. To account for the uncertainty in the bandgap we perform our calculation for two cases as in LO: when $\Delta_{\Sigma^-} = \Delta_\Lambda$ and when $\Delta_{\Sigma^-} = 10\Delta_\Lambda$.

For the superfluidity of protons we use model 2p of Ref. [124], which is one of the bandgap models used by HLY. (LO did not model proton superfluidity, since it was not relevant at the temperatures greater than 10^{10} K that they considered.) This bandgap model is not based on a specific calculation of the bandgap but preserves the general features of bandgaps predicted by various microscopic theories. In this model the zero temperature gap depends only on the Fermi momentum k_p of the proton. The relation for T_C is given by

$$T_C = T_0\left[\frac{k_p^2}{k_p^2 + k_1^2}\right]\left[\frac{(k_p - k_2)^2}{(k_p - k_2)^2 + k_3^2}\right], \tag{5.32}$$

where $k_1 = 1.117$ fm^{-1}, $k_2 = 1.329$ fm^{-1}, $k_3 = 0.1179$ fm^{-1} and $T_0 = 17 \times 10^9 K$. The Fermi momentum k_p is in fm^{-1} units and T_C is non-zero only if $k_p < k_1$. This leads to T_C for the protons peaking somewhat below 10^{10} K, similar to the Λ critical temperature.

Since neutrons are, after all, more abundant than other particles in neutron stars, they have higher energies and at supernuclear densities are unlikely to form $^1S_0$ pairs. They can have a $^3P_2$ pairing as considered in Ref. [124], but it is much weaker and corresponds to a maximum critical temperature $T_C \simeq 3 \times 10^8$ K. Below this temperature the contribution to the critical frequency curve from hyperon bulk viscosity is quite low, most of the contribution coming from viscosity at the crust-core interface. Therefore neutron superfluidity does not much affect the viability of persistent gravitational wave emission from the r-modes, and we neglect it here.

The effect of superfluidity on the microscopic relaxation timescale (5.15) or (5.16) ap-

pears, after doing the lengthy collision integrals (see HLY and LO), as multiplicative factors in the average matrix elements:

$$\langle|\mathcal{M}_\Sigma|^2\rangle \rightarrow R_{nnp\Sigma}\langle|\mathcal{M}_\Sigma|^2\rangle, \tag{5.33}$$

$$\langle|\mathcal{M}_\Lambda|^2\rangle \rightarrow R_{npp\Lambda}\langle|\mathcal{M}_\Lambda|^2\rangle. \tag{5.34}$$

If none of the participating particle species is superfluid, an R factor is 1. Each R factor is reduced as more species become superfluid. Our treatment of these factors is based on that used by HLY, who calculate R for the cases when either one or two of the particles participating in the reaction are superfluid. HLY do not however provide a 3-particle R which is required for calculating the timescale of the Λ reaction (5.13). Our numerical investigations found (see Section (5.3.3)) that expressing $R_{nnp\Sigma}$ as a product of two single-particle factors $R_pR_{\Sigma^-}$ instead of HLY's two-particle factor does not affect the r-mode critical frequency much. Therefore throughout this paper we express all R's as products of the appropriate single-particle factors. The expression for the single-particle R from Eq. (30) of HLY is

$$R = \frac{a^{5/4} + b^{1/2}}{2} \exp\left(0.5068 - \sqrt{0.5068^2 + y^2}\right), \tag{5.35}$$

where $y = \Delta(T)/kT$, $a = 1 + 0.3118y^2$ and $b = 1 + 2.566y^2$. LO used a simple factor e^{-y} for the hyperons only, since they were focusing on the ordinary fluid case. The exponential is indeed the dominant behavior of the HLY expression for $y \gg 1$, but the HLY expression is significantly more accurate for y less than about 5–10, which turns out to be the astrophysically interesting region.

We plot the most important results of our microphysics calculations. Figure 5.2 shows a typical relaxation timescale as a function of density, and Fig. 5.3 shows the corresponding bulk viscosity coefficient. Among the equations of state we use, H3 has a relaxation timescale in the middle of the distribution. Neglecting superfluidity, the timescales are about a factor of 40 shorter than in LO. About 20 of this comes from making the matrix elements consistent with the quasiparticle picture, and most of the rest comes from changes to the equation of state (including accounting for the typos in Ref. [53] which propagated to LO). Fig. 5.3 is reduced from LO by a further factor of 2 due to the relativistic factor $\gamma_\infty - \gamma_0$. Including superfluidity, the shapes of the curves are different from LO but the peak timescales are comparable. It is difficult to compare to HLY because at these temperatures the high-frequency approximation they use ($\hat{\omega}\tau \gg 1$) does not hold.

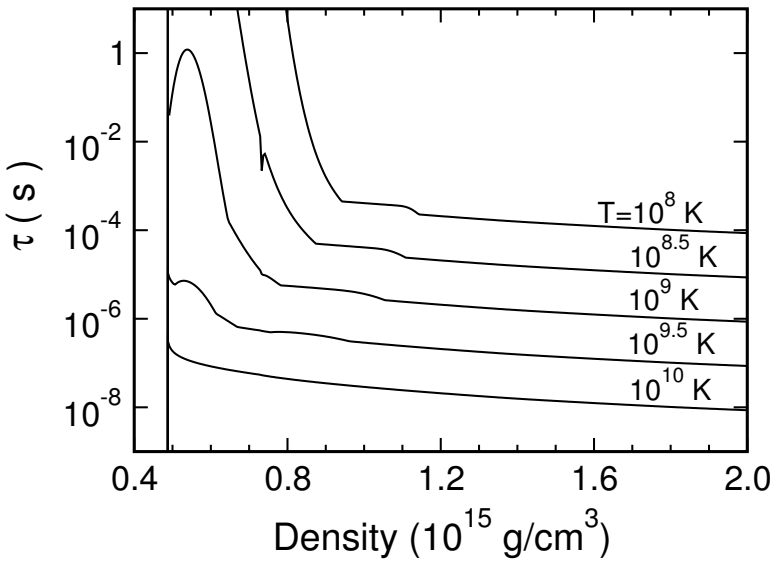

Figure 5.2: Microscopic relaxation timescale as a function of density for various temperatures. The equation of state is H3 and the Σ^- and Λ bandgaps are assumed equal. Thus at the highest temperature plotted, no superfluid effects are present.

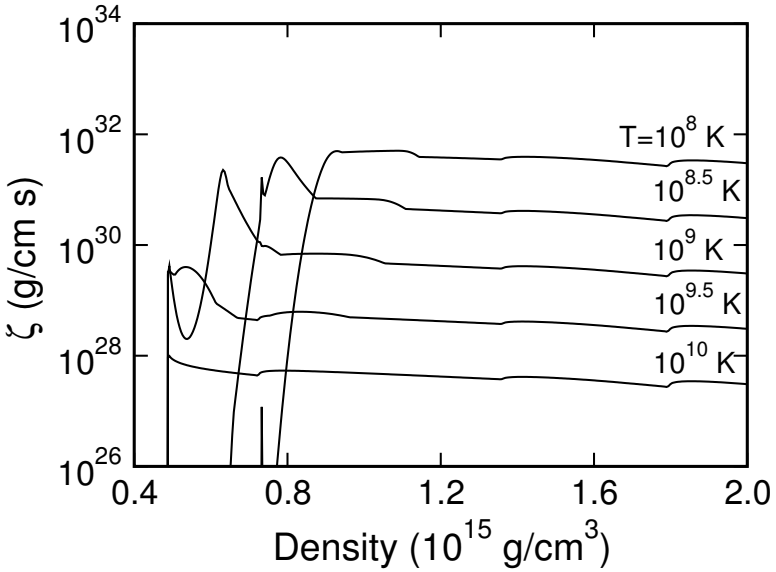

Figure 5.3: Bulk viscosity coefficient as a function of density for various temperatures, for the same model as Fig. 5.2. The star is rotating with angular frequency 2300 radians per second.

5.3 Macrophysics

With the bulk viscosity coefficient ζ in hand, we can proceed to compute r-mode damping times and critical frequencies. For this we also need the hydrodynamic structure of the r-mode as well as equilibrium models of the structure of a neutron star (i.e. its density profile).

5.3.1 Stellar structure

We are motivated by the sensitivity of the hyperon population to the central density to include the effects of general relativity and rotation in our stellar models. Relativistic stellar models have higher densities than nonrelativistic ones, and rotating models have lower densities than nonrotating ones. LO used relativistic, nonrotating stellar models; while other work such as HLY and Ref. [107] did not treat the stellar or mode structure in much detail. Since we are interested in exploring a broader parameter space, we do not restrict ourselves to nonrotating stars.

We take into account the effect of rotation on the neutron star structure using Hartle's slow-rotation approximation [125]. Hartle's formalism is based on treating a rotating star as a perturbation on a non-rotating star. We start by solving the Oppenheimer-Volkoff equations for a static spherically symmetric star in a form due to Lindblom [68]

$$\frac{dm}{dh} = -\frac{4\pi\epsilon(h)r(h)^3[r(h)-2m(h)]}{m(h)+4\pi r(h)^3 p(h)}, \tag{5.36}$$

$$\frac{dr}{dh} = -\frac{r(h)[r(h)-2m(h)]}{m(h)+4\pi r(h)^3 p(h)}, \tag{5.37}$$

using as independent variable the specific enthalpy

$$h(p) = \int_0^p dp'/[p'+\epsilon(p')]. \tag{5.38}$$

From $r(h)$, the radius at which the enthalpy is h, and $m(h)$, the mass contained within a sphere of that radius, we find $m(r)$. We also find $\nu(r)$, the logarithm of the time-time metric component which is based on $h(r)$. We then use this solution of the static star to solve for a rotating star with the same central pressure.

The metric of a slowly rotating star to second order in Ω, the spin frequency, can be

written as

$$\begin{aligned} ds^2 = & - e^{\nu}\left[1+2(h_0+h_2P_2)\right]dt^2 \\ & + \left[1+\frac{2(m_0+m_2P_2)}{(r-2M(r))}\right]\left[1-\frac{2M(r)}{r}\right]^{-1}dr^2 \\ & + r^2\left[1+2(v_2-h_2)P_2\right]\left[d\theta^2+\sin^2\theta(d\phi-\omega dt)^2\right] \\ & + O(\Omega^3). \end{aligned} \tag{5.39}$$

Here $P_2 = P_2(\cos\theta)$ is the 2nd order Lagrangian polynomial. The quantity ω is the frame dragging frequency that is proportional to Ω, while h_0, h_2, m_0, m_2, and ν_2 are all functions of r that are proportional to Ω^2. Before we solve the Einstein equations for all the subscripted quantities in Eq. (5.39) we need to solve for $\bar{\omega} = \Omega - \omega$. This is done by solving

$$\frac{1}{r^4}\frac{d}{dr}\left(r^4 j(r)\frac{d\bar{\omega}(r)}{dr}\right) + \frac{4}{r}\frac{dj(r)}{dr}\bar{\omega}(r) = 0, \tag{5.40}$$

with the definition

$$j(r) = \exp^{-\nu/2}\left[1-\frac{2M(r)}{r}\right]^{1/2}, \tag{5.41}$$

and the boundary conditions that at the center of the star $\bar{\omega}(0) = \bar{\omega}_i$, an arbitrary constant, and $(d\bar{\omega}(r)/dr)_{r=0} = 0$. From Eq. (5.40) one determines Ω and the angular momentum J corresponding to $\bar{\omega}_i$ as follows:

$$J = \frac{1}{6}R^4\left(\frac{d\bar{\omega}(r)}{dr}\right)_{r=R}, \tag{5.42}$$

$$\Omega = \bar{\omega}(R) + \frac{2J}{R^3}. \tag{5.43}$$

Here R is the radius of the star. To obtain the desired value of Ω one can scale $\bar{\omega}$ thus:

$$\bar{\omega}(r)_{new} = \bar{\omega}(r)_{old}(\Omega_{new}/\Omega_{old}). \tag{5.44}$$

The angular momentum J corresponding to Ω_{new} can then be calculated using Eq. (5.42).

A measure of the change in the star structure caused by rotation is $\xi(r,\theta)$ which represents the displacement of constant energy density surfaces between the rotating star and the corresponding non-rotating star. This displacement's angular dependence can be separated out:

$$\xi(r,\theta) = \xi_0(r) + \xi_2(r)P_2. \tag{5.45}$$

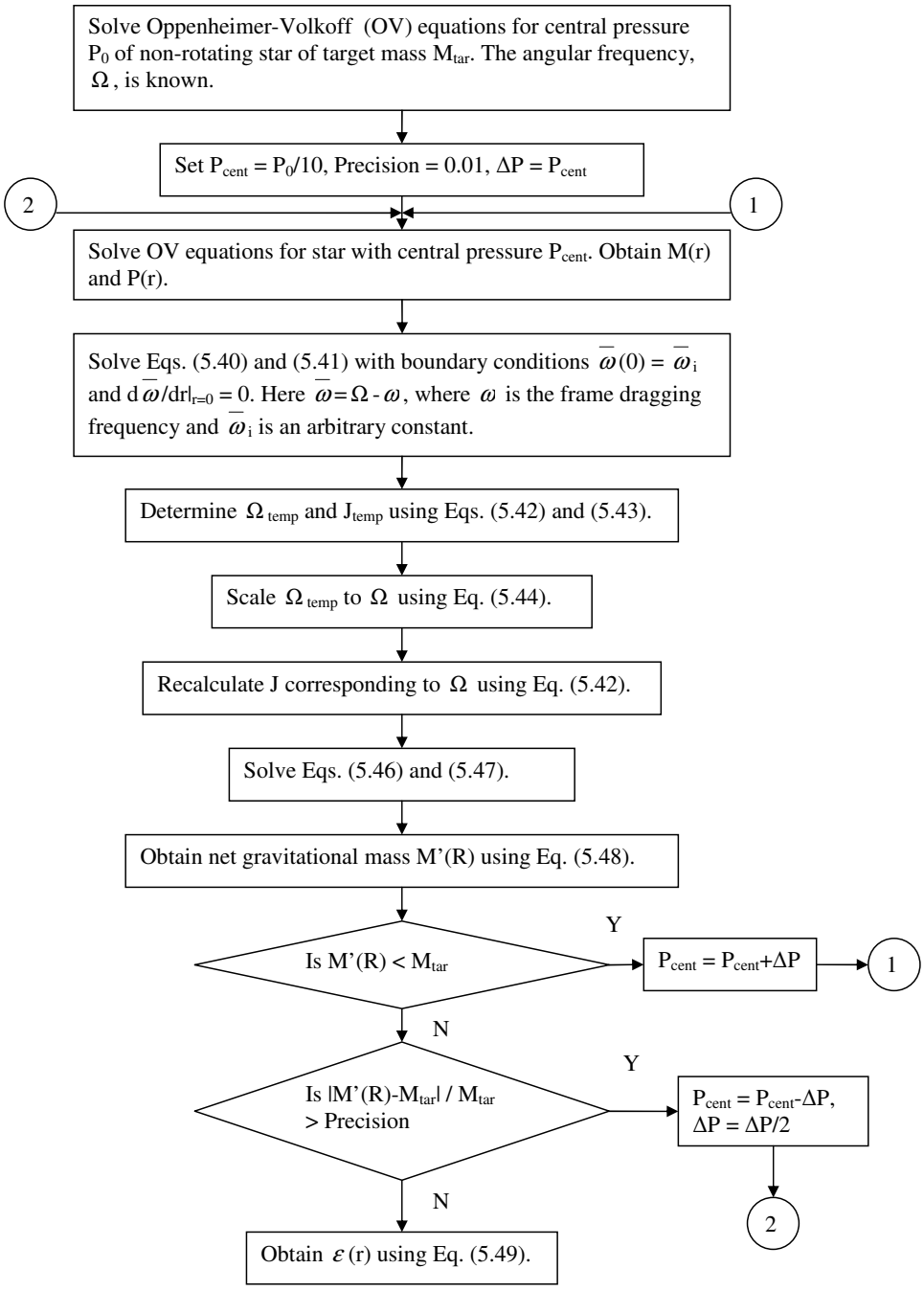

Figure 5.4: A graphical representation of obtaining the density profile of a rotating neutron star.

The $l = 0$ part of this deformation, ξ_0, can be obtained by solving the following equations:

$$\begin{aligned}
\frac{dm_0(r)}{dr} = &+ 4\pi r^2 \frac{d\epsilon(r)}{dp(r)} \left[\epsilon(r) + p(r)\right] p_0^*(r) \\
&+ \frac{1}{12} j^2(r) r^4 \left(\frac{\bar{\omega}(r)}{dr}\right)^2 \\
&- \frac{1}{3} r^3 \frac{dj^2(r)}{dr} \bar{\omega}^2(r), \qquad (5.46) \\
\frac{dp_0^*(r)}{dr} = &- \frac{m_0 \left[1 + 8\pi r^2 p(r)\right]^2}{r - 2M(r)} \\
&- \frac{4\pi \left[\epsilon(r) + p(r)\right] r^2}{r - 2M(r)} p_0^*(r) \\
&+ \frac{r^4 j^2(r)}{12\left[r - 2M(r)\right]} \left(\frac{d\bar{\omega}(r)}{dr}\right)^2 \\
&+ \frac{1}{3}\frac{d}{dr}\left(\frac{r^3 j^2(r) \bar{\omega}^2(r)}{r - 2M(r)}\right), \qquad (5.47)
\end{aligned}$$

where p_0^* is a pressure perturbation, the density profile $\epsilon(r)$ is the energy density of the non-rotating star as function of r, and $p(r)$ is the pressure of the star as a function of r. The boundary conditions for the above equations are that both m_0 and p_0^* vanish at the origin.

The gravitational mass of the rotating star is given by

$$M'(R) = M(R) + m_0(R) + \frac{J^2}{R^3}, \qquad (5.48)$$

which is greater than the mass of the nonrotating star with the same central pressure. We wish to build sequences of stars rotating at various rates all with the same gravitational mass. To do this we first solve the Oppenheimer-Volkoff equations; then, solve Eq. (5.40), (5.46), and (5.47); then calculate the new mass of the rotating star using Eq. (5.48). This procedure is repeated with lower values of the central pressure until the same mass as the nonrotating star is obtained.

To perform the viscosity calculations we need information on the structure of the rotating star contained in its density profile, a graphical representation of calculating which is given in Fig. 5.4. Once the correct mass is obtained the density profile $\epsilon(r)$ is calculated by using

$$\epsilon_{rot}(r) = \epsilon_{stat}(r) - \frac{d\epsilon_{stat}(r)}{dr} \xi_0(r), \qquad (5.49)$$

where

$$\xi_0(r) = -p_0^*(r) \frac{\epsilon(r) + p(r)}{dp(r)/dr}. \qquad (5.50)$$

Here, $\epsilon_{rot}(r)$ is the density profile of the rotating star, while $\epsilon_{stat}(r)$ is the density profile of the non-rotating one. This yields only the spherically symmetric part of the density perturbation, which is the dominant one for our purposes.

5.3.2 Driving and damping timescales

The stability of an r-mode is determined by calculating the damping and driving timescales. The mode is unstable if the driving timescale is shorter than the viscous damping timescale. This can be expressed in terms of an overall r-mode timescale τ_r such that

$$\frac{1}{\tau_r(\Omega,T)} = \frac{1}{\tau_{GR}(\Omega)} + \frac{1}{\tau_V(\Omega,T)}, \tag{5.51}$$

where $\tau_{GR} < 0$ is the damping timescale of the mode due to gravitational radiation and $\tau_V > 0$ is the damping timescale resulting from the sum of all viscous processes in the star. The star's spin angular frequency and temperature are represented by Ω and T, respectively. A mode unstable to gravitational radiation corresponds to $\tau_r < 0$ in Eq. (5.51), and the critical frequency Ω_c of the star as a function of temperature is found by solving $1/\tau_r(\Omega_c, T) = 0$.

The gravitational radiation timescale is given by

$$\frac{1}{\tau_{GR}} = -\frac{1}{2\tilde{E}}\left(\frac{d\tilde{E}}{dt}\right)_{GR}, \tag{5.52}$$

where $\tilde{E}$ is the mode energy in a frame rotating with the star and $(d\tilde{E}/dt)_{GR}$ is the rate at which energy is emitted in gravitational waves in the same frame. For the current quadrupole r-mode, there exist simple expressions (to lowest order in mode amplitude and angular velocity of the star) for the energy and gravitational radiation timescale: [73]

$$\begin{aligned} \tilde{E} &= \frac{1}{2}\alpha^2\Omega^2 R^{-2}\int_0^R \epsilon(r) r^6 dr, \\ \frac{1}{\tau_{GR}} &= -\frac{131\,072\pi}{164\,025}\int_0^R \epsilon(r) r^6\, dr. \end{aligned} \tag{5.53}$$

Here α is a dimensionless amplitude coefficient which cancels out of the driving and damping timescales.

The viscous damping time scale τ_V is given by

$$\frac{1}{\tau_V} = -\frac{1}{2\tilde{E}}\left(\frac{d\tilde{E}}{dt}\right)_V, \tag{5.54}$$

where $(d\tilde{E}/dt)_V$ is the rate at which energy is being drained from the mode by viscosity.

EOS	ϵ_c (10^{14}g/cm^3)	R (km)	R_Σ (km)	R_Λ (km)
H3	6.86	13.74	6.38	0.00
H4	6.12	13.85	4.50	0.00
H5	7.70	13.33	5.37	0.00
H6	7.84	13.44	6.70	2.46
H7	9.00	13.01	6.03	0.00

Table 5.2: Parameters of non-rotating $1.4M_\odot$ equilibrium stars for each equation of state (EOS). The central mass density is ϵ_c, R is the stellar radius, R_Σ is the distance out to which Σ^- hyperons appear, and R_Λ is the corresponding distance for Λ hyperons.

Here we consider only hyperon bulk viscosity from the nonleptonic processes discussed in the previous section. Leptonic (Urca) processes also contribute, but in LO they were shown to be overwhelmed by the viscosity due to nonleptonic processes. Although the crust-core viscosity is important at low temperatures—it determines the shape of the negatively sloped part of the instability curve which in turn puts a constraint on how much farther along the temperature axis the rising part of the instability curve should be located at to prevent a thermal runaway—we neglect it. For a reasonable estimate of the shape of the crust-core viscosity curve and of the value of the saturation amplitude the stars temperatures hould increase to around 10^9 K [116]. To explore the effect of the crust-core viscosity and the saturation amplitude in more details is beyond the scope of this paper. We can then compute the viscous damping timescale as in LO: To lowest order in Ω, we can write

$$\left(\frac{d\tilde{E}}{dt}\right)_V = -4\pi \int_0^R \zeta(\epsilon(r))\langle|\vec{\nabla}\cdot\delta\vec{v}|^2\rangle r^2\, dr, \tag{5.55}$$

where $\langle|\vec{\nabla}\cdot\delta\vec{v}|^2\rangle$ is the angle average of the square of the hydrodynamic expansion. LO found that the expansion found numerically in Ref. [126] could be fit well by

$$\langle|\vec{\nabla}\cdot\delta\vec{v}|^2\rangle = \frac{\alpha^2\Omega^2}{690}\left(\frac{r}{R}\right)^6\left[1+0.86\left(\frac{r}{R}\right)^2\right]\left(\frac{\Omega^2}{\pi G\bar{\epsilon}}\right)^2, \tag{5.56}$$

where $\bar{\epsilon}$ is the mean density of the (nonrotating) star. [In Eq. (6.6) of LO the last factor is missing due to a misprint, but is properly included in the calculations.] This approximation breaks down for $r/R \approx 1$, but since the bulk viscosity is coming from the hyperon core that is enough. In Table 5.2 we give typical radii of nonrotating stars and their hyperon cores.

5.3.3 Critical frequency curves

We are now in a position to solve for the critical frequency as a function of temperature for various neutron star models. This must be done numerically.

Because of the inclusion of rotation the process is somewhat more involved than in LO.

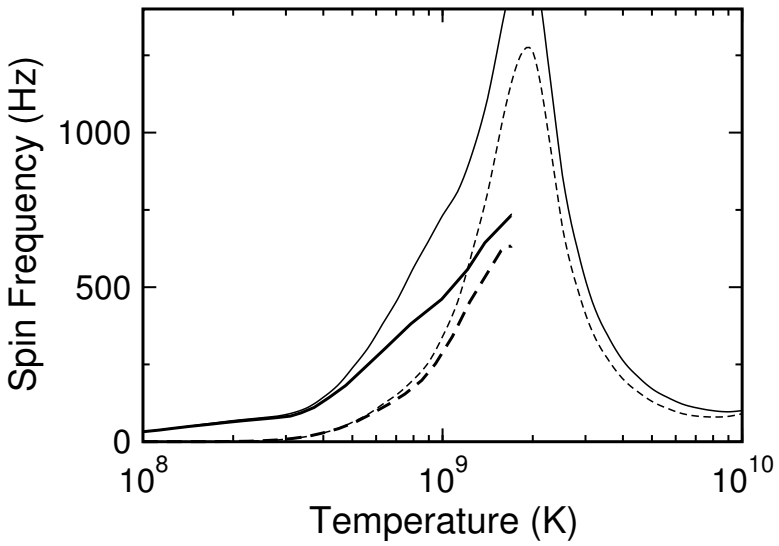

Figure 5.5: Critical frequency curves for $1.4M_\odot$ neutron stars with equal bandgaps for Σ^- and Λ hyperons. The dashed curve is for equation of state H3 and the solid curve is for H6. The thinner curves neglect the effect of rotation on stellar structure while the thicker curves include it. The curves including rotation are extended to their peaks, but no further.

The critical frequency curve is calculated in two stages to ensure that the correct gravitational mass is retained after including the corrections to it from rotation. In the first stage we calculate the critical frequency as a function of temperature for a nonrotating star using the Oppenheimer-Volkoff formalism. Then a set of points on this curve is taken. In the second stage, for each point we find the structure (density profile) of a star rotating at that frequency with the same gravitational mass as the nonrotating star. Since Hartle's formalism produces stars with greater gravitational masses, this step requires several iterative trials of the central pressure to find the star with the same gravitational mass. Using the new density profile with rotation, we keep the frequency fixed and use the corresponding temperature on the nonrotating curve as an initial guess for a routine that finds the root of $1/\tau_r$, thereby obtaining the correct temperature for the marginally star rotating at that frequency. Because of this it is cumbersome to trace out parts of the curves where the critical frequency decreases with temperature, and since those parts of the bulk viscosity curves are not important for determining the viability of persistent gravitational wave emission we neglect them.

The importance of rotation is shown in the critical frequency curves plotted in Fig. 5.5. (Kepler frequencies for these equations of state are 750–850 Hz for 1.4 $M_\odot$ stars.) Equation of state H6 is soft and has the highest hyperon population for a given mass, and thus its curve is higher than for H3 which is intermediate. This plot shows the general trend that the effect of rotation is more significant for softer equations of state. For persistent

gravitational wave emission the key question is whether or not a neutron star undergoing thermal runaway will be blocked by hitting the curve at a temperature lower than a few times 10^9 K. Even for the soft H6 equation of state, the effect of rotation on stellar structure changes the temperature at which a star hits the curve by no more than a factor of 2 (still within the region that is good for gravitational wave emission). More significant is the fact that the frequency at which the curve peaks can be considerably reduced from the value neglecting rotation. If the peak is low enough, thermal runaway can still occur—for example in this plot it can occur for H3 stars if they hit above 700 Hz—and the outlook is bad for persistent gravitational wave emission.

In Fig. 5.6 we show the effect of the equation of state on the critical frequency curve for 1.4 $M_\odot$ stars. The curves generically reach their peak at temperatures of 1–2$\times 10^9$ K, which is good for persistent gravitational wave emission. However, the heights (frequencies) of the peaks change significantly. The peak is highest for H6, which has the largest hyperon population. It is almost identical for H3 and H7, although those two equations of state are the furthest separated in the (K, m^*, x_σ) parameter space. This seems to be due to the similar radii of their hyperon-containing cores as in Table 5.2. All three of these equations of state then allow persistent gravitational wave emission in 1.4 $M_\odot$ stars. The peak is lowest for H4, which is not surprising since that is the stiffest equation of state and has the lowest hyperon population. For H4 the peak is so low that, depending on the details of the crust-related damping, the full curve including that damping might show no significant effect from hyperon bulk viscosity—it might decrease throughout the temperature range and never allow persistent emission. In any case, for H4 and H5 persistent emission is not possible for the most rapidly rotating stars in LMXBs (up to 619 Hz) if they are 1.4 $M_\odot$. This demonstrates in principle how observation of r-mode gravitational waves from an LMXB could rule out some equations of state or, more broadly, constrain hyperon populations.

In Fig. 5.7 we plot critical frequency curves for stars with different masses for the H4 equation of state, which is the stiffest of those we use. (For other equations of state, the stellar mass affects the curve more but is constrained to a narrower range, so the overall variation is greatest for H4.) We also vary the Σ^- bandgap from the Λ value to 10 times that value. It can be seen that increasing the mass pushes the curve to lower temperatures and raises its peak. This is due to the fact that higher mass stars have higher central densities and hence, in absolute terms, larger hyperon populations than their lower mass counterparts. Persistent r-mode gravitational wave emission is viable in all but the 1.4 $M_\odot$ neutron stars. The temperature at which this can happen is strongly dependent on the mass, and to a lesser but still significant extent (factor 3) on the Σ^- bandgap, with higher bandgaps leading to higher temperatures at a given frequency. (The small horizontal sections of the $1.4M_\odot$ and $1.6M_\odot$ large bandgap curves should actually dip slightly. This behavior is missed due to our method of including rotation, but is unimportant for the thermal runaway and persistent

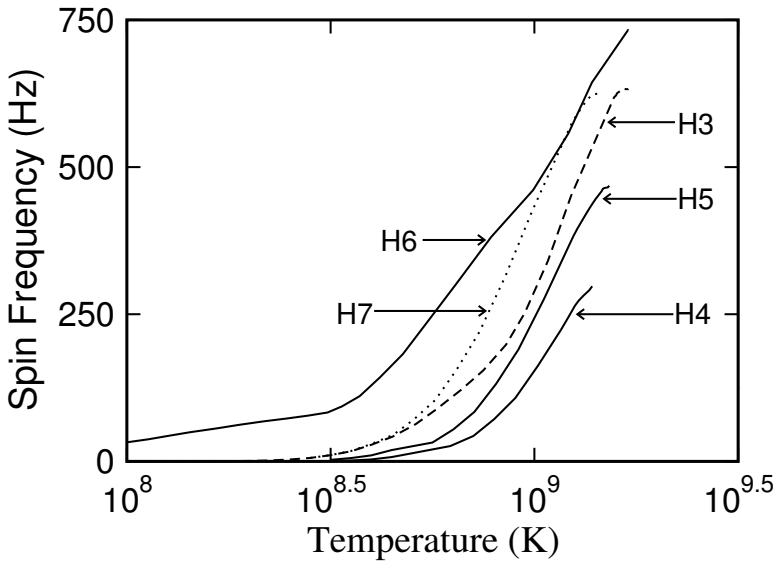

Figure 5.6: Critical frequency as a function of temperature for 1.4 $M_\odot$ stars with different equations of state. All curves assume the superfluid bandgaps of the Λ and Σ^- hyperons are equal.

gravitational wave emission.)

The curves for 1.8–2.0 $M_\odot$ stars are particularly interesting in light of predicted interior temperatures of neutron stars in LMXBs. These can be determined from observations in quiescence of the surface temperatures of three slowly accreting neutron stars mentioned in Brown, Bildsten, and Chang [127]. To calculate the interior temperatures we use Fig. 2 from Yakovlev et al [128], which depicts the relationship between the core and the measured surface temperatures using different atmospheric and equation of state models. We thereby obtain a temperature range (1.5×10^7–4×10^8K) which covers LMXBs whose thermal emission spectra have been observed. This result is probably statistically biased, since LMXBs with higher accretion rates are likely to have higher temperatures but surface temperatures are harder to observe because of the accretion discs. At any rate, the most massive H4 stars have critical frequency curves which would allow gravitational wave emission scenarios [58, 118] to operate in that temperature range. Less massive stars allow it at higher temperatures, which may be consistent with the more rapidly accreting neutron stars such as Sco X-1 whose temperatures are poorly known.

The effects of varying some additional microphysical parameters are shown in Fig. 5.8, which depicts curves for 1.4 $M_\odot$ neutron stars with the H3 equation of state and the Σ^- superfluidity bandgap equal to that of the Λ. The variations include using the asymptotic (quark) values for the axial-vector couplings in the reaction rates, using HLY's two-particle superfluid reduction factor instead of the product of two one-particle factors, and using

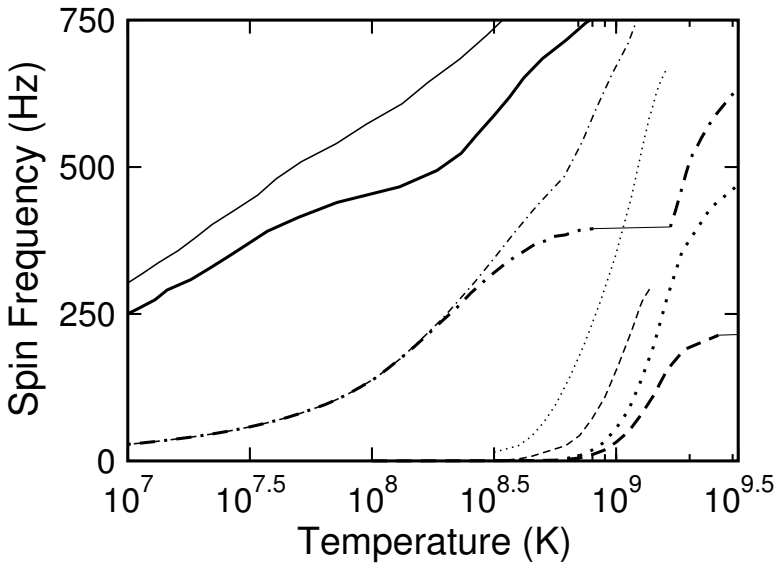

Figure 5.7: Instability curves for H4 stars with different masses. The thicker curves use the larger Σ^- bandgap while the thinner curves use the smaller one. The solid lines represent $2.0M_\odot$ stars, the dot-dash lines repsents $1.8M_\odot$ stars, the dotted line represents $1.6M_\odot$ stars, and the dashed line represents $1.4M_\odot$ stars.

relaxation times an order of magnitude faster from van Dalen and Dieperink [107]. All of these curves peak at almost identical frequencies, and the temperature at a fixed frequency changes by less than a factor of 1.5 Therefore, the changes to these microphysical parametrs do not affect our earlier conclusions. From an astrophysical point of view, the most sensitive unknowns in this complicated calculation are the hyperon population (thus the equation of state and stellar mass) and superfluid bandgaps. At a very simple level this makes sense because the hyperons appear only after a threshold density and the bandgaps appear in exponential factors rather than power laws.

5.4 Discussion

We have extended previous investigations of r-modes in accreting hyperon stars in LMXBs as persistent sources of gravitational waves, focusing on the bulk viscosity which is needed to prevent thermal runaway. We have used improved microphysics compared to previous treatments, and have accounted for the most important macroscopic correction due to rotation of the star.

We find that persistent gravitational wave emission is quite robust. Even the stiffest hyperonic equations of state in relativistic mean field theory produce enough damping to stop the runaway and persistently radiate, although some of them require neutron stars

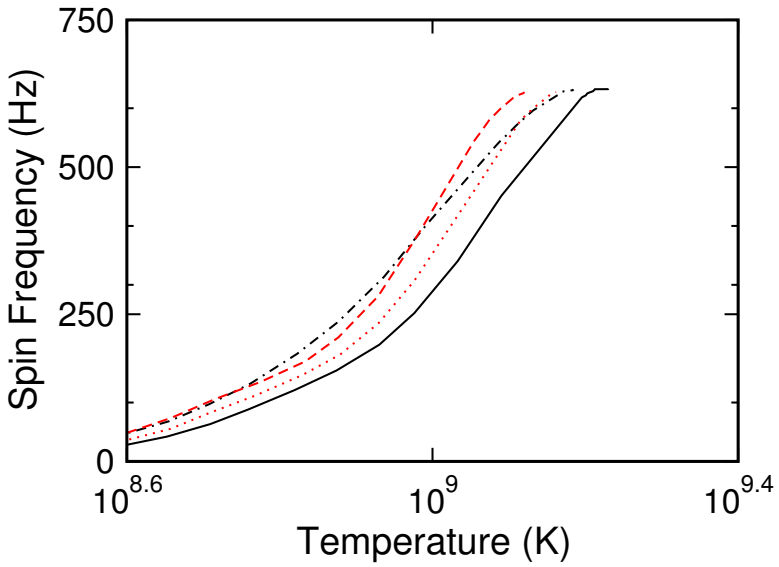

Figure 5.8: Variations on the critical frequency curve for a 1.4 $M_\odot$ H3 star with equal Λ and Σ^- bandgaps. The solid curve is our standard model. The dotted curve uses asymptotic values for the axial couplings instead of vacuum at-rest values. The dot-dash curve uses the 2-particle superfluid reduction factor for the Σ^- interaction instead of two 1-particle factors. The dashed curve simulates the fast timescales predicted by van Dalen and Dieperink.

somewhat more massive than 1.4 $M_\odot$. Stars below about 1.3 $M_\odot$ are not likely to be persistent sources regardless of the equation of state. The mass thresholds are somewhat more favorable for lower superfluid bandgaps than for higher bandgaps. Other details of the microphysics are found to be considerably less important. Our results seem robust for typical values of the crust-core viscosity and of saturation amplitude of r-modes, though this issue requires further investigation. Stars with high masses and stiff equations of state could exist in thermal and torque equilibrium at temperatures down to 10^7 K.

One possible avenue for substantial improvement is the hydrodynamics. We used a fluid expansion in the dissipation integrals which is a reasonable approximation for a Newtonian normal fluid, but not for a superfluid which can be much more complicated due to multiple components and entrainment. Work is underway to deal with the superfluid problem in general ([129] and references therein).

Chapter 6

Hybrid Stars

6.1 Introduction

Hybrid stars are neutron stars with a core consisting of an exotic phase of mixed quark and baryonic matter [32]. The possible existence of the mixed phase has been the subject of much interest from nuclear physicists and astrophysicists since its discovery 15 years ago [33], and lately has become of great interest in the context of gravitational waves. Rough estimates [27, 31] indicate that some stars with exotic equations of state could sustain quadrupole moments large enough for gravitational radiation from them to be detectable by LIGO at its present sensitivity ("initial LIGO") rather than after upgrades in a few years ("advanced LIGO").

There are several types of exotic matter that could lead to stars with quadrupoles larger than normal neutron stars. In the normal matter neutron star model the quadrupole moment results from elastic deformations of the thin solid crust (see Ref. [29] and references therein), while the rest of the star is liquid. In terms of a dimensionless ellipticity (defined precisely below), normal neutron stars are estimated to sustain ellipticities at most a few times 10^{-7} [29]. The highest ellipticities (detectable by initial LIGO) are allowed in a model of completely solid strange quark stars by Xu [30] and have been estimated by Owen [31] to be a few times 10^{-4}. The difference is mostly due to a thousandfold increase in the shear modulus of the matter. More recently Mannarelli, Rajagopal, and Sharma [130] have evaluated the shear modulus of quark matter exhibiting crystalline color superconductivity (CCS). The quarks that exhibit CCS form non-BCS types of pairings, i.e. the total momentum of each Cooper pair is non-zero. The CCS phase behaves like a solid whose shear modulus is 20–1000 times greater than typical values for neutron star crusts, leading to ellipticities similar to those for Xu's model. The CCS model is better grounded in QCD than Xu's model, but both are fairly speculative in that they require extremely high densities and it is not clear if such densities are achieved in stable stars.

Other, more robust models involve a gradual phase transition from normal nuclear matter to other exotic matter states in the high density regions of the star [33]. Gradual phase transitions generically result in the formation of a crystalline lattice which can have a high shear modulus and thus is capable of sustaining large elastic deformations. The phase

transition may involve the formation of a charged kaon condensate or a move to quark matter at high densities as is indicated by asymptotic freedom. The latter type of star is known as a hybrid star. Mechanically it consists of a thin solid crust, underlaid by a liquid nuclear matter mantle, with a solid core of mixed quark/baryon matter. (In principle a transition to pure quark matter in the inner core is possible, but we find that this does not happen for realistic stars.) The maximum ellipticities of these quark/baryon hybrid stars (hereafter, hybrid stars) have been estimated by Owen [31] to be about 10^{-5}. However, that estimate was based on several very rough approximations. The goal of this Chapter is to firm up Owen's estimate with a more detailed calculation.

Our first improvement on the work of Owen [31] is a self-consistent calculation of the microphysical properties of the model within the framework of Glendenning [32]. We assume that the corrections to the total energy density resulting from crystallization are small. This enables us to divide our calculation into two parts: We first calculate the large-scale structure of the star using the Oppenheimer-Volkoff equations, following which we calculate the details related to the formation of a lattice including the shear modulus. For the baryonic equation of state we use, as in the rest of this thesis, the relativistic mean field theory framework [32]. For the quark equation of state we use a framework that is based on the MIT bag model and includes corrections from perturbative QCD. We explain how the mixed phase equation of state is obtained by relaxing the local conservation laws and making them global. We constrain the equations of state using the latest neutron star mass and gravitational redshift observations. We find that the hybrid equations of state in the literature cannot account for these observations. We therefore generate new equations of state from the available parameter space which satisfy the observational constraints.

For each equation of state we compute additional microscopic properties needed for the shear modulus. The shape of the embedded phase in the crystalline lattice depends on the Coulomb interaction between the two phases and the surface energy of the embedded phase. Once the shape is known we can calculate the half-length dimensions and the spacings between the embedded lattice points. Using the half-lengths and spacings we calculate the shear modulus of the configuration. We estimate the effect of charge screening on the shear modulus in a self-consistent way, where Owen patched together existing results from the literature.

Finally, using the shear modulus and the simple hydrostatic equations [29, 31] we determine the maximum ellipticities for various hybrid stellar models. We compare the results with the first estimates for hybrid stars [31] and comment on the implications for gravitational wave observations.

6.2 Equations of state

For hybrid stars which show a phase transition to quark matter at high densities we need to consider two equations of state, a hadronic equation of state for the outer lower-density parts of the star and a quark equation of state for the inner high density part of the star. The equation of state for the intermediate density region of the star where the two phases coexist is constructed from both of these equations of state.

The mantle of the star is likely to have no quark content and requires a hadronic equation of state. We use a hadronic equation of state based on relativistic mean field theory [32]. How this equation of state is obtained is explained in 2.2 and 5.2.1, here we repeat a few key steps. In this theory the strong force is modeled as an exchange of mesons (scalar σ, vector ω, and isoscalar ρ) between baryons which include protons, neutrons, and, at higher densities, also hyperons. The starting point is the Lagrangian for the theory which is a combination of the free particle Lagrangian terms for the mesons and the baryons, of terms corresponding to the interaction of each meson with each of the baryons, and also two scalar meson self-interaction terms. From the Lagrangian we determine the Euler-Lagrange equations for each of the mesonic and baryonic fields under the assumption that matter is in its static and homogeneous ground state. This assumption allows us to simplify the equations by setting their spatial terms to zero. We also have additional equations corresponding to the requirements of charge neutrality, baryon conservation, and generalize-β equilibrium in a neutron star. This system of equations in which the dependent variables are the mesonic mean fields and the Fermi momenta of the baryons is solved as a function of the hadronic number density, n, which is the independent variable. Now we can write the pressure and energy density as functions of the hadronic number density, thereby determining the equation of state.

The inner parts of neutron stars contain up (u), down (d), and strange (s) quarks, (charm quarks being heavier are unlikely to exist in neutron stars), and electrons and muons. We model the quarks as a degenerate Fermi gas using the MIT bag model modified by QCD corrections to take into account the fact that the densities are not high enough for asymptotic freedom.

Our starting point for determining the quark equation of state is not the Lagrangian as it was for the baryonic case. Instead, we start by calculating correlation functions in perturbative QCD. These correlation functions give the grand partition function as a series in α_s, the strong coupling constant. Once the grand partition function is known we can calculate the thermodynamic potential $\tilde{\Omega}$ (sometimes also known as the grand potential)

whose relationship with the grand partition function is given by

$$\Xi = \exp\left(-\frac{\tilde{\Omega}}{kT}\right). \tag{6.1}$$

Here, k is the Boltzmann constant while T is the temperature.

The expression for the thermodynamic potential, Ω_f (Ω without the tilde refers to the thermodynamic potential per unit volume), for each quark, f, to the first order in α_s is given by [32, 131]

$$\begin{aligned}
\Omega_f \;=\; & -\frac{1}{4\pi^2}\left\{\mu_f\sqrt{\mu_f^2-m_f^2}\left(\mu_f^2-\frac{5}{2}m_f^2\right)+\frac{3}{2}m_f^4\log\left[\frac{\mu_f+\sqrt{\mu_f^2-m_f^2}}{m_f}\right]\right. \\
& -\frac{2\alpha_s}{\pi}\left[3\left(\mu_f\sqrt{\mu_f^2-m_f^2}-m_f^2\log\left[\frac{\mu_f+\sqrt{\mu_f^2-m_f^2}}{\mu_f}\right]\right)^2\right. \\
& -2(\mu_f^2-m_f^2)^2-3m_f^4\log^2\left(\frac{m_f}{\mu_f}\right) \\
& \left.\left.+6\log\left(\frac{\sigma}{\mu_f}\right)\left(\mu_f\sqrt{\mu_f^2-m_f^2}m_f^2-m_f^4\log\left[\frac{\mu_f+\sqrt{\mu_f^2-m_f^2}}{m_f}\right]\right)\right]\right\}.
\end{aligned} \tag{6.2}$$

The mass of each quark flavor f is denoted by m_f, while the chemical potential μ_f is given by

$$\mu_f = \sqrt{m_f^2+k_f^2}, \tag{6.3}$$

where k_f is the Fermi momentum of the quark. The parameter σ is a renormalization scale that provides an infrared cutoff for the calculation of the QCD correlation functions. The expression Eq. (6.2) given here is from Glendenning's book [32] which corrects a typo in the journal article by Farhi and Jaffe [131]. For massless quarks, which is a good approximation for up and down quarks, the expression reduces to

$$\Omega_f = -\frac{\mu_f^4}{4\pi^2}\left[1-\frac{2\alpha_s}{\pi}\right]. \tag{6.4}$$

We also considered the effect of color-flavor-locked (CFL) superconductivity on the quark equation of state. The CFL phase occurs only at very high densities when the mass of the strange quark is small compared to the quark Fermi momenta, and the quarks all have equal chemical potentials. The contribution from CFL conductivity to the chemical potential of each quark is [132]

$$\Omega_{CFL} = -\frac{\Delta^2}{\pi^2}\mu_f^2, \tag{6.5}$$

where Δ is the superconducting bandgap whose values lie in the 10-100 MeV range in the relevant neutron star density regime. We found that the CFL phase comes in at densities that exceed the central densities of the maximum mass stars of all the equations of state we consider.

The thermodynamic potential allows us to calculate analytic expressions for all the thermodynamic quantities required in the calculation of the equation of state. We can obtain the number densities of the quarks using the thermodynamic potential which is defined as

$$\tilde{\Omega} = -pV = E - TS - \mu N, \tag{6.6}$$

where p is the pressure, V the volume, E the internal energy, S the entropy, μ the chemical potential, and N the number of particles. From the differential of Eq. (6.6) we obtain

$$d\tilde{\Omega} = dE - Tds - SdT - \mu dN - Nd\mu, \tag{6.7}$$

which can be simplified using the first law of thermodynamics, $dE = TdS - pdV + \mu dN$, to obtain

$$d\tilde{\Omega} = -pdV - SdT - Nd\mu. \tag{6.8}$$

It is clear from this equation that the number density, n_f, of each quark flavor can be written as

$$n_f = -\partial\Omega_f/\partial\mu_f, \tag{6.9}$$

where Ω is the thermodynamic potential per unit volume.

For the quark equation of state we solve a set of equations for the Fermi momenta of the different particle species as a function of the baryonic number density (a third of the total quark number density). Two of the equations that express chemical equilibrium in the system can be obtained from the following weak interaction processes:

$$\begin{aligned} d &\leftrightarrow u + e + \bar{\nu}, \\ s &\leftrightarrow u + e + \bar{\nu}. \end{aligned} \tag{6.10}$$

Chemical equilibrium of these interactions implies the following relationships between the particle chemical potentials

$$\begin{aligned} \mu_d &= \mu_u + \mu_e, \\ \mu_s &= \mu_u + \mu_e. \end{aligned} \tag{6.11}$$

Another set of weak interactions is obtained by replacing the electrons in Eq. (6.10) by

muons which gives

$$\mu_e = \mu_\mu. \tag{6.12}$$

The constraints of charge neutrality,

$$\frac{2}{3}n_u - \frac{1}{3}n_d - \frac{2}{3}n_s - n_e - n_\mu = 0, \tag{6.13}$$

and baryon number conservation,

$$\frac{1}{3}\left(n_u + n_d + n_s\right) = n, \tag{6.14}$$

complete the set of equations to be solved.

The equation of state is now obtained by determining the pressure and energy density using the following expressions

$$p_Q = -B - \sum_f \Omega_f + \frac{1}{3}\sum_j \frac{1}{\pi^2}\int_0^{k_j} \frac{k^4\, dk}{\sqrt{k^2 + m_j^2}}, \tag{6.15}$$

$$\epsilon_Q = B + \sum_f \left(\Omega_f + \mu_f n_f\right) + \sum_j \frac{1}{\pi^2}\int_0^{k_j} \sqrt{k^2 + m_j^2}\, k^4\, dk. \tag{6.16}$$

The second term in each of the above equations is the contribution from quarks, which can be inferred from Eq. (6.6) under the assumption that $T = 0$. The last integral term in each equation is the contribution from the two leptonic species and can be evaluated analytically in each case. Finally, B stands for the bag constant which is a relic of the MIT bag model for a Fermi gas of asymptotically free quarks. It is a crude way of taking into account the fact that the coupling constant, α_s, in QCD, unlike the QED coupling constant, grows with distance. In other words, the QCD vacuum cannot contain quarks and B is the energy per unit volume required to keep the vacuum out.

The values of B, α_s, and m_s, the mass of the strange quark, are not that well known. Though the value of B is uncertain, it is estimated that $B^{1/4}$ lies in the range 145–228 MeV [133]. The value of the bag constant inferred from hadronic masses is $B^{1/4} =$ 145MeV. Values of B below this value are not physically viable as they imply that the lowest stable ground state of matter is non-strange quark matter. This value is, however, not appropriate for neutron star matter that is expected to contain strange quarks in addition to up and down quarks. The corresponding minimum value for strange quark matter is $B^{1/4} = 154.5$ MeV. The values of α_s are expected to lie in the range 0.4–0.6 [133] for neutron star matter. The mass of the quark star is expected to lie in the range 80–155 MeV [133].

To determine the equation of state in the mixed phase we first determine how the quantities in one phase are related to the other. For equilibrium to exist between the two

phases the Gibbs condition must be satisfied. According to it the temperature and the pressure must be the same in both phases (we use $T = 0$). Another requirement is related to the independently conserved quantities of the system. In neutron stars the total electric charge and the total baryonic charge must be conserved. This condition implies that the electron and neutron potentials must be the same in both phases. The Gibbs condition can then be written as

$$p_B\left(\mu_n, \mu_e\right) = p_Q\left(\mu_n, \mu_e\right), \tag{6.17}$$

where p_B represents the pressure in the baryonic phase Eq. (5.11), p_Q the pressure in the quark phase Eq. (6.15), μ_n the neutron chemical potential, μ_e the electron chemical potential and temperature is assumed to be zero in both phases. The conservation laws of charge neutrality and baryon conservation in the mixed phase are satisfied globally rather than locally for each phase. If χ is the volume fraction occupied by quarks then these conditions for the mixed phase are written, respectively, as

$$(1-\chi)q_B + \chi q_Q = 0 \tag{6.18}$$

$$(1-\chi)n_B + \chi n_Q = n, \tag{6.19}$$

Here, q_B and q_Q are the charge densities of the baryon and quark phases respectively and n_B and n_Q are the baryonic number densities of the baryonic and quark phases respectively. They are defined as

$$q_B = \sum_b Q_b n_b, \tag{6.20}$$

$$q_Q = \sum_f Q_f n_f, \tag{6.21}$$

$$n_B = \sum_i n_i, \tag{6.22}$$

$$n_Q = \frac{1}{3}\sum_f n_f, \tag{6.23}$$

where, the subscripts i and f denote baryonic species i and quark species f, respectively, Q denotes the charge of a species, and n the number density. The physical implication of these global laws is that they allow the quark and the baryonic phases to have a net charge and thereby form a crystalline lattice. To solve for the equation of state we also need to express the quark chemical potentials in terms of the neutron and electron chemical potentials. These relations are obtained by recognizing that the phases being in equilibrium allows matter to be exchanged between them. The implication is that the chemical potentials of

nucleons equal the chemical potentials of their constituents:

$$\mu_n = \mu_u + 2\mu_d \tag{6.24}$$
$$\mu_p = 2\mu_u + \mu_d. \tag{6.25}$$

These relations coupled with the relationship between the chemical equations implied by the neutron β decay equation (the neutrinos are assumed to be absent and their chemical potential is therefore set to zero):

$$\mu_n = \mu_p + \mu_e, \tag{6.26}$$

give us our desired equations:

$$\begin{aligned} \mu_u &= \frac{1}{3}\mu_n - \frac{2}{3}\mu_e \\ \mu_d = \mu_s &= \frac{1}{3}\mu_n + \frac{1}{3}\mu_e. \end{aligned} \tag{6.27}$$

The system of equations to be solved, therefore, includes Eqs. (6.11), (6.12) (6.17), (6.18), (6.19), (6.27), the Euler-Lagrange equations for the baryons and the mesons, and the equations of generalized β-equilibrium in the baryonic phase. These equations are solved for the Fermi momenta of the particles and the meson states as a function of the volume fraction χ, where $\chi = 0$ identifies the lower density edge, while $\chi = 1$ the higher density edge of the mixed phase of the star. The total energy density, ϵ, is the energy density of each phase weighted by the corresponding volume fraction:

$$\epsilon = \chi\epsilon_Q + (1-\chi)\epsilon_B, \tag{6.28}$$

where ϵ_Q is the quark phase energy density while ϵ_B is the energy density associated with the baryons.

A valid equation of state is one that satisfies the latest astronomical constraints on the neutron star mass. These constraints are the same as those described in 3.1, here we briefly summarize them adding an update.

The traditional limit on the heaviest observed neutron star mass has till very recently been $1.5M_\odot$ [48] as determined from radio observations of pulsars. Nice et al. [44, 61] have, however, determined recently that the mass of PSR J0751-1807 is greater than $1.6M_\odot$ at the 95% confidence level. Another observation that has pushed the observed mass limit to an even higher value is that of Ter 5 I [43]. It has been determined by measuring the periastron advance of the star's orbit that its mass is 1.68 at the 95% confidence level, although the observation might be contaminated by the quadrupole moment rotationally induced by the companion star.

We use the Oppenheimer-Volkoff (OV) equations to determine the maximum mass star

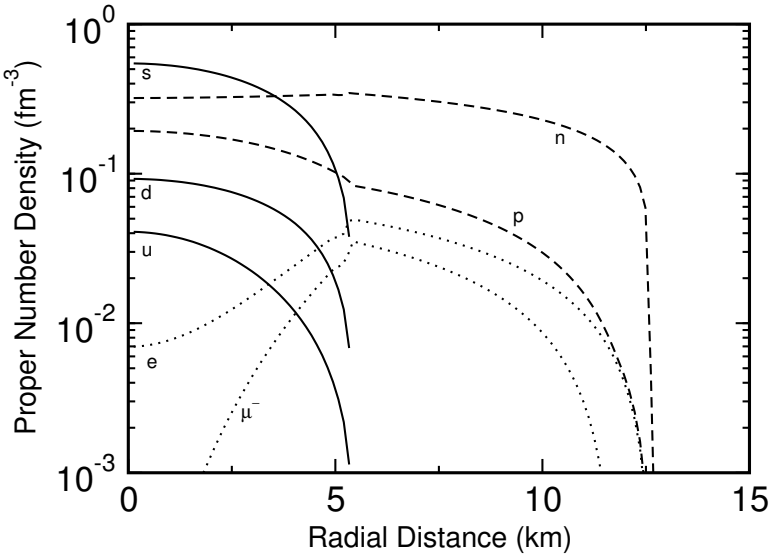

Figure 6.1: Population densities as a function of the radial distance from the center of the maximum mass star with equation of state Hy1 from Table 6.1. The solid lines represent the quarks, the dashed lines the baryons, and the dotted lines the leptons.

for each equation of state that is stable to radial oscillations. We use a form of these equations which are, for reasons of simplifying the numerics, framed in terms of the enthalpy rather than the pressure [68]. The maximum mass obtained using the OV equations is for the static case, we expect that the value for rotating stars will be higher. The neutron star Ter 5I is rotating at 104 Hz which implies an upward correction of $\sim 1\%$ to masses obtained using the OV equations. Then, any maximum mass obtained from the OV equations that exceeds $1.68 M_\odot$ less 1%, satisfies this mass constraint.

The equations of state must also satisfy the gravitational redshift measurement obtained by Cottam, Paerels, and Mendez [45] by observing the absorption spectra of EXO0748-676 during multiple burst events. They have determined the star's gravitational redshift to be 0.35, and the errors on this measurement total to less than 5% [45]. The maximum redshift corresponds to the maximum mass for any equation of state. Once the mass and radius of a star have been determined by the OV equations the corresponding redshift can be determined using

$$1 + z = \left[1 - \frac{2GM}{Rc^2}\right]^{-\frac{1}{2}}. \tag{6.29}$$

It has been observed that the star is rotating only at 45 Hz which suggests that the correction from rotation is minimal. The acceptable value of redshift obtained for the maximum OV star is then 0.35 less 5%, which is the error in the redshift measurement.

We find that the existing hybrid equations of state from Ref. [32] fall well short of both

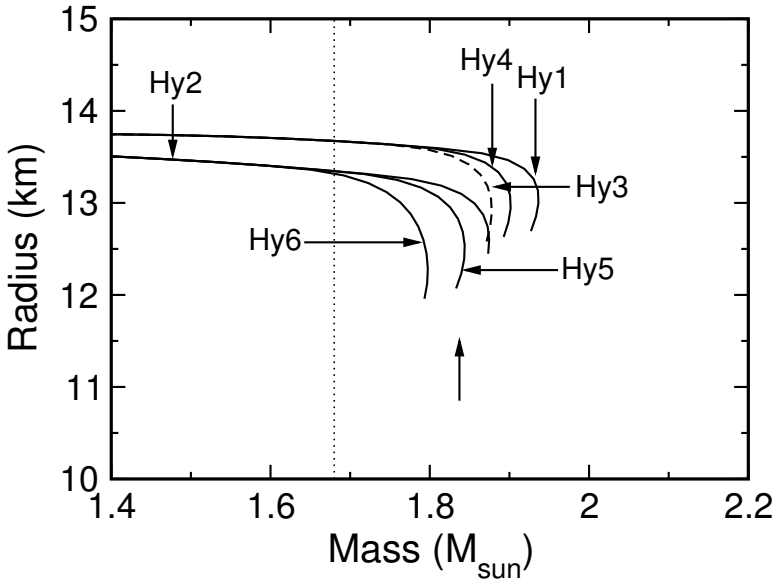

Figure 6.2: Radius-Mass curves for the hybrid equations of state given in Table 6.1.

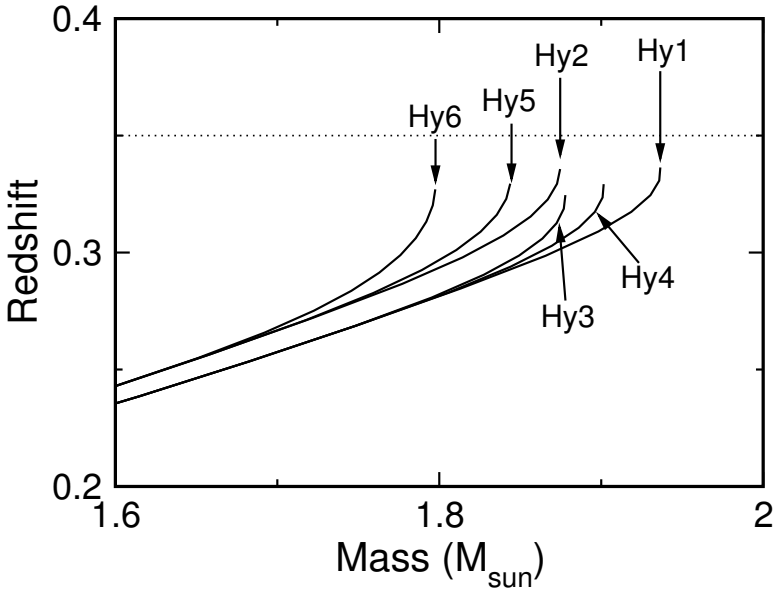

Figure 6.3: Gravitational redshift versus mass sequences for the equations of state given in Table 6.1.

the gravitational redshift and the mass limit. We therefore create a set of equations of state (given in Table 6.1) that satisfy the mass and redshift requirements by varying the most uncertain equation of state parameters: K and m^* of the hadronic equation of state, and B and α_s of the quark equation of state. The theoretically allowed ranges for the hadronic parameters, K and m^*, are well established and they are 120–300 MeV, and 0.7–0.8 m_N, respectively. The quark equation of state values are more uncertain. We consider a range of 150–180 MeV for $B^{1/4}$, 0.4–0.6 for α_s and set the mass of the strange quark to $m_s = 150$ MeV. Common to all of these equations of state are the relatively well known experimentally determined values of saturation number density (0.153 fm^{-3}), saturation binding energy (-16.3 MeV), and the coefficient of isospin asymmetry energy at saturation (32.5 MeV). We do not include hyperons as we find that the extra degrees of freedom provided by them, in almost all cases, softens the equations of state to the point where they don't satisfy the gravitational redshift constraint.

The equations of state that satisfy both are given in Table 6.1. We found that the parameter space of the equation of state is not much constrained by either the incompressibility, the bag constant or the strong coupling constant. The equations of state we created exhibit values of K in the 240-300 MeV range, $B^{1/4}$ in the 150-180 MeV range, and α_s in the 0.45–0.6 range. All the equations used the lowest possible value of the effective mass, i.e. $m^* = 0.7 m_N$.

The gravitational redshift constraint is harder to satisfy than the mass constraint. It can be seen from Fig. 6.2 that the hybrid equations of state comfortably exhibit higher masses than the $1.68 M_\odot$ limit. From Fig. 6.3 it can be seen that the redshifts of the hybrid equations of state lie in the 0.33–0.34 range–short of the redshift constraint but within the 0.5% error of the measurement. It is worth stating that even though burst events have been observed for EXO0748-676 after the publication of Ref. [45], the gravitational redshift lines have not been observed again [134]. Whether this casts doubt on the original set of observations is a question that remains so far unresolved.

Table 6.1: Parameters for a few mixed equations of state which satisfy the astronomical constraints.

Name	K (MeV)	m^*/m	$B^{1/4}$(MeV)	α_s
Hy1	300	0.70	180	0.60
Hy2	240	0.70	180	0.60
Hy3	300	0.70	160	0.60
Hy4	300	0.70	180	0.45
Hy5	240	0.70	180	0.45
Hy6	240	0.70	150	0.6

6.3 Microstructure

Once the mixed phase density is reached, the additional degree of freedom provided by quark matter allows a decrease in the total isospin asymmetry energy. The neutrons in the hadronic phase can now be converted to protons, the positive charge being balanced by the negatively charged quark phase. The opposing charges on the two phases cause the formation of a crystalline lattice in which the rarer phase occupies lattice sites in the background phase. The shape of the rare phase at the lattice sites evolves with density. At the lowest densities in the mixed phase quark matter occupies the lattice sites and is spherical in shape (drops). As the quark content increases the shape is first modified to rods as the drops merge, and then to slabs as the rods merge to form "lasagne"-like sheets. Further increase in the quark content causes the hadronic phase to become the rarer phase. Hadronic matter now occupies the lattice sites shaped like slabs buried in a quark matter background. The shape of the hadronic matter now evolves first to rods and finally to drops before the neutron star becomes exclusively quark matter. The evolution of the shape of the immersed phase with density is very similar to the better known "nuclear pasta" structure of the crust [135].

The size and shape of the rarer phase depends on the interplay between the Coulombic interaction and the surface interface energy. Coulombic interaction tends to break up the rarer phase into small units while surface interface energy tends to cause aggregation. The analysis can be performed by considering a single Wigner-Seitz cell. Each cell is associated with a lattice point where the rarer phase is located, and surrounded by oppositely charged dominant phase matter that makes the cell neutral. To determine as a function of χ the shape of the rarer phase we calculate the sum of the Coulombic and surface energies (per unit volume) for each of the three shapes we consider. The shape with the lowest energy sum is the shape taken. The sum of the energies is given by [135, 136]

$$\epsilon_C + \epsilon_S = 6\pi x \left(\frac{\{\sigma d\,[q_H(\chi) - q_Q(\chi)]\,e\}^2\, f_d(x)}{16\pi^2} \right)^{1/3}, \tag{6.30}$$

Table 6.2: The lowest mass star which exhibits a mixed phase along with the maximum possible mass for each equation of state.

Name	Mass ($M_\odot$)	Max. Mass ($M_\odot$)
Hy1	1.86	1.94
Hy2	1.79	1.88
Hy3	1.78	1.88
Hy4	1.75	1.90
Hy5	1.67	1.84
Hy6	1.63	1.80

where ϵ_C and ϵ_S are the charge and surface energy densities, respectively, and d tracks the shape:

$$d = \begin{cases} 1, & \text{slab} \\ 2, & \text{rod} \\ 3, & \text{drop} \end{cases} . \tag{6.31}$$

The parameter x is defined as

$$x = \begin{cases} \chi, & \text{(background phase is hadrons)} \\ 1-\chi, & \text{(background phase is quarks)} \end{cases} , \tag{6.32}$$

and the function $f_d(x)$ as

$$f_d(x) = \frac{1}{d+2}\left[\frac{1}{d-2}(2 - dx^{1-2/d}) + x\right]. \tag{6.33}$$

For $d = 2$, the limit of Eq.(6.33) is well defined and can be calculated using

$$\lim_{d\to 2}\left[\frac{2 - dx^{1-2/d}}{d-2}\right] = -(1 + \ln x). \tag{6.34}$$

The parameter σ is the surface tension, e is the electronic charge in Gaussian units, and $q_H(\chi)$ and $q_Q(\chi)$ are the charge densities of the hadronic and quark phases, respectively. The electronic charge e in Gaussian units is given by the following relation:

$$e_{Gauss} = \sqrt{\alpha}, \tag{6.35}$$

where α is the fine structure constant. The half dimension of the rarer phase (radius of droplets, half-thickness of rods and slabs) can be calculated by minimizing the sum of the Coulombic and surface energy. The relation that results from the minimization is

$$\epsilon_S = 2\epsilon_C, \tag{6.36}$$

which gives for the radius the result

$$r = \left(\frac{\sigma d}{4\pi\left[q_H(\chi) - q_Q(\chi)\right]^2 e^2 f_d(x)}\right)^{1/3}, \quad \text{d=1, 2, 3.} \tag{6.37}$$

The spacing between the lattice points is $S = 2R$ where R is related to the radius by the following relation:

$$x = (r/R)^d. \tag{6.38}$$

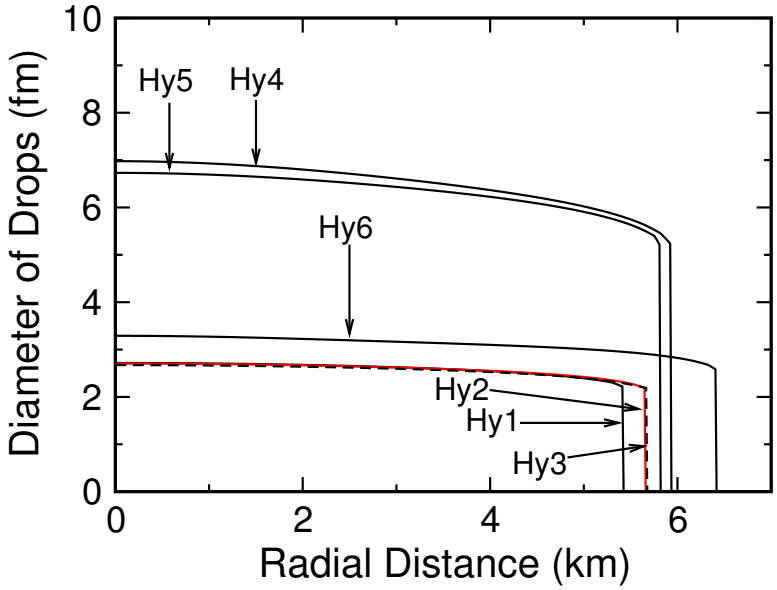

Figure 6.4: The size of the spherical quark drops as a function of the radial coordinate in the mixed cores of maximum mass hybrid stars for equations of state enumerated in Table 6.1.

The value of the surface tension, σ, is not well known for quark matter. It is estimated by Heiselberg et al. [137] to be in the range 10-100 MeV fm^{-2}. Glendenning [32] recommends picking a value of surface tension that ensures that the sum of the surface and energy density is smaller than 1% of the higher of the hadronic or quark energy density. To minimize this sum we use the lowest allowed value of 10 MeV fm^{-2} which makes it about a 7% correction to the hadronic or quark energy density. The important point is that it is still a small correction, and thus the simplification of ignoring the effect of crystallization on the overall equation of state is still well justified.

The constraint imposed by the gravitational redshift observation has consequences on the size and spacing of the embedded phase lattice points. We find that the cores of the maximum mass stars for our equations of state are not dense enough to be purely quark matter. In fact, in the centers of these stars the ratio of quark matter to hadronic matter by volume is only $\chi \sim 0.1$. The mixed phase cores of these stars are therefore populated only by spherical quark droplets in the baryonic background, other shapes do not occur. In Fig. 6.4 we plot the diameter of the droplets for the maximum mass stars for each of the equation of state. It can be seen that the droplet diameters are in the 2.5–7.0 fm range. It can be seen that the mixed phase cores of the star are in the 5.5-6.5 km range. The spacing as a function of the stellar radial coordinate for the maximum mass stars is given in Fig. 6.5. The spacing is typically in the 6–13 fm range.

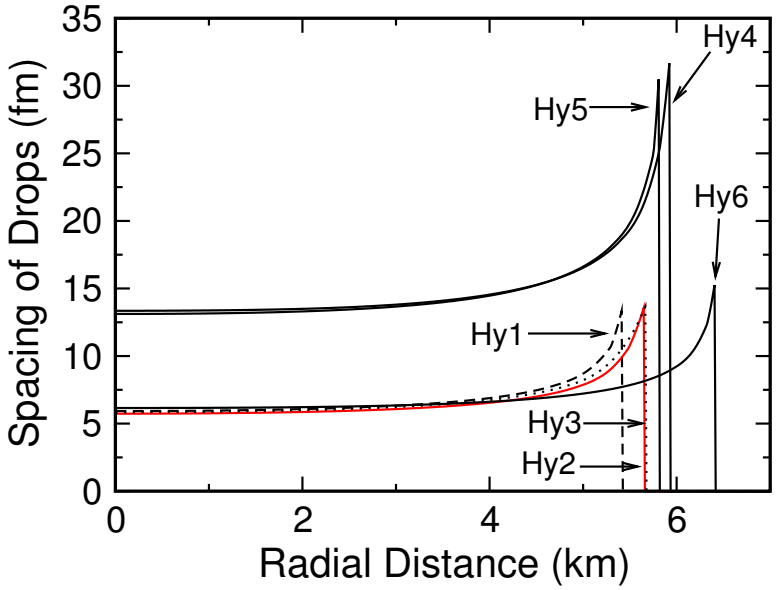

Figure 6.5: The spacing between the spherical quark drops as a function of the radial coordinate in the mixed cores of maximum mass hybrid stars for equations of state enumerated in Table 6.1.

6.4 Shear modulus

To calculate the size of the mountain caused by the formation of a lattice in the mixed phase part of the star we need to be able to calculate the shear modulus of the lattice in terms of D and S. We use the calculation by Fuchs [138] who calculates the shear modulus for a bcc lattice of metal ions embedded in a sea of electrons. In that calculation he assumes that the metallic ions are point-like particles to calculate the electrostatic energy of the lattice. He does not include the effect of charge screening. The expression he obtains for the shear modulus is

$$\mu = 0.3711 q_B^2 n_B / a, \tag{6.39}$$

where q_B is the charge in esu of the embedded phase at a lattice point, n_B its number density, and a is the lattice constant. If we use the definitions of S and D above, and the relation between S, the diameter of the Wigner Seitz cell, and the lattice constant, $S = (\sqrt{3}/2)a$, we obtain the following relation:

$$\mu = 0.075\, q^2 D^6 / S^4. \tag{6.40}$$

Here, q is the charge density of the embedded phase in esu units. In Fig. 6.6 we plot the shear modulus as a function of the radial distance for the maximum mass Hy1 EOS star. These values are of order 10^4 times the values for normal neutron star crusts, largely because

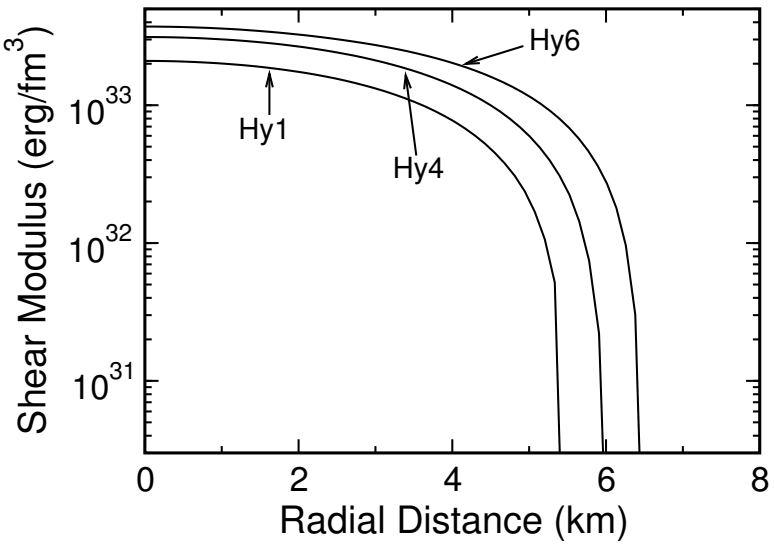

Figure 6.6: The shear modulus as a function of the radial distance for the maximum mass stars for a few equations of state. The effect of charge screening is not included here.

of the higher density. Overall, the shear modulus we obtain here before screening is higher than estimated by Owen [31] because the equations of state are generally stiffer than those he considered from Ref. [32], leading to higher densities and shorter length scales.

The effect of charge screening is worth investigating as high charge screening would make the two phases effectively neutral thereby preventing the formation of a lattice. The amount of charge screening is measured in terms of the Debye length—the smaller the Debye length the greater the charge screening. We give the outline of a derivation of the Debye length for a simplified version of the problem from which this becomes evident. Making the assumption that the blob is a point charge we can write the effect of charge screening on the unperturbed Poisson equation as

$$\nabla^2\Phi = -4\pi\left[Q\delta^3(r) + \sum_i Q_i\bar{n}_i(r)\right]. \tag{6.41}$$

Here Q is the unperturbed charge of the blob, Q_i is the charge associated with each species and $\bar{n}_i$ is the number density of each particle species in the final configuration. We assume that the electrostatic energy is a small perturbation on the chemical potential so that we can write the number densities as

$$\bar{n}_i = n_i + Q_i\Phi(\delta\bar{n}_i/\delta\mu_i), \tag{6.42}$$

where n_i is the unperturbed number density. Then, using $\sum_i Q_i n_i = 0$ and the above

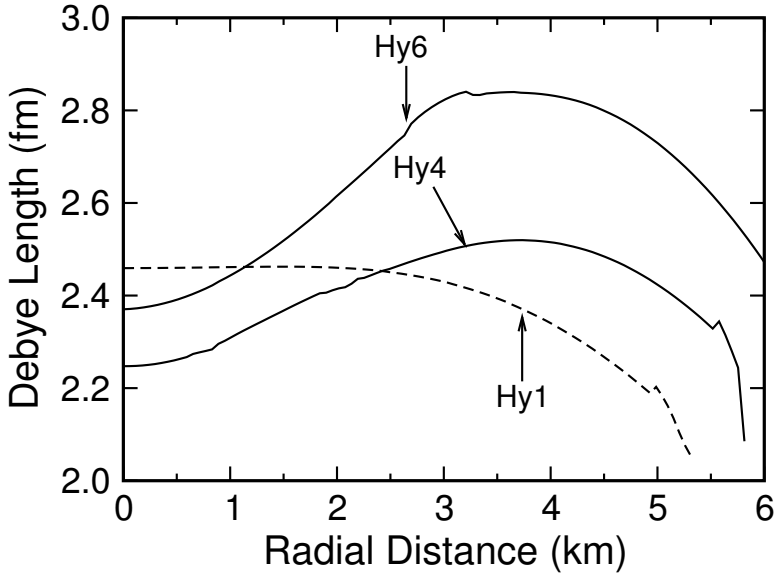

Figure 6.7: The Debye length as a function of the radial distance for the maximum mass stars for a few equations of state.

equation, we can rewrite Eq. (6.41) as

$$\left[\nabla^2 - 4\pi \sum_i Q_i^2 \left(\frac{\delta \bar{n}_i}{\delta \mu_i}\right)\right] \Phi = -4\pi Q \delta^3(r). \tag{6.43}$$

The solution to this equation is the Yukawa potential,

$$\Phi = \frac{Q}{r} \exp^{-r/\lambda}, \tag{6.44}$$

where λ, the Debye length is given by

$$\lambda = \left[4\pi \sum_i Q_i^2 \left(\frac{\partial n_i}{\partial \mu_i}\right)\right]^{-1/2} \tag{6.45}$$

We can see that if λ is too small then the electrostatic potential falls off very fast, thereby, implying large charge screening. We compare the length scales of the blobs with the Debye lengths obtained for the different equations of state we use. We find that the Debye length is typically comparable to the radius of the blobs, indicating that our simple approximation is on the edge of losing relevance. The shear modulus is approximately the second derivative of the potential energy. Screening then, for our typical values of $\lambda = 2.5$ fm (see Fig. 6.7), reduces the shear modulus by a factor of e^5 or $\sim$ 150 for the higher values of spacing $S = \sim$ 13 fm, and e^2 or $\sim$ 7 for the smaller values. Using lower values in the allowed range

for σ, the surface tension, can lower the spacing by approximately a factor of 2. In that case the decrease in the shear modulus for the large and small spacing is, respectively, e^3 or ~ 20 and e^1 or ~ 2.7. Despite the effect of charge screening the values of shear modulus for hybrid stars still remain much higher than the corresponding values for normal neutron stars.

6.5 Maximum quadrupoles

Table 6.3: The quadrupole moments over breaking strain for each of the hybrid equations of state. The effect of charge screening is not included. Each star is at the maximum stable mass.

Name	Q_{22}/σ_{max} (10^{43}erg cm^2)
Hy1	1.26
Hy2	1.53
Hy3	2.05
Hy4	2.31
Hy5	2.08
Hy6	3.36

The average amplitude strain of gravitational radiation from a neutron star is given by [139]

$$h_0 = \frac{16\pi^2 G}{c^4}\frac{Q_{22}f^2}{D}, \tag{6.46}$$

where Q_{22} is the quadrupole moment of the star, f is the frequency of the star. The ellipticity, ϵ, of the star is given by

$$\epsilon = \frac{I_{xx} - I_{yy}}{I_{zz}}, \tag{6.47}$$

where the axis of rotation is the z axis and I_{ab} is the moment of inertia tensor. The ellipticity

Table 6.4: The quadrupole moments over breaking strain for each of the hybrid equations of state. The effect of charge screening is included. Each star is at its maximum stable mass.

Name	Q_{22}/σ_{max} (10^{42}erg cm^2)
Hy1	0.80
Hy2	1.19
Hy3	1.38
Hy4	1.22
Hy5	1.32
Hy6	2.81

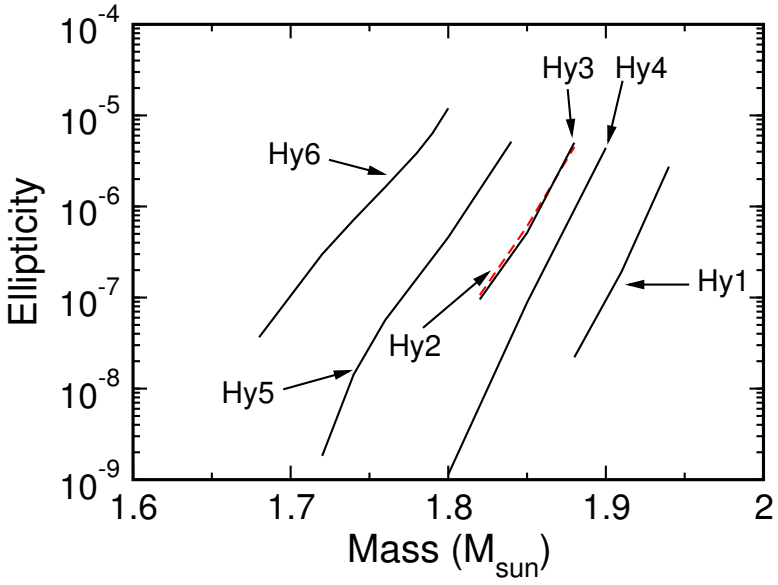

Figure 6.8: The ellipticity as a function of mass for all the hybrid equations of state. We use a value of $\sigma_{max} = 10^{-2}$. The dashed line represents the Hy2 curve which is very similar to the Hy3 curve. The effect of self-gravity is not included here.

is related to the quadrupole moment by the relation

$$\epsilon = \sqrt{8\pi/15} Q_{22}/I_{zz}. \tag{6.48}$$

The quadrupole moment for arbitrary equations of state is given by

$$\frac{Q_{22,\max}}{\sigma_{\max}} = \sqrt{\frac{32\pi}{15}} \int dr \frac{\mu r^3}{g} \left(48 - 14U + U^2 - \frac{dU}{d\ln r}\right), \tag{6.49}$$

where g is the local acceleration due to gravity, and $U = 2 + d\ln g/d\ln r$. Since the density in the core changes very gradually we can write $g = GMr/R^3$ which gives us a value of $U = 3$. We tabulate the quadrupole moment (over the breaking strain) for our equations of state without the effect of charge screening in Table 6.4. The breaking strain is not very well known. The highest breaking strain obtained from Earthly metals is 10^{-2}, but some estimate that this could be lower by 10^2–10^3 [29].

The moment of inertia of the star is given to a few percent approximation by [140]

$$\begin{aligned} I_{zz} &= 9.2 \times 10^{44} \text{ g cm}^2 \left(\frac{M}{1.4\ M_\odot}\right) \left(\frac{R}{10 \text{ km}}\right)^2 \\ &\quad \times \left[1 + 0.7 \left(\frac{M}{1.4\ M_\odot}\right) \left(\frac{10 \text{ km}}{R}\right)\right], \end{aligned} \tag{6.50}$$

regardless of the equation of state. This allows us to convert the quadrupole to a dimensionless ellipticity using Eq. (6.48).

The above figures use the equations of hydrostatic equilibrium in the Cowling approximation, i.e. not including the perturbation of the gravitational potential. Early estimates from Newtonian gravity [29] suggest that inclusion of the perturbation could multiply these numbers by up to a factor 3. Haskell, Jones, and Andersson [141] essentially rediscovered this factor in their attempt to drop the Cowling approximation, although they claim more novelty.

6.6 Conclusion

From the results in Fig. 6.8, which do not include the factor of 3 from self-gravity, we see that ellipticities up to about 3×10^{-5} or three times the results of Owen [31] are possible. However, this occurs only for stars that are within about 0.1 $M_{\odot}$ of their maximum stable mass. Both of these are primarily due to the fact that here we use a different set of equations of state within the same framework. The equations of state used here are stiffer overall because they are made to satisfy new observational constraints on masses and redshift, resulting in higher densities and smaller lengthscales of the crystalline structure. The implications for LIGO are mixed. LIGO can now consider that somewhat higher ellipticities are possible in the robust hybrid star model than previously considered [31], and thus observational upper limits can be claimed to be interesting somewhat sooner. However the likelihood of actually detecting a signal is decreased due to the small mass range necessary.

In the near future we would like to more carefully address the issue of charge screening. Also, we would like to repeat this analysis for kaon condensate stars, which should have similarly large maximum ellipticities and be of similar interest to LIGO [31].

6.7 Discussion: Implications for LIGO

It is planned that LIGO will go through two intermediate phases in its evolution before it achieves its most technologically advanced form as "advanced LIGO". Currently in its first phase, that of initial LIGO, it is collecting data in its fifth scientific run (S5). The goal of S5 is to achieve a year of triple coincident data between the two LIGO detectors at Hanford and the one in Louisiana, which is projected to be achieved by October 2007. Once S5 is concluded LIGO will be upgraded to "enhanced LIGO", which will be twice as sensitive as initial LIGO for frequencies greater than 100 Hz. Work on the final set of upgrades for "advanced LIGO" will begin around 2015 [142].

There are 4 types of neutron star related searches conducted by LIGO. The first type

is directed towards known pulsars whose frequencies, f, frequency time-derivatives, $\dot{f}$, and distances from Earth, D, are known [1] from photon astronomy. The second type is directed towards non-accreting non-pulsating neutron stars whose position in the sky is known. The third type is an all-sky search which looks for neutron stars which have not been discovered yet. Finally, the fourth type of search targets neutron stars in accreting systems that may or may not be pulsating. Our results for the maximum ellipticities obtainable from hybrid stars have implications for the first two types of searches, as explained below.

The gravitational wave signal from a pulsar is likely to be detectable when the spin-down limit on its strain amplitude, h_{sd}, is higher than LIGO's sensitivity curve. How small an h LIGO is sensitive to depends on the parameter space to be searched over and the integration time of the search. For pulsars whose parameters f, $\dot{f}$, and D are known, the sensitivity of LIGO is the highest as data analysis is required to search only over a small parameter space. In Fig. 6.9 we plot the corresponding sensitivity curve for LIGO which is obtained for S5 triple coincidence data for an integration time of one year. It plots the 95% credible lower-limit strain amplitude [2] LIGO will be capable of detecting at the end of S5 as a function of the frequency of the gravitational wave signal. The spin-down limit on h for a given pulsar is calculated by assuming that its loss of rotational energy is caused completely by gravitational radiation. The upper bound on the amplitude strain of a pulsar can be calculated using [143]

$$h_{sd} = 8.1 \times 10^{-25} \left(\frac{1 \text{ kpc}}{D}\right) \left(\frac{-\dot{f}}{10^{-10}\text{Hz/s}} \frac{100\text{Hz}}{f}\right)^{1/2} \left(\frac{I}{10^{38} \text{ kg m}^2}\right)^{1/2}, \tag{6.51}$$

where *kpc* denotes 1 kilo parsec. It can be seen from Fig. 6.9 that by the end of S5 LIGO will beat the spindown limit on the Crab pulsar. "Enhanced LIGO", which will be ~ 2 times more sensitive than initial LIGO at frequencies greater than 100 Hz, will be able to beat the spindown limits on two additional pulsars: PSR J0537-6910 and PSR J1952+3252 (from Ref. [27] which omits PSR J0537-6910 due to an arithmetic error).

The connection between known pulsars and our results can be made by converting the spin down limits on h to spin down limits on the ellipticities by using Eqs. (6.46) and (6.48). The spindown ellipticities of the Crab, PSR J0537-6910, and PSR J1952+3252 are, respectively, 7.4×10^{-4}, 8.8×10^{-5}, and 1.1×10^{-4} (although the uncertainties in the moment of inertia and distance could result in limits higher by a factor of ~ 2 [144]). That PSR J0537-6910, and PSR J1952+3252 lie very close to the sensitivity curve is indicative of the fact that lower values of ellipticty would not be detectable by "initial" or "enhanced LIGO".

[1] D for a pulsar is obtained from measurements of the dispersion of its radio pulses. It is uncertain in most cases by up to 20%.

[2] the 95% confidence limit is $11\sqrt{S_h(f)/T}$ where T is the observation time and S_h is the sum of the interferometers' power spectral noise densities.

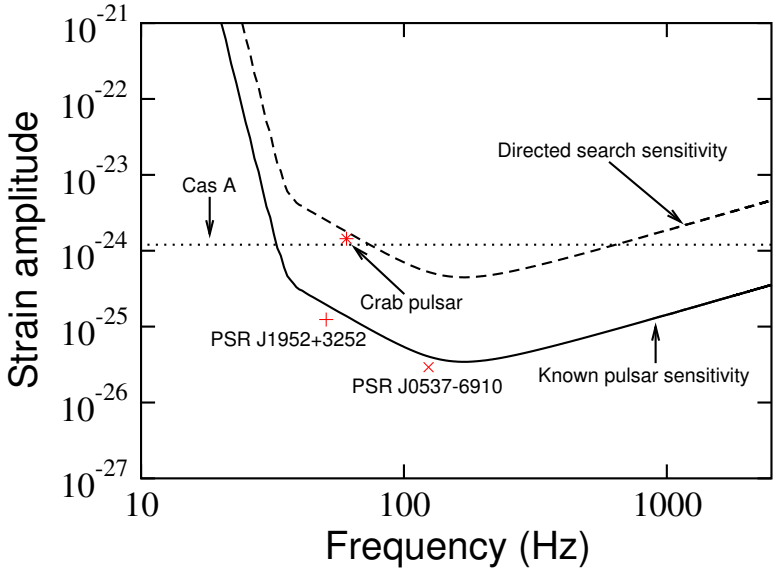

Figure 6.9: LIGO's sensitivity curves for the known-pulsar search (solid line) and directed neutron star search (dashed line): the lower-limit amplitude strain detectable by LIGO as a function of the frequency of the gravitational wave signal. The dotted line represents h_{sd} for Cas A whose frequency is not known, while the h_{sd} for the Crab, PSR J1952+3252, and PSR J0537-6910 pulsars are also indicated.

Since these values are higher than 3×10^{-5}, the maximum ellipticities possible for hybrid stars, "initial" and "enhanced LIGO" will not be able to detect hybrid stars. Advanced LIGO which will be more sensitive by a factor of ~ 10 will be able to probe the hybrid star regime better.

Non-pulsating non-accreting stars include compact objects in supernova remnants and several x-ray and gamma-ray sources not associated with any remnants. The distance to these objects is known but the frequencies and the frequency time-derivatives are not. The search for signals from these sources (directed search) is more computationally intensive than the known-pulsar search as the parameter space to be searched is larger–it would include atleast f, $\dot{f}$ and $\ddot{f}$. The LIGO sensitivity curve for this case, also shown in Fig. 6.9, is a factor of ~ 13 higher than that for the known pulsar search. The search over extra parameters contributes a factor of 3 to the increase, while the remaining factor is a result of high computational costs which limit the search to ~ 18 days at present. Under the assumption that the neutron star has spun down significantly since its birth and this spin down is caused mostly by gravitational radiation we can calculate, in this case too, a "spindown" limit by rewriting Eq. (6.51) as

$$h_{sd} = 2.3 \times 10^{-24} \left(\frac{1 \text{ kpc}}{D}\right) \left(\frac{10^3 \text{ yr}}{A}\right)^{1/2} \left(\frac{I}{10^{38} \text{ kg m}^2}\right)^{1/2}, \tag{6.52}$$

where, A is the age of the star. Initial LIGO can beat this upper limit for several objects including the central compact object in the supernova remnant Cas A which being only 327 years old [145] is the youngest of these.

For non-pulsating non-accreting neutron stars we can again use Eqs. (6.46) and (6.48) to determine the spindown limit on ellipticity as an inverse function of the squared spin frequency of the star. For Cas A which has a spindown limit on h of 1.2×10^{-24} only values of frequency higher than 180 Hz would yield values of ellipticity smaller than the maximum hybrid star value of 3×10^{-5}. In other words, if Cas A is a hybrid star then it would be detectable by "initial LIGO" only if it was spinning in the frequency range 180–611 Hz where the upper value marks the upper frequency edge of the sensitivity curve for directed searches.

References

[1] C. W. Misner, K. S. Thorne, and J. A. Wheeler. *Gravitation.* San Francisco 1973, 1279p.

[2] (Ed.) Hawking, S. W. and (Ed.) Israel, W. *Three Hundred Years of Gravitation.* Cambridge, UK: Univ. Pr. (1987) 684 p.

[3] Clifford M. Will. The confrontation between general relativity and experiment. *Living Rev. Rel.*, 4:4, 2001. gr-qc/0103036.

[4] A. Einstein. Näherungsweise integration der feldgleichungen der gravitation. *Sitzungsberichte der Königlich Preußischen Akademie der Wissenschaften (Berlin), Seite 688-696.*, page 688, 1916.

[5] A. Einstein. Über gravitationswellen. *Sitzungsberichte der Königlich Preußischen Akademie der Wissenschaften (Berlin), Seite 154-167.*, page 154, 1918.

[6] H. Weyl. *Space-Time-Matter.* Methuen, London, 1922.

[7] Eddington. *The mathematical theory of relativity.* Cambridge University Press, 2nd edition, 1924.

[8] L. D. Landau, E. M. Lifshitz, (Ed.) Schopf, H. G., and (Ed.) Ziesche, P. *Textbook on Theoretical Physics, Vol. 2: Classical Field Theory. (In German).* Akademie-Verl., Berlin (1987) 481 p.

[9] Richard A. Isaacson. Gravitational radiation in the limit of high frequency. I. The linear approximation and geometrical optics. *Phys. Rev.*, 166(5):1263, Feb 1968.

[10] Richard A. Isaacson. Gravitational radiation in the Limit of high frequency. II. Nonlinear terms and the effective stress tensor. *Phys. Rev.*, 166(5):1272, Feb 1968.

[11] R. A. Hulse and J. H. Taylor. Discovery of a pulsar in a binary system. *Astrophys. J.*, 195:L51, 1975.

[12] Joseph H. Taylor and J. M. Weisberg. Further experimental tests of relativistic gravity using the binary pulsar PSR 1913+16. *Astrophys. J.*, 345:434, 1989.

[13] Alex Abramovici et al. Ligo: The laser interferometer gravitational wave observatory. *Science*, 256:325, 1992.

[14] A. Lazzarini. Document G060293-00-Z: Strain sensitivity for the LIGO 4km interferometers, performance for S5 - June 2006. http://www.ligo.caltech.edu/docs/G/G060293-00.

[15] Curt Cutler and Kip S. Thorne. An overview of gravitational-wave sources. 2002. gr-qc/0204090.

[16] Jason W. T. Hessels et al. A radio pulsar spinning at 716 Hz. *Science*, 311:1901, 2006. astro-ph/0601337.

[17] P. Kaaret et al. Discovery of 1122 Hz x-ray burst oscillations from the neutron-star x-ray transient XTE J1739-285. *Astrophys. J.*, 657:L97, 2006. astro-ph/0611716.

[18] C. Kouveliotou et al. An x-ray pulsar with a superstrong magnetic field in the soft gamma-ray repeater SGR 1806-20. *Nature*, 393:235, 1998.

[19] L. D. Landau. K teorii zvezd (1932) (on the theory of stars (1932)). In *Sobranie trudov T. 1*, page 69. Nauka (Moscow), 1969.

[20] W. Baade and F. Zwicky. Remarks on super-novae and cosmic rays. *Phys. Rev.*, 46(1):76, Jul 1934.

[21] J. R. Oppenheimer and G. M. Volkoff. On massive neutron cores. *Phys. Rev.*, 55:374, 1939.

[22] A. Hewish, S. J. Bell, J. D. H Pilkington, P. F. Scott, and R. A. Collins. Observation of a rapidly pulsating radio source. *Nature*, 217:709, 1968.

[23] T. Gold. Rotating neutron stars as the origin of the pulsating radio sources. *Nature*, 218:731, 1968.

[24] P B Jones. The alignment of the crab pulsar magnetic axis. *Astrophys. Space Sci.*, 33:215, 1975.

[25] Curt Cutler. Gravitational waves from neutron stars with large toroidal B-fields. *Phys. Rev.*, D66:084025, 2002. gr-qc/0206051.

[26] Andrew Melatos and D. J. B. Payne. Gravitational radiation from an accreting millisecond pulsar with a magnetically confined mountain. *Astrophys. J.*, 623:1044, 2005. astro-ph/0503287.

[27] B. J. Owen. Detectability of periodic gravitational waves by initial interferometers. *Class. Quant. Grav.*, 23:S1, 2006.

[28] Lars Bildsten. Gravitational radiation and rotation of accreting neutron stars. *Astrophys. J.*, 501:L89, 1998. astro-ph/9804325.

[29] Greg Ushomirsky, Curt Cutler, and Lars Bildsten. Deformations of accreting neutron star crusts and gravitational wave emission. *Mon. Not. Roy. Astron. Soc.*, 319:902, 2000.

[30] R. X. Xu. Solid quark matter? *Astrophys. J.*, 596:L59, 2003.

[31] Benjamin J. Owen. Maximum elastic deformations of compact stars with exotic equations of state. *Phys. Rev. Lett.*, 95:211101, 2005. astro-ph/0503399.

[32] Norman K. Glendenning. *Compact Stars: Nuclear Physics, Particle Physics, and General Relativity.* Springer, New York, 2nd edition, 2000.

[33] Norman K. Glendenning. First order phase transitions with more than one conserved charge: Consequences for neutron stars. *Phys. Rev.*, D46:1274, 1992.

[34] Norman K. Glendenning and Jürgen Schaffner-Bielich. Kaon condensation and dynamical nucleons in neutron stars. *Phys. Rev. Lett.*, 81:4564, 1998. astro-ph/9810284.

[35] M. H. van Kerkwijk et al. Spectroscopy of HD 77581 and the mass of Vela X-1. *Astron. Astrophys.*, 303:483, 1995. astro-ph/9505070.

[36] Nils Andersson, Kostas D. Kokkotas, and Nikolaos Stergioulas. On the relevance of the r-mode instability for accreting neutron stars and white dwarfs. *Astrophys. J.*, 516:307, 1999. astro-ph/9806089.

[37] S. Chandrasekhar. Solutions of two problems in the theory of gravitational radiation. *Phys. Rev. Lett.*, 24(11):611, Mar 1970.

[38] J. L. Friedman and B. F. Schutz. Secular instability of rotating newtonian stars. *Astrophys. J.*, 222:281, 1978.

[39] R. V. Wagoner. Gravitational radiation from accreting neutron stars. *Astrophys. J.*, 278:345, 1984.

[40] A. Akmal, V. R. Pandharipande, and D. G. Ravenhall. The equation of state for nucleon matter and neutron star structure. *Phys. Rev.*, C58:1804, 1998. nucl-th/9804027.

[41] Madappa Prakash et al. Composition and structure of protoneutron stars. *Phys. Rept.*, 280:1–77, 1997. nucl-th/9603042.

[42] Shmuel Balberg and Nir Barnea. S-wave pairing of lambda hyperons in dense matter. *Phys. Rev.*, C57:409, 1998. nucl-th/9709013.

[43] Scott M. Ransom et al. Twenty-one millisecond pulsars in Terzan 5 using the green bank telescope. *Science*, 307:892, 2005. astro-ph/0501230.

[44] David J. Nice et al. A 2.1 solar mass pulsar measured by relativistic orbital decay. *Astrophys. J.*, 634:1242, 2005.

[45] J. Cottam, F. Paerels, and M. Mendez. Gravitationally redshifted absorption lines in the x-ray burst spectra of a neutron star. *Nature*, 420:51, 2002. astro-ph/0211126.

[46] Benjamin D. Lackey, Mohit Nayyar, and Benjamin J. Owen. Observational constraints on hyperons in neutron stars. *Phys. Rev.*, D73:024021, 2006. astro-ph/0507312.

[47] Mohit Nayyar and Benjamin J. Owen. R-modes of accreting hyperon stars as persistent sources of gravitational waves. *Phys. Rev.*, D73:084001, 2006. astro-ph/0512041.

[48] S. E. Thorsett and Deepto Chakrabarty. Neutron star mass measurements. I. Radio pulsars. *Astrophys. J.*, 512:288, 1999. astro-ph/9803260.

[49] Paul C. Joss and Saul A. Rappaport. Neutron stars in interacting binary systems. *Ann. Rev. Astron. and Astrophys.*, 22:537, 1984. and references therein.

[50] J. M. Lattimer and M. Prakash. Neutron star structure and the equation of state. *Astrophys. J.*, 550:426, 2001. astro-ph/0002232.

[51] George G. Pavlov and Victor G. Bezchastnov. Once-ionized helium in superstrong magnetic fields. *Astrophys. J.*, 635:L61, 2005. astro-ph/0505464.

[52] K. Sumiyoshi, K. Oyamatsu, and H. Toki. Neutron star profiles in the relativistic Bruckner-Hartree-Fock theory. *Nucl. Phys.*, A595:327, 1995.

[53] N. K. Glendenning. Neutron stars are giant hypernuclei? *Astrophys. J.*, 293:470, 1985.

[54] N. K. Glendenning and S. A. Moszkowski. Reconciliation of neutron star masses and binding of the lambda in hypernuclei. *Phys. Rev. Lett.*, 67:2414, 1991.

[55] Dima G. Yakovlev and C. J. Pethick. Neutron star cooling. *Ann. Rev. Astron. Astrophys.*, 42:169, 2004. astro-ph/0402143.

[56] Lee Lindblom and Benjamin J. Owen. Effect of hyperon bulk viscosity on neutron-star r-modes. *Phys. Rev.*, D65:063006, 2002. astro-ph/0110558.

[57] P. Haensel, K. P. Levenfish, and D. G. Yakovlev. Bulk viscosity in superfluid neutron star cores. III. Effects of Σ^- hyperons. *Astron. Astrophys.*, 381:1080, 2002. astro-ph/0110575.

[58] Robert V. Wagoner. Conditions for steady gravitational radiation from accreting neutron stars. *Astrophys. J.*, 578:L63, 2002. astro-ph/0207589.

[59] O. Barziv, L. Kaper, M. H. van Kerkwijk, J. H. Telting, and J. van Paradijs. The mass of the neutron star in Vela X-1. *Astron. Astrophys.*, 377:925, 2001. astro-ph/0108237.

[60] H. Quaintrell et al. The mass of the neutron star in Vela X-1 and tidally induced non-radial oscillations in GP Vel. *Astron. Astrophys.*, 401:313, 2003. astro-ph/0301243.

[61] David J. Nice, Eric M. Splaver, and Ingrid H. Stairs. Heavy neutron stars? A status report on Arecibo timing of four pulsar-white dwarf systems. 2003. astro-ph/0311296.

[62] David J. Nice, Eric M. Splaver, and Ingrid H. Stairs. Arecibo measurements of pulsar–white dwarf binaries: Evidence for heavy neutron stars. 2004. astro-ph/0411207.

[63] Sudip Bhattacharyya, M. Coleman Miller, and Frederick K. Lamb. The shapes of atomic lines from the surfaces of weakly magnetic rotating neutron stars and their implications. *Astrophys. J.*, 644:1085–1089, 2006.

[64] Gordon Baym, Christopher Pethick, and Peter Sutherland. The ground state of matter at high densities: Equation of state and stellar models. *Astrophys. J.*, 170:299, 1971.

[65] Shmuel Balberg, Itamar Lichtenstadt, and Gregory B. Cook. Roles of hyperons in neutron stars. *Astrophys. J. Supp.*, 121:515, 1998. astro-ph/9810361.

[66] S. C. Lundgren, A. F. Zepka, and J. M. Cordes. A millisecond pulsar in a 6 hour orbit: PSR J0751+1807. *Astrophys. J.*, 453:419, 1995.

[67] Gregory B. Cook, Stuart L. Shapiro, and Saul A. Teukolsky. Rapidly rotating neutron stars in general relativity: Realistic equations of state. *Astrophys. J.*, 424:823, 1994.

[68] Lee Lindblom. Determining the nuclear equation of state from neutron-star masses and radii. *Astrophys. J.*, 398:569, 1992.

[69] Adam R. Villarreal and Tod E. Strohmayer. Discovery of the neutron star spin frequency in EXO 0748-676. *Astrophys. J.*, 614:L121, 2004. astro-ph/0409384.

[70] Andrea Tiengo et al. Discovery of a redshifted x-ray emission line in the symbiotic neutron star binary 4U 1700+24. *Astron. Astrophys.*, 441:283, 2005. astro-ph/0506590.

[71] D. E. Groom et al. Review of particle physics. *Eur. Phys. J.*, C15:1–878, 2000.

[72] Nikolaos Stergioulas. Rotating stars in relativity. *Living Rev. Rel.*, 6:3, 2003. and references therein.

[73] Lee Lindblom, Benjamin J. Owen, and Sharon M. Morsink. Gravitational radiation instability in hot young neutron stars. *Phys. Rev. Lett.*, 80:4843, 1998. gr-qc/9803053.

[74] J. Papaloizou and J.E. Pringle. Non-radial oscillations of rotating stars and their relevance to the short-period oscillations of cataclysmic variables. *Mon. Not. R. Astr. Soc.*, 182:423, 1978.

[75] Nils Andersson. A new class of unstable modes of rotating relativistic stars. *Astrophys. J.*, 502:708, 1998. gr-qc/9706075.

[76] John L. Friedman and Sharon M. Morsink. Axial instability of rotating relativistic stars. *Astrophys. J.*, 502:714, 1998. gr-qc/9706073.

[77] Nils Andersson, Kostas D. Kokkotas, and Bernard F. Schutz. Gravitational radiation limit on the spin of young neutron stars. *Astrophys. J.*, 510:846, 1999. astro-ph/9805225.

[78] Benjamin J. Owen et al. Gravitational waves from hot young rapidly rotating neutron stars. *Phys. Rev.*, D58:084020, 1998. gr-qc/9804044.

[79] J. Provost, G. Berthomieu, and A. Rocca. Low frequency oscillations of a slowly rotating star - quasi toroidal modes. *Astron. Astrophys.*, 94:126, 1981.

[80] E. Flowers and N. Itoh. Transport properties of dense matter. *Astrophys. J.*, 206:218, 1976.

[81] D. G. Yakovlev and P. Haensel. What we can learn from observations of cooling neutron stars. *Astron. Astrophys.*, 407:259, 2003. astro-ph/0209026.

[82] L. Lindblom and G. Mendell. Does gravitational radiation limit the angular velocities of superfluid neutron stars? *Astrophys. J.*, 444:804, 1995.

[83] Xiao-ping Zheng, Xue-wen Liu, Miao Kang, and Shu-hua Yang. Bulk viscosity of strange quark matter in density-dependent quark mass model and dissipation of r-modes in strange stars. *Phys. Rev.*, C70:015803, 2003. astro-ph/0305320.

[84] Mark G. Alford, Matt Braby, Sanjay Reddy, and Thomas Schaefer. Bulk viscosity due to kaons in color-flavor-locked quark matter. 2007. nucl-th/0701067.

[85] Mark G. Alford and Andreas Schmitt. Bulk viscosity in 2sc quark matter. *J. Phys.*, G34:67–102, 2007.

[86] Na-Na Pan, Xiao-Ping Zheng, and Jia-Rong Li. Bulk viscosity of mixed nucleon-hyperon-quark matter in neutron stars. *Mon. Not. Roy. Astron. Soc.*, 371:1359, 2006. astro-ph/0607051.

[87] Zheng Xiaoping et al. Implication of existence of hybrid stars and theoretical expectation of submillisecond pulsars. *New Astron.*, 12:165, 2006. astro-ph/0609011.

[88] Kostas Glampedakis and Nils Andersson. Ekman layer damping of r-modes revisited. *Mon. Not. Roy. Astron. Soc.*, 371:1311, 2006. astro-ph/0607105.

[89] Debarati Chatterjee and Debades Bandyopadhyay. Bulk viscosity in kaon condensed matter. 2007. astro-ph/0702259.

[90] L. D. Landau and E. M. Lifshitz. *Fluid Mechanics*. Butterworth-Heinemann, Oxford, 2nd edition, 1999.

[91] R. F. Sawyer. Bulk viscosity of hot neutron–star matter and the maximum rotation rates of neutron stars. *Phys. Rev.*, D39:3804, 1989.

[92] R. Reif. *Fundamentals of Statistical and Thermal Physics*. McGraw-Hill, New York, 1965.

[93] D. J. Griffiths. *Introduction to Elementary Particles*. Wiley, New York, 1987.

[94] J. Papaloizou and J.E. Pringle. Gravitational radiation and the stability of rotating stars. *Mon. Not. R. Astron. Soc.*, 184:501, 1978.

[95] A. Katrin Schenk, Phil Arras, Eanna E. Flanagan, Saul A. Teukolsky, and Ira Wasserman. Nonlinear mode coupling in rotating stars and the r-mode instability in neutron stars. *Phys. Rev.*, D65:024001, 2002. gr-qc/0101092.

[96] Sharon M. Morsink. Nonlinear couplings between r-modes of rotating neutron stars. *Astrophys. J.*, 571:435, 2002. astro-ph/0202051.

[97] Phil Arras et al. Saturation of the r-mode instability. *Astrophys. J.*, 591:1129, 2003. astro-ph/0202345.

[98] Jeandrew Brink, Saul A. Teukolsky, and Ira Wasserman. Nonlinear couplings of r-modes: Energy transfer and saturation amplitudes at realistic timescales. *Phys. Rev.*, D70:121501, 2004. gr-qc/0406085.

[99] Jeandrew Brink, Saul A. Teukolsky, and Ira Wasserman. A nonlinear coupling network to simulate the development of the r-mode instablility in neutron stars I. Construction. *Phys. Rev.*, D70:124017, 2004. gr-qc/0409048.

[100] Jeandrew Brink, Saul A. Teukolsky, and Ira Wasserman. A nonlinear coupling network to simulate the development of the r-mode instablility in neutron stars II. Dynamics. *Phys. Rev.*, D71:064029, 2005. gr-qc/0410072.

[101] Paulo M. Sa and Brigitte Tome. Nonlinear evolution of r-modes: The role of differential rotation. *Phys. Rev.*, D71:044007, 2005. gr-qc/0411072.

[102] W. D. Langer and A. G. W. Cameron. Effects of Hyperons on the Vibrations of Neutron Stars. *Astrophys. Space Sci.*, 5:213, 1969.

[103] P. B. Jones. Pulsation damping by the nonleptonic weak interaction in hyperon stars. *Astrophys. Lett.*, 5:33, 1970.

[104] P. B. Jones. Astrophysical significance of the dissipation of turbulence in a dense baryon fluid. *Proc. Roy. Soc. (London)*, A323:111, 1971.

[105] P. B. Jones. Comment on 'gravitational radiation instability in hot young neutron stars'. *Phys. Rev. Lett.*, 86:1384, 2001.

[106] P. B. Jones. Bulk viscosity of neutron-star matter. *Phys. Rev.*, D64:084003, 2001.

[107] E. N. E. van Dalen and A. E. L. Dieperink. Bulk viscosity in neutron stars from hyperons. *Phys. Rev.*, C69:025802, 2004. nucl-th/0311103.

[108] Jes Madsen. How to identify a strange star. *Phys. Rev. Lett.*, 81:3311, 1998. astro-ph/9806032.

[109] Lee Lindblom, Benjamin J. Owen, and Greg Ushomirsky. Effect of a neutron-star crust on the r-mode instability. *Phys. Rev.*, D62:084030, 2000. astro-ph/0006242.

[110] Yuri Levin and Greg Ushomirsky. Crust-core coupling and r-mode damping in neutron stars: a toy model. *Mon. Not. Roy. Astron. Soc.*, 324:917, 2001. astro-ph/0006028.

[111] Yanqin Wu, Christopher D. Matzner, and Phil Arras. R-modes in neutron stars with crusts: Turbulent saturation, spin-down, and crust melting. *Astrophys. J.*, 549:1011, 2001. astro-ph/0006123.

[112] Justin B. Kinney and Gregory Mendell. The r-modes in accreting neutron stars with magneto-viscous boundary layers. *Phys. Rev.*, D67:024032, 2003. gr-qc/0206001.

[113] Deepto Chakrabarty et al. Nuclear-powered millisecond pulsars and the maximum spin frequency of neutron stars. *Nature*, 424:42, 2003. astro-ph/0307029.

[114] Yuri Levin. Runaway heating by r-modes of neutron stars in low mass x-ray binaries. *Astrophys. J.*, 517:328, 1999. astro-ph/9810471.

[115] H. C. Spruit. Gamma-ray bursts from x-ray binaries. *Astron. Astrophys.*, 341:L1, 1998. astro-ph/9811007.

[116] J. S. Heyl. Low-mass x-ray binaries may be important laser interferometer gravitational-wave observatory sources after all. *Astrophys. J.*, 574:L57, 2002.

[117] Robert V. Wagoner, Joseph F. Hennawi, and Jing-song Liu. Gravitational radiation evolution of accreting neutron stars. 2001. astro-ph/0107229.

[118] Andreas Reisenegger and Axel A. Bonacic. Millisecond pulsars with r-modes as steady gravitational radiators. *Phys. Rev. Lett.*, 91:201103, 2003. astro-ph/0303375.

[119] Robert V. Wagoner. A timing signature of gravitational radiation from LMXB neutron stars. *AIP Conf. Proc.*, 714:224, 2004. astro-ph/0312433.

[120] N. Andersson, D. I. Jones, and K. D. Kokkotas. Strange stars as persistent sources of gravitational waves. *Mon. Not. Roy. Astron. Soc.*, 337:1224, 2002. astro-ph/0111582.

[121] K. Hagiwara et al. Review of particle physics. *Phys. Rev.*, D66:010001, 2002.

[122] N. W. Ashcroft and N. D. Mermin. *Solid State Physics*. Brookes Cole, 1st edition, 1976.

[123] T. Takatsuka, S. Nishizaki, Y. Yamamoto, and R. Tamagaki. The possibility of hyperon superfluids in neutron star cores. *Prog. Theor. Phys.*, 105:179, 2001.

[124] A. D. Kaminker, D. G. Yakovlev, and O. Y. Gnedin. Three types of cooling superfluid neutron stars: Theory and observations. *Astron. Astrophys.*, 383:1076, 2002.

[125] James B. Hartle. Slowly rotating relativistic stars. 1. Equations of structure. *Astrophys. J.*, 150:1005, 1967.

[126] Lee Lindblom, Gregory Mendell, and Benjamin J. Owen. Second-order rotational effects on the r-modes of neutron stars. *Phys. Rev.*, D60:064006, 1999. gr-qc/9902052.

[127] Edward F. Brown, Lars Bildsten, and Philip Chang. Variability in the thermal emission from accreting neutron star transients. *Astrophys. J.*, 574:920, 2002. astro-ph/0204102.

[128] D. G. Yakovlev, K. P. Levenfish, Alexander Y. Potekhin, O. Y. Gnedin, and G. Chabrier. Thermal states of coldest and hottest neutron stars in soft x-ray transients. *Astron. Astrophys.*, 417:169, 2004. astro-ph/0310259.

[129] Nils Andersson and G. L. Comer. A flux-conservative formalism for convective and dissipative multi-fluid systems, with application to newtonian superfluid neutron stars. *Class. Quant. Grav.*, 23:5505, 2005. physics/0509241.

[130] Massimo Mannarelli, Krishna Rajagopal, and Rishi Sharma. The rigidity of crystalline color superconducting quark matter. 2007. hep-ph/0702021.

[131] Edward Farhi and R. L. Jaffe. Strange matter. *Phys. Rev.*, D30:2379, 1984.

[132] Mark Alford, Matt Braby, M. W. Paris, and Sanjay Reddy. Hybrid stars that masquerade as neutron stars. *Astrophys. J.*, 629:969, 2005. nucl-th/0411016.

[133] Omar Benhar, Valeria Ferrari, Leonardo Gualtieri, and Stefania Marassi. Constraining the MIT bag model of quark matter with gravitational wave observations. 2006. astro-ph/0603464.

[134] Sudip Bhattacharyya. Private communication.

[135] D. G. Ravenhall, C. J. Pethick, and J. R. Wilson. Structure of matter below nuclear saturation density. *Phys. Rev. Lett.*, 50:2066, 1983.

[136] N. K. Glendenning and S. Pei. Crystalline structure of the mixed confined - deconfined phase in neutron stars. *Phys. Rev.*, C52:2250, 1995.

[137] H. Heiselberg, C. J. Pethick, and E. F. Staubo. Quark matter droplets in neutron stars. *Phys. Rev. Lett.*, 70:1355, 1993.

[138] K. Fuchs. A quantum mechanical calculation of the elastic constants of monovalent metals. *Proc. Roy. Soc.*, A153:622, 1936.

[139] Piotr Jaranowski, Andrzej Krolak, and Bernard F. Schutz. Data analysis of gravitational-wave signals from spinning neutron stars. I: The signal and its detection. *Phys. Rev.*, D58:063001, 1998. gr-qc/9804014.

[140] Michal Bejger and P. Haensel. Moments of inertia for neutron and strange stars: Limits derived for the crab pulsar. *Astron. Astrophys.*, 396:917, 2002. astro-ph/0209151.

[141] Brynmor Haskell, D. I. Jones, and N. Andersson. Mountains on neutron stars: Accreted vs. non-accreted crusts. *Mon. Not. Roy. Astron. Soc.*, 373:1423, 2006. astro-ph/0609438.

[142] M. Zucker. Talk G070070–A–D: S5, S6 and S7. March 2007. http://www.ligo.caltech.edu/docs/G/G070070-A/.

[143] B. Abbott et al. (LIGO Science Collaboration). Coherent searches for periodic gravitational waves from unknown isolated sources and Scorpius X-1: results from the second LIGO science run. gr-qc/0605028.

[144] B. Abbott et al. (LIGO Science Collaboration), M. Kramer and A. G. Lyne. Upper limits on gravitational wave emission from 78 radio pulsars. 2007. gr-qc/0702039.

[145] J. R. Thorstensen, R. A. Fesen, and S. van den Bergh. The expansion center and dynamical age of the galactic supernova remnant Cassiopeia A. *Astron. J.*, 122:297, Jul 2001. astro-ph/0104188.

Vita

Mohit Nayyar was born on November 30, 1978 in Jaipur, India. He received his B. Tech. in Engineering Physics from the Indian Institute of Technology, Bombay in 2000. Since then he has been a graduate student at the Pennsylvania State University at University Park. He was a recipient of the Braddock Fellowship for the academic year 2000-2001. His publications include:

- B. D. Lackey, M. Nayyar, and B. J. Owen. Observational constraints on hyperons in neutron stars. *Physical Review D.* 73:024021–024028, 2006.
- M. Nayyar and B. J. Owen. *R*-modes of accreting hyperon stars as persistent sources of gravitational waves. *Physical Review D.* 73:084001–084014, 2006.
- M. Nayyar, and B. J. Owen. Gravitational radiation from quark-hybrid stars. *In preparation.*